Spatial solitons and optical vortices in nematic liquid crystals

Raouf Barboza

Spatial Solitons and Optical Vortices in Nematic Liquid Crystals

Raouf BARBOZA

Department of Engineering

University of Rome

A thesis submitted for the degree of

Doctor of Philosophy

2013

International Doctoral School **EDEMOM**
European **D**octorate in **E**lectronic **M**aterials, **O**ptoelectronics and **M**icrosystems.

Doctor of Philosophy Course in Electronic Engineering - XXV CICLO

Spatial Solitons and Optical Vortices in Nematic Liquid Crystals

BARBOZA Raouf

Departement Of Engineering

Universtity of Rome ROMA Tre

in cotutele with:

Universtity of Nice-Sofia Antipolis.

Discipline: PHYSICS

Tutors:
Prof. Gaetano ASSANTO

Prof. Stefania RESIDORI

Coordinator:
Prof. Giuseppe SCHIRRIPA SPAGNOLO

UNIVERSITÉ DE NICE-SOPHIA ANTIPOLIS - UFR Sciences
Ecole Doctorale Sciences Fondamentales et Appliquées

THESE
pour obtenir le titre de
Docteur en Sciences

de l'UNIVERSITÉ de Nice-Sophia Antipolis
Discipline: Physique

presentée et soutenue par
Raouf BARBOZA

Solitons and Optical Vortices in Nematic Liquid Crystals

en cotutele avec:

Departement of Engineering
Universtity of Rome "ROMA Tre"

These dirigée par:

Prof. Stefania RESIDORI — *Université de Nice Sophia-Antipolis*

Prof. Gaetano ASSANTO — *Universtity of Rome ROMA TRE*

soutenue le: 17 Juin 2013
á : Rome - ITALIE

Jury:

Prof. Stefania RESIDORI	Directeur
Prof. Etienne BRASSELET	Rapporteur
Prof. Pasquale CARELLI	Rapporteur
Prof. Giuseppe SCHIRRIPA SPAGNOLO	Examinateur

Abstract

Liquid crystals have been all along a fertile background for scientific research, from mathematics to materials science to optics; their use is not limited to displays but extends to nonlinear optics, switching, routing. Due to their extreme sensitivity to electric fields at frequencies ranging from continuous wave to optics, they are also nonlinear media supporting the generation and propagation of self confined beams, called spatial optical solitons, at very low powers. Spatial optical solitons have the property to propagate without diffraction, as diffraction is compensated by nonlinear self-focusing of the medium in which light is injected, resulting in self-induced waveguides. These waveguides in nematic liquid crystals can in turn confine and route other optical signals and can be reconfigured, optically or electrically, as soliton trajectories can be controlled by other fields, paving the way to optical and all-optical manipulation. Nematic liquid crystals have also been recently employed with success in the so called singular optics, in which the key parameter is the topologic singularity carried by the phase of an electromagnetic wave. In this thesis I will report on my work on spatial optical solitons and optical singularities in nematic liquid crystals. In the first chapter I will outline the basic properties of nematic liquid crystals, with an introduction to solitons in nonlinear optics. In the second I will discuss the generation of optical spatial solitons and their steering in nematic liquid crystals. In the third chapter I will present the basic concepts of singular optics , followed by a discussion on vortices and their generation using optical induction of defects.

Contents

List of Figures

List of Tables

Chapter 1

Introduction

1.1 Basic Properties of Liquid Crystals

Liquid crystals (LCs) are formed by organic molecules strongly elongated in one direction. Therefore, they are characterized by an anisotropy in their physical properties: electrical, optical and structural. In certain ranges of temperature, LC form *mesophases*, that is, phases that are intermediate between liquids and solids. Figure 1.1 illustrates the nematic phase and its differences with respect to an isotropic (normal liquid) phase and a crystalline (perfectly ordered) structure. In the nematic phase all the molecules are in average aligned along a preferential direction, so called the nematic director $\hat{n}$, therefore they have orientational order but still lack positional order.

(a) **Isotropic** (b) **Nematic** (c) **Crystal**

Figure 1.1: The isotropic phase (a) is characterized by the absence of both orientational and positional order. In the nematic state (b) a long range orientation order is observed, but the molecules still lack positional order. If cooled, the nematic state can go through other states and finally become a solid crystalline (c) structure.

Liquid crystals can exhibit other phases like:

- *smectic*: it is distinguishable from nematics by the existence of a long range positional order along the nematic director, hence the molecules are distributed in layers called smectic planes without a positional order. The angle of the normal to the layers and the director defines a subclass of smectics: SmA when the director is perpendicular to the layer, SmC when the director is tilted, SmC* when the director is tilted but also twists continuously around the normal.
- *columnar*: the molecules are ordered in two dimension. This situation is found typically for molecules (or aggregates) exhibiting disc shape, often called *discotics*.
- *cholesteric*: consist of quasi-nematic parallel layers, with a constant twist around the normal to the layers.

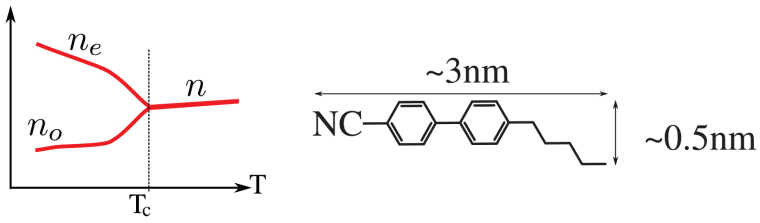

(a) (b)

Figure 1.2: (a) Sketch of the typical behavior of the refractive indexes of nematic liquid crystal; above T_c the critical temperature for the nematic to isotropic transition, the anisotropy vanishes . (b) Chemical structure of 5CB liquid crystal

In this work, we will be using only nematic liquid crystals. The constituent molecules of the nematic phase are very long with respect to their averaged diameter (figure 1.2(b)), with a negligible bend. Due to the fast rotation around their axis (this time scale is comparatively small than the other time scales), they are considered in average a cylindrical structure with no head and tail difference, at least for non polar molecules, which is our case. Hence, the averaged molecular directors (in a volume small but large compared to the molecule length), i.e., the molecular director $\hat{n}$, is physically indistinguishable from $-\hat{n}$. Due to the thermal agitation, the molecules will fluctuate around their average direction. Thus, the physical properties (at least the basic ones), by using the simplest theories, will depend on the statistical average of the molecule director and the deviation from it. Considering a polar reference system with the polar axis z coinciding with the nematic director, the molecular directions are statistically described

by a distribution function $s(\xi, \phi)$, with $\int_{\mathcal{V}} s(\xi, \phi) dv$, $\mathcal{V}$ a sphere with diameter about the correlation length located in position $\vec{r}$. In the limit of conventional nematics, with cylindrically symmetric molecules, s does not depend on ξ. Then, it suffices to use one statistical non null average to describe the ordering effect; the scalar order parameter S defined as:

$$S(\vec{r}) = \int_{\mathcal{V}} s(\phi) \mathrm{P}_2(\cos\phi) dV, \tag{1.1}$$

being P_2 the second order Legendre polynomial (the weighing function is used in order to select the first non zero weighted moment). From the definition $-\frac{1}{2} \leq S \leq 1$. But it is more common to have in the equilibrium liquid crystal state the scalar order parameter such that $0 \leq S \leq 1$. $S = 0$ correspond to the loss of the long range orientational order (isotropic), $S = 1$ all molecules aligned along $\vec{n}$, the unusual case $S = -\frac{1}{2}$ all the molecules randomly orientated in the plane orthogonal to the nematic director. As the temperature of the liquid crystal changes, the scalar order parameter S will change from 0: the isotropic state corresponding to high temperature, to $S = 1$ crystalline state: low temperature. This change in the phase of the liquid crystal is reflected in the change of its physical properties, like, for example, the refractive index, for which the material will exhibit an optical anisotropy that vanishes above a critical temperature T_c: the nematic to isotropic transition temperature (see figure 1.2(a)). The physical macroscopic parameters of a nematic liquid crystal will be that of a uniaxial material, a uniaxial tensor, i.e. same value along all directions perpendicular to $\hat{n}$ and a different value along $\hat{n}$. Thus, every characteristics will be written as $\underline{\underline{\chi}} = \chi_\perp + (\chi_\parallel - \chi_\perp)\hat{n}\hat{n}$ [1], with $\chi_a = \chi_\parallel - \chi_\perp$ the parameter anisotropy. They are booth temperature dependent with a vanishing anisotropy when the nematic temperature is above T_c i.e, in isotropic phase.

1.2 Continuum Theory

Liquid crystals are very sensitive to external stimuli: electrical and optical. When a field is applied to the LC, the molecules feel the torque exerted by the external field, the director distribution is modified until a new equilibrium condition is reached. To describe their behavior, we need to construct a parameter that encompasses the order parameter S and the molecular director $\hat{n}$. Note that we must maintain in our description the fact that $\hat{n}$ and $-\hat{n}$ are equivalent. So a second rank traceless tensor,

[1] $\vec{u}\vec{v}$ represent the dyadic product between the two vectors.

called Q- tensor, defined as $Q = S(\hat{n}\hat{n} - \frac{1}{3}\mathbb{1})$ is used [1, 2, 3]. The energy of of the liquid crystal can be written then, in terms of components of Q (Landau-deGennes expansion), and can be demonstrated to be dependent only on S [3]. When the liquid crystal is subjected to an external force, the director field is deformed, deformation which is taken into account by considering the spatial derivatives of the Q-tensor in the computation of the energy: thus variation of S and $\hat{n}$ are taken care of. When the deformation rate is smooth enough (with respect to the nematic coherence length), and there is no defect with singular core, and temperature effects are neglected, a more simple formulation based only on the nematic director is used. The balance of the energy of the liquid crystal consists, then, in taking into account the terms of second order in the product of the first order spatial derivative of the component of the nematic director, the term linear in $\hat{n}$ or its spatial derivative a zero due to the equivalence of $\hat{n}$ and $-\hat{n}$. This assumptions lead to the well known Oseen-Zöcher-Frank formula for the free energy (or distortion energy) density, written as:

$$\mathcal{F}_K = \frac{1}{2}K_1(\nabla \cdot \hat{n})^2 + \frac{1}{2}K_2(\hat{n} \cdot \nabla \times \hat{n})^2 + \frac{1}{2}K_3(\hat{n} \times \nabla \times \hat{n})^2, \tag{1.2}$$

with K_1, K_2 and K_3 the constants of the three elementary elastic deformations of the LC respectively *splay* (figure 1.3(a)), *twist* (figure 1.3(c)) and *bend* (figure 1.3(b)).

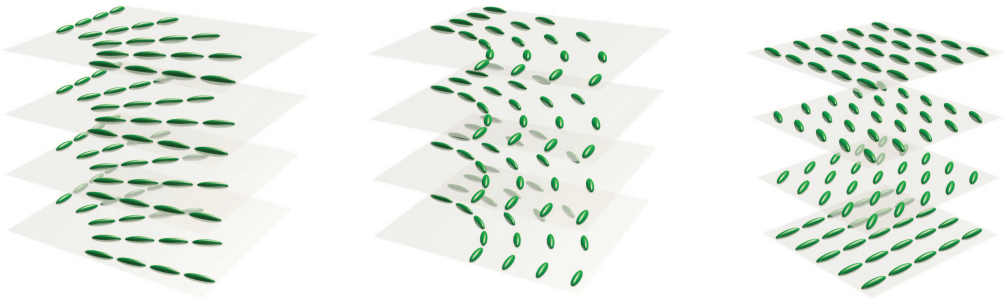

(a) Splay (b) Bend (c) Twist

Figure 1.3: The three elementary elastic distortions of a nematic liquid crystal: (a) splay, (b) bend, (c) twist.

In the presence of external excitations, the free energy density has to be supplemented with the interaction energies in order to find the configuration of the deformed liquid crystal director field. For an optical field we need to consider the averaged

interaction energy [1] density given by:

$$\mathcal{F}_{\mathcal{E}} = -\frac{1}{2} < \vec{\mathcal{E}} \cdot \vec{\mathcal{D}} >_t, \tag{1.3}$$

with $\vec{\mathcal{E}}$ the electric field, $\vec{\mathcal{D}}$ the displacement. For a monochromatic, or a quasi-monochromatic field, the averaged value of the contribution of the energy gives:

$$\mathcal{F}_{\mathcal{E}} = -\frac{1}{4}\mathrm{Re}\left[\vec{\mathcal{E}}^* \cdot \vec{\mathcal{D}}\right].$$

Note that we have neglected the magnetic field contribution. Indeed at optical frequencies LC are in general non magnetic media. Low frequency fields (or quasi static fields) can also interact with the liquid crystal due to the medium polarizability . Their effect is taken into account by adding to the free energy:

$$\mathcal{F}_E = -\frac{1}{2}\vec{E} \cdot \vec{D}, \tag{1.4}$$

where $\vec{E}$ and $\vec{D}$ represent, respectively, the electric field and the electric displacement. The final configuration is found by minimizing over the volume of the LC medium the total free energy:

$$\boldsymbol{\mathcal{F}} = \int_{\mathcal{V}} \mathrm{d}^3\vec{\mathrm{r}} \left[\mathcal{F}_K + \mathcal{F}_E + \mathcal{F}_{\mathcal{E}} + \frac{\boldsymbol{\lambda}}{2}(|\hat{n}|^2 - 1)\right] \tag{1.5}$$

with $\boldsymbol{\lambda}$ the Lagrange multiplier accounting for the fact that $\hat{n} \cdot \hat{n} = 1$. The minimization done variationally on $\hat{n}$ gives the Euler-Lagrange equation for the statics of the nematic liquid crystal and it is written in a more compact form as

$$\hat{n} \times \frac{\delta\mathcal{F}}{\delta\hat{n}} = 0 \tag{1.6}$$

where $\dfrac{\delta\mathcal{F}}{\delta\hat{n}}$ is the variational, or Fréchet derivative of $\mathcal{F}$ with respect to $\hat{n}$.

The equation of the statics for the nematic medium has to be supplemented with the constitutive relations of the external fields. For the quasi static electric field we can write $\vec{E} = -\nabla V$, with $\vec{D} = \underline{\underline{\epsilon}}^{\Omega} \cdot \vec{E}$, the quasi-static potential V at frequency Ω. The quasi-static potential V can be described by the anisotropic Laplace equation

$$\nabla \cdot \underline{\underline{\epsilon}}^{\Omega} \cdot \nabla V = 0. \tag{1.7}$$

[1] The time scale of the mechanical response of the nematic liquid crystal due to the optical field is far greater than that of the electronic response of the single molecules, the later will be neglected.

Here we assume the absence of free charges in the media, that is the LC is a perfect dielectric, and $\underline{\underline{\epsilon}}^{\Omega}$ is the dielectric tensor at Ω.

The evolution of the optical field $\vec{\mathcal{E}}$, oscillating at frequency ω, with $\vec{\mathcal{D}} = \underline{\underline{\epsilon}}^{\omega} \cdot \vec{\mathcal{E}}$, of the optical field is governed by the Maxwell equations:

$$\nabla \times \nabla \times \vec{\mathcal{E}} = k_0^2 \underline{\underline{\tilde{\epsilon}}}^{\omega} \cdot \vec{\mathcal{E}}, \tag{1.8}$$

with $\underline{\underline{\epsilon}}^{\omega} = \epsilon_0 \underline{\underline{\tilde{\epsilon}}}^{\omega}$ the dielectric tensor.

1.3 Optical reorientation

To get a more physical insight in the statics of the LC medium, its is convenient to write the equation 1.6 in terms of momentum balance. The same equation can be written in term of torque balance, gives:

$$\vec{\Gamma}_K + \vec{\Gamma}_E + \vec{\Gamma}_{\mathcal{E}} = 0, \tag{1.9}$$

$\vec{\Gamma}_i = -\hat{n} \times \dfrac{\delta \mathcal{F}_i}{\delta \hat{n}}$, $i = K, E, \mathcal{E}$.

The elastic torque, in the approximation of all elastic constant being equal (or one elastic constant approximation), has a simple expression given by:

$$\vec{\Gamma}_K = \hat{n} \times K \nabla^2 \hat{n}.$$

The electric torque and the optical torque are given respectively by

$$\vec{\Gamma}_E = \epsilon_a^{\Omega} \left(\hat{n} \cdot \vec{E} \right) \hat{n} \times \vec{E},$$

and

$$\vec{\Gamma}_{\mathcal{E}} = \frac{1}{2} \epsilon_a^{\omega} \mathrm{Re} \left[\left(\hat{n} \cdot \vec{\mathcal{E}}^* \right) \hat{n} \times \vec{\mathcal{E}} \right].$$

When an external linearly polarized optical field is applied to NLC [1] with positive dielectric anisotropy, that is, $\epsilon_a^{\omega} = \epsilon_{\parallel}^{\omega} - \epsilon_{\perp}^{\omega} \geq 0$, due to the induced dipoles, in this case parallel the long axis, the molecule will rotate toward the field in order to minimize the interaction energy, with an increasing effect for high field. The opposite happens when the anisotropy is negative $\epsilon_a^{\omega} \leq 0$, as the induced dipoles are perpendicular to the axis, and the molecule will rotate away from the field in order to align the dipoles parallel

[1] The same discussion holds for static and low frequency fields.

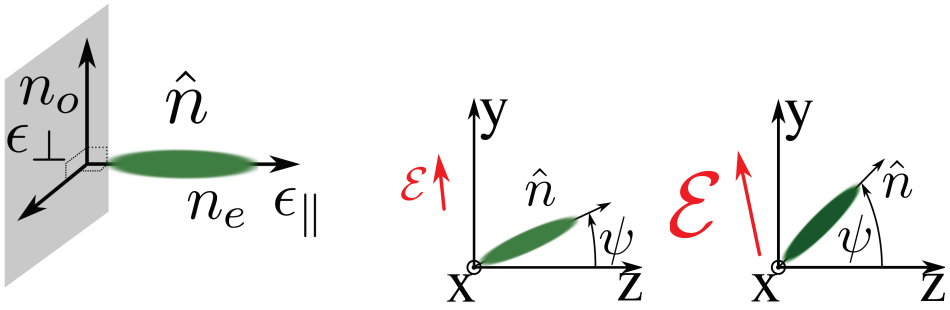

(a) (b) (c)

Figure 1.4: (a) Electro-optical properties of an NLC. Effect of linearly polarized optical field on the nematic: the scketch are shown for low (b) and high (c) field intensity.

to the field. The equilibrium condition is reached when the induced torque is balanced by elastic the torque steaming from the interaction between the molecules. When the initial nematic director is perpendicular to the electric field for a NLC with a positive anisotropy (parallel in the case of negative anisotropy), the reorientation takes place when the field strength is above a threshold, called the Freedericks threshold [3]. For now, we will put ourselves in conditions that avoid the Fredericksz effect, effect that we will exploit later in chapter 3.

1.4 Optical reorientational nonlinearity.

Let us consider a plane wave with a propagating wave vector $\mathbf{k}$ in a homogeneous NLC, with the nematic director an the electric field in the same plane $y - z$. Due to the anisotropy, the propagating field will experience a refractive index depending on its angle with respect to the nematic director. When $\hat{n}$ lies along $\mathbf{k}$, the refractive index seen is that of a wave polarized in the plane perpendicular to $\hat{n}$, that is, the ordinary refractive index:

$$n_o = n_\perp = \sqrt{\tilde{\epsilon}_\perp}$$

For a non null angle, the refractive index, termed as extraordinary refractive index is, given by:

$$n_e(\psi) = \frac{n_\perp n_\parallel}{\sqrt{n_\perp^2 \sin^2\psi + n_\parallel^2 \cos^2\psi}},$$

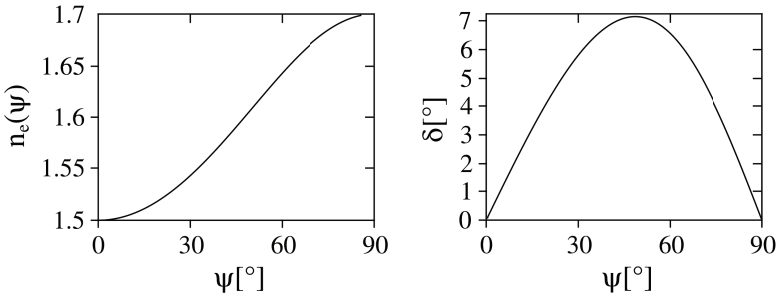

(a) (b)

Figure 1.5: (a) Extraordinary refractive index versus the angle ψ between $\hat{n}$ and $\mathbf{k}$. The parameters are chosen for the E7 LC mixture. (b) Walkoff versus ψ.

with $n_{\parallel} = \sqrt{\tilde{\epsilon}_{\parallel}} = n_e$, the refractive index of waves oscillating along $\hat{n}$ [1] Moreover, Poynting vector S propagates at a not negligible *walk-off* angle δ with respect to $\mathbf{k}$, being $\tan\delta = \dfrac{\epsilon_{yz}}{\epsilon_{zz}}$ that is:

$$\delta = \arctan \frac{\epsilon_a \sin\psi \cos\psi}{\epsilon_{\perp} + \epsilon_a \cos^2\psi}.$$

As we have discussed earlier, the angle of the nematic director changes when subjected to an external field. So, a finite size beam, due to the mechanical torque exerted, will alter the refractive index as the molecules rotates toward the field, ψ increases with the consequent nonlinear change of the effective refractive index. Note that for a NLC with negative optical anisotropy, ψ decreases, but the effect is an increase of $n_e(\psi)$ as $n_o \geq n_e$. This type of optical nonlinearity called reorientational nonlinearity is typical in liquid crystals and have been extensively studied in the literature [4, 5]. A self focusing nonlinearity is obtained for a bell shaped beam (Gaussian). The induced index change also have a bell shape profile, with the medium behaving like a lens. Moreover when the diffraction of the propagating beam is compensated by this self-focusing effect, a spatial optical soliton is formed. Due to the elastic interactions between adjacent molecules, the extension of the nonlinear response is greater than the beam size giving rise to a nonlocal type response. This effect has important consequences on the beam dynamic, matter we will discuss in the next chapter.

[1] the notation $n_e(\psi)$, and n_e can be some time confusing, we will consider $n_e = n_e(\pi/2)$, unless specified otherwise.

1.5 Conclusions

Because of the high polarizability and anisotropy (for example $\Delta n = 0.2$, $\tilde{\epsilon}_a = 14.5$ for E7 mixture) LCs are very sensitive to electrical and optical fields [1]. Low voltages can be used to change the refractive index (via electric fields) and high phase shift are achieved using thin layer of material (tenth of microns). This makes LCs the most used material for electrooptic devices, from displays to optical couplers and polarization cntrollers for telecommunications [6, 7]. Moreover the effective optical nonlinearity is orders of magnitude (≈ 3) greater than that of the most most performant nonlinear crystals. The nonlinear reorientational phenomena can be observed at low powers [5, 8]; hence, LCs are an ideal workbench for investigating all-optical non linear effects. We will consider one of them which is the generation of spatial optical solitons, focusing on their possible applications.

[1] the optical torque an the electric one depend linearly on the anisotropies

Chapter 2

Nematicons: application to beam steering

Owing to their unique properties intermediate between those of liquids and of solids, liquid crystals (LC) are relevant materials in optical signal processing, [7] well beyond their most common use in displays. One of their remarkable features is their sensitivity to applied perturbations, such as electric fields. The latter provides large electro-optic and all-optical responses and significant tunability through molecular reorientation, as exploited e.g. in LC light valves,[9] light modulators,[10] adjustable lenses,[11] etc. Due to LC high polarizability and anisotropy, nonlinear reorientational phenomena can be observed at low powers;[12] hence, LC are an ideal workbench for investigating all-optical effects, e.g. switching in waveguides.[13, 14] Reorientational self-focusing in nematic LC (NLC), i.e. LC with a high degree of orientational but no positional order [12] supports spatial solitons or *nematicons*, at mW powers.[15] Nematicons are light-induced waveguides with nonlocal features providing stability, robustness and long range interactions, even with partially incoherent light; [16] they can confine and route weaker copolarized signals of any wavelengths and transmission protocols; in short, they can form a reconfigurable fabric of interconnections in circuits defined by light and with paths controlled by light and/or by voltage(s)[17, 18].

In this chapter we analyze a scheme for the effective angular deflection of self-guided beams, using NLC and voltage-driven dielectric interfaces, finally a practical realization of the beam steering device will be given.

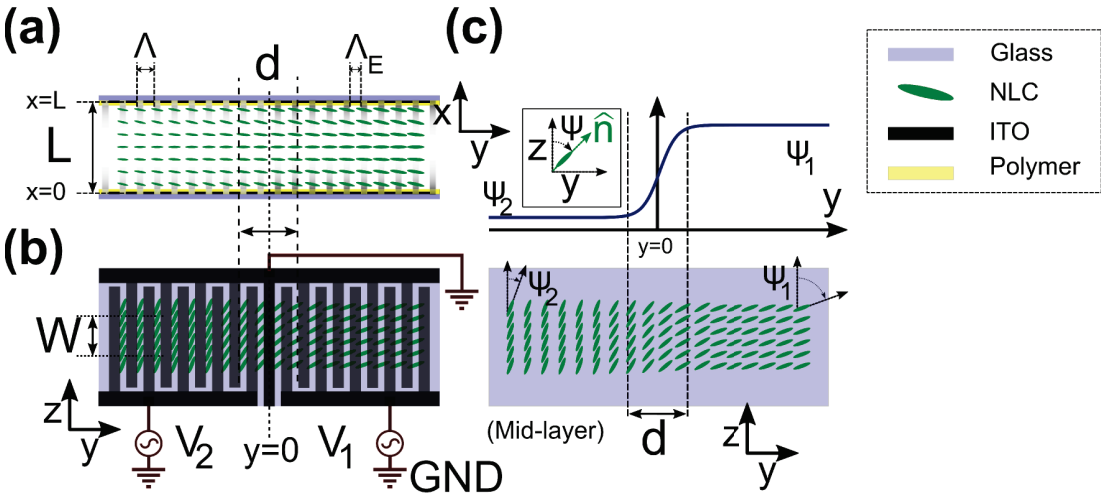

Figure 2.1: Sketch of the proposed structure. (a)Front view; the superposed gray-scale map represents the intensity of the low-frequency electric field E_{LF} (darkest colour corresponds to stronger field). (b) Top view. (c) Bottom: distribution of the NLC molecular director in the mid-layer; top: behaviour of ψ versus y in $x = L/2$. The inset shows the reference system for the director $\hat{n}$.

2.1 Theoretical analysis

We resort to a double set of comb-patterned electrodes to achieve in-plane nematicon propagation and steering, bias-tuning the effective anisotropy and avoiding the detrimental effects of out-of-plane walk-off [19]. Electro-optic beam deflectors with large angles were previously demonstrated in ferroelectrics [20] and in LC [21]; however, the use of nematicons with waist of a few μm permits the deflection of guided-wave signals irrespective of their spectral placement and temporal format while maximizing the number of resolvable output spots.

The geometry is sketched in figure 2.1: an NLC layer is confined between two glass slides parallel to plane yz, separated by L along x (figure. 2.1(a)) and treated at the glass/NLC interfaces to ensure the uniform orientation of the optic axis $\hat{n}$ (i.e. the molecular director [12]) at an angle ψ_0 with $\hat{z}$ (see inset in figure. 2.1(c)). Before the rubbing (the treatment to ensure the uniform reorientation), three sets of interdigitated transparent electrodes (e.g. Indium Tin Oxide) with fingers along y and period Λ are deposited on the inner side of the glasses. For simplicity of the design the finger width Λ_E is set to $\Lambda/2$, with 50:50 mark-to-space ratio, see figure 2.1(b). The electrodes are connected in pair and in symmetric fashion with respect to the cell mid-layer: left-top with left-bottom, right-top with right-bottom, and center-top with center-bottom. The

central electrode (the one with finger on the y axis) is grounded; the left and the right one are connected to two low frequency sinusoidal voltage generator respectively V_2 and V_1. The application of the biases can electro-optically twist the NLC molecular dipoles and therefore reorientate the optic axis in yz and throughout the thickness L in the region underneath (figure 2.1). Hereafter we consider an unbound cell along z, in an actual device, this region would be limited by the two dashed lines in figure 2.1(b), with a good uniformity allong z in the dellimited region of with W and an input beam removed from $y = 0$.

2.1.1 Electrically tunable interface in nematic cell.

For $\Lambda \ll L$, the dominant component of the applied electric field E_{LF} is along $\hat{y}$, thus $\hat{n}$ tends to rotate in the plane yz to align the induced dipoles with the field polarization [22, 23]. To first approximation, at each NLC/glass interface $E_{LF}(x = 0) = E_{LF}(x = L) = 0$ under the electrodes and $E_{LF}(x = 0) = E_{LF}(x = L) = 2V_{1,2}/\Lambda$ in between them, decaying exponentially (with a characteristic length l_a) along x towards the cell mid-plane; the E_{LF} distribution for $V_2 > V_1$ is represented in figure. 2.1(a). Owing to the NLC electro-optic response to $|E_{LF}|^2$, the optic axis $\hat{n}$ will be twisted everywhere, with angle its with respect to the z axis depending on ψ_0 and $|E_{LF}|^2$. Moreover, the nonlocal character of the elastic response, in the limit $\Lambda \ll L$, will smooth out the spatial inhomogeneities of E_{LF}, making the bias-driven reorientation voltage-tuned in the two regions across $y = 0$ and uniform through the cell thickness [23, 24]. Therefore, applied biases $V_1 \neq V_2$ give rise to a graded interface along y (see figure 2.1(c)), of width d depending on L and with an electrically controlled change in director angle $\Delta\psi\,(V_1, V_2) = \psi_1 - \psi_2$, with ψ_2 (ψ_1) the orientation in $x = L/2$ for a single set of electrodes biased at V_2 (V_1).

To validate our predictions, we numerically solved the NLC reorientational equation which is obtained by assuming that the nematic director, for all the operating points, lies in the yz plane. Using the equation 1.6 with the one constant approximation i.e. $K_1 = K_2 = K_3$, and $\partial\psi/\partial z = 0$[1], the reorientational equation reads [23, 24]

$$\frac{\partial^2\psi_{LF}}{\partial x^2} + \frac{\partial^2\psi_{LF}}{\partial y^2} + \gamma_{LF}\sin\left(2\psi_{LF}\right)|E_{LF}|^2 = 0, \tag{2.1}$$

with ψ_{LF} the electro-optic reorientation, $\gamma_{LF} = \Delta\epsilon_{LF}/\left(2K\right)$ with $\Delta\epsilon_{LF}$ the low-

[1]This approximation is justified for unbounded cells.

frequency dielectric anisotropy and K the elastic constant. Eq. (2.1) can be normalized by setting $x' = x/L, y' = y/L$ and $V' = \sigma V$, with $\sigma = L/\Lambda$. We chose the parameters of the commercial NLC mixture E7, with $\gamma_{LF} = 5.4V^{-2}$; we also employed $\sigma = 3.3$ and $l_a/L = 0.05$, the latter derived from experimental data[23]. To trade off voltage-sensitivity (the Coulombian torque is maximum for $\psi_0 = 45°$) and the ψ-variation across the interface, we set $\psi_0 = 10°$ (see reorientation curves in figure. 2.2). As expected, ψ is flat (with respect to x) near the mid-plane $x = L/2$ (figure 2.3(a))

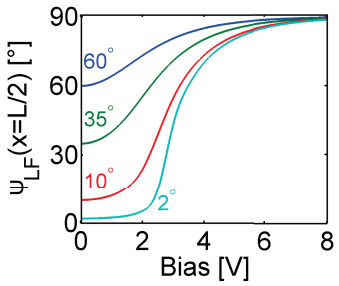

Figure 2.2: Reorientation angle in the cell mid-plane $x = L/2$ versus applied bias, here $V_1 = V_2$ and each label indicates the corresponding background angle ψ_0

and undergoes a negative (positive) variation $\Delta\psi$ along y for $V_1 > V_2$ ($V_1 < V_2$) (figure 2.3(b)), with a quasi-linear trend over a transition length $d \approx L$, independent on V_1 or V_2 (figures 2.4(a)-(c)).

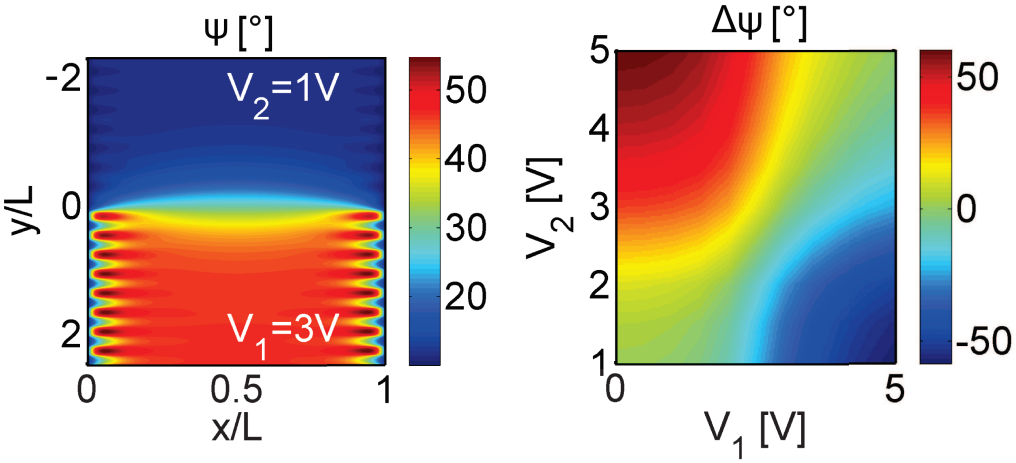

(a) (b)

Figure 2.3: (a) Colormap of $\psi(x, y, z = W/2)$, for $V_1 = 3V$ and $V_2 = 1$. (b) Maximum change in the reorientation angle $\Delta\psi$ versus V_1 and V_2.

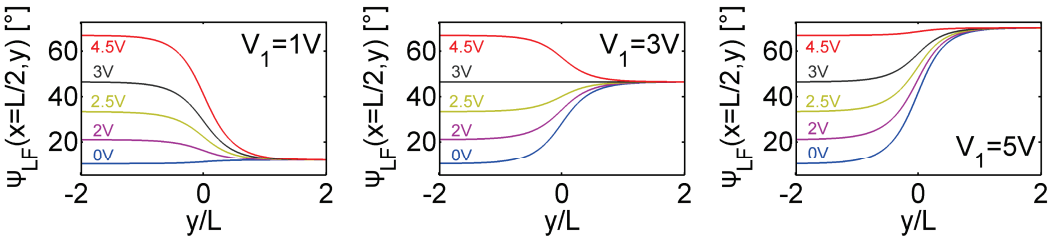

(a) (b) (c)

Figure 2.4: Distribution of the director's angle with the z axis ψ_{LF} in the middle plane for various bias voltage V_1: (a) 1V, (b) 3V and (c) 5V. The numeric labels on each line indicate the corresponding V_2.

2.1.2 Spatial soliton at tunable optical interfaces.

Having established the link between voltages and ψ distribution, i.e. refractive index for extraordinarily polarized light, we turn to nonlinear propagation of beams launched in $y < 0$ (where the index gradient is negligible) with wave vector $\mathbf{k}$ at an angle α with $\hat{z}$ in the plane $x = L/2$ and extraordinary field polarized along $\hat{y}$ (the latter also prevents threshold effects in the reorientational response [24, 25]). Such excitation can reorientate the optic axis in the plane yz, i.e. ensuring in-plane director rotations and corresponding in-plane changes of walk-off. We stress that the spatial soliton trajectory after the interface does not depend on the profile of the transition region but simply on $\Delta\psi$, the specific distribution of ψ_{LF} only affecting the lateral displacement of the beam.

Nonlinear reorientation in yz and self-confined beam (i.e. nematicon) dynamics can be modelled in 2D by [23]:

$$2ik_0n_0\left(\frac{\partial A}{\partial z}+\tan\delta\frac{\partial A}{\partial y}\right)+D_y\frac{\partial^2 A}{\partial y^2}+k_0^2\Delta n_e^2 A=0 \tag{2.2}$$

$$\frac{\partial^2\psi_{NL}}{\partial z^2}+\frac{\partial^2\psi_{NL}}{\partial y^2}-\left(\frac{\pi}{L}\right)^2\psi_{NL}+\gamma\sin\left[2(\psi_{LF}+\psi_{NL}-\delta)\right]|A|^2=0 \tag{2.3}$$

with A the magnetic field along x, $\gamma = [\epsilon_0/(4K)]\left(n_\parallel^2-n_\perp^2\right)\left[Z_0/(n_0\cos\delta)\right]^2$ (Z_0 is the vacuum impedance), ψ_{NL} the (nonlinear) perturbation on ψ due to light (i.e., $\psi=\psi_{LF}+\psi$), D_y the diffraction coefficient, δ the walk-off, k_0 the vacuum wavenumber, n_0 the extraordinary index and $\Delta n_e^2 = n_e^2(\psi)-n_0^2$ the refractive index change, including electro-optic (ψ_{LF}) and all-optical contributions (ψ_{NL}). The nematicon trajectory can

be calculated using the Ehrenfest's theorem [26]:

$$\frac{d^2\langle y\rangle}{dz^2} = \frac{n_e}{n_0^2}\frac{\partial n_e}{\partial y} + \frac{d\tan\delta}{dz}, \tag{2.4}$$

where $\langle y\rangle = \int y|A|^2dy / \int |A|^2dy$ is the soliton position. Equation (2.4) is general, as it provides the effective transverse force acting on the soliton when the local wave vector is aligned to z [26].

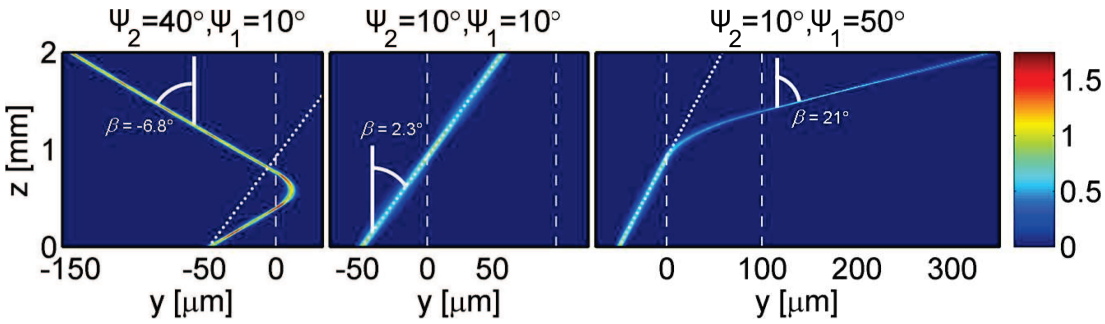

Figure 2.5: Nematicon evolution for P=3mW; dashed and dotted white lines indicate the interface borders and the beam trajectory when $\psi_{LF} = 10°$, β indicates the deflection endured by the soliton with respect to the z axis.

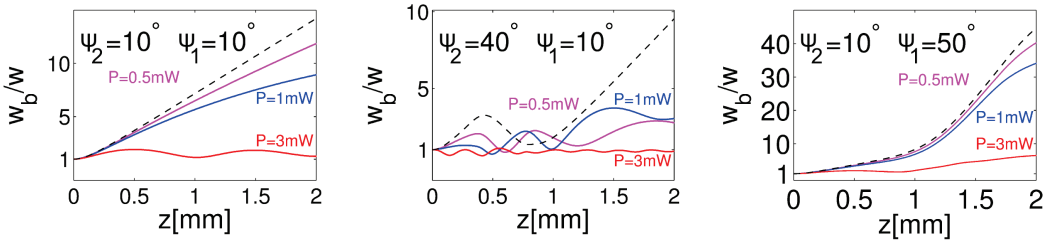

(a) (b) (c)

Figure 2.6: Beam width w normalized with respect to the input waist w_0=5μm for various input powers and angles ψ_1 and ψ_2 corresponding to the plots in figure 2.5 (see labels: dashed lines = linear propagation)

.

Hereafter, we take a linear profile for ψ_{LF} across d, from $y = 0$ to $y = L = 100\mu m$, note that for clarity we shift the axis origin in order to have the z axis coincident with the beginning of the interface. Figure 2.5 shows the evolution of a Gaussian beam launched in $y = -50\mu m$ with $\mathbf{k}//\hat{z}$. For $\psi_2 > \psi_1$ the refractive gradient is negative, thus the soliton wave vector bends towards $y < 0$; to achieve TIR, the change in $\mathbf{k}$

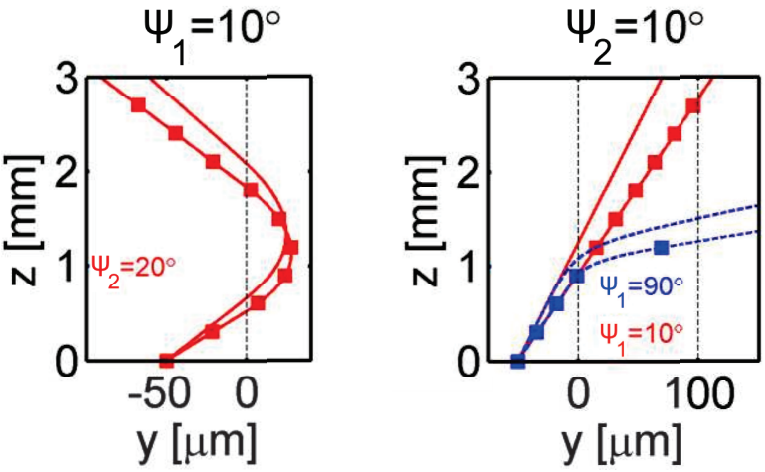

(a) (b)

Figure 2.7: (a) Dynamic of the nematicon with the optical interface in TIR mode ($\psi_1 = 10°$, $\psi_2 = 20°$) for $P = 0.5mW$ (no symbols) and $P = 3mW$ (squares markers). (b) Transmission of the nematicon across the interface for $P = 0.5mW$ (no symbols) and $P = 3mW$, dashed (solid) lines correspond to $\psi_1 = 90°$ (10°).

has to ensure a Poynting vector **S** leaving the interface with a negative y component. Noteworthy, reflection and incidence angles are generally different due to anisotropy [27]. For $\psi_2 < \psi_1$, conversely, the beam can always overcome the index barrier and be refracted.

Figures 2.7 graphs the calculated soliton trajectories vs input power: the power dependence is due to all-optical changes in walk-off [23]. For excitation with $\mathbf{k}//\hat{z}$, the angle β of the Poynting vector with $\hat{z}$ away from the interface, the overall steering (from refraction to TIR) amounts to $\approx 40°$ (figure 2.8), with excellent agreement between the results from a beam propagator (BPM) and the predictions of the geometric optics approximation (GOA) for β up to 20°. Even larger deflections are obtained by launching solitons with phase fronts slanted with respect to $\hat{z}$, i.e. $\alpha \neq 0$.

For a fixed α, large steering has to rely on TIR. Defining α_{TIR} the maximum incidence angle resulting in TIR, α_{TIR} is plotted in figure 2.9 for given $\psi_{1/2}$, with a maximum $\alpha_{TIR}^{max} \cong 25.1°$; TIR does not take place above these curves.

The output angle β vs ψ_1 and ψ_2 is graphed in figure 2.10: the largest deflections are obtained for $\alpha < \alpha_{TIR}^{max}$ (for a fixed ψ_2 the solitons evolve from TIR to refraction as ψ_1 varies, see figure 2.10(a)-(b)) rather than for $\alpha > \alpha_{TIR}^{max}$ (where only refraction occurs, see figure 2.10(c)), with a maximum steering of 60° for $\alpha = \alpha_{TIR}^{max}$ and $\psi_2 = 90°$.

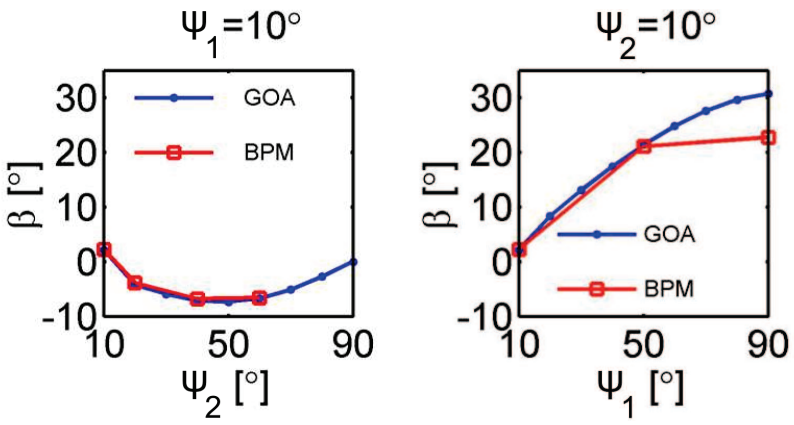

(a) TIR. (b) Refraction.

Figure 2.8: Soliton deflection β versus ψ_2 for $\psi_1 = 10°$ (a) and versus ψ_1 for $\psi_2 = 10°$ (b).

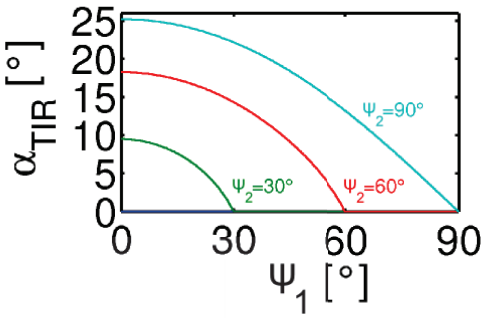

Figure 2.9: α_{TIR} region versus ψ_1, the labels indicate the value of ψ_2.

By varying ψ_2 as well, an overall steering angle of 70° is achieved for α_{TIR}^{max} (figure 2.11), taking advantage of the dependence of the refraction angle from walk-off (see the three upper lines in figure 2.10(b)). Such voltage-controlled angular deviations, to be achieved with biases of a few Volt, are among the largest observed at a single dielectric interface and well above the record value of 40° reported for nematicons [28]. Noteworthy, greater steering could be engineered by adopting multiple interfaces.

2.2 Experimental results

As supplement to our theoretical investigations, a beam steering device was implemented following the design in figure 2.1. The glass plate were rubbed at $\psi_0 = 10°$ with respect to the z axis and glued together with Mylar spacers in between them,

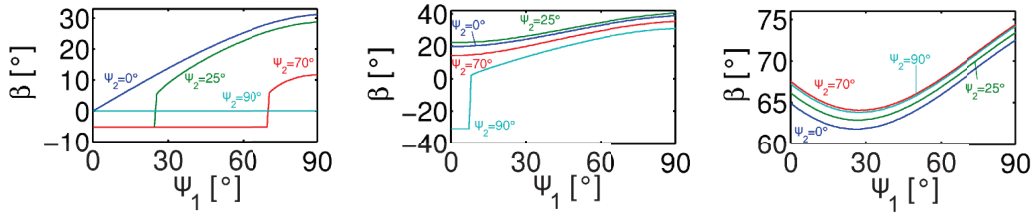

(a) (b) (c)

Figure 2.10: Deflection angle β versus ψ_1 for incidence angle α (a) 0°, (b) 25° and (c) 10°; the labels in each line indicate the corresponding ψ_2.

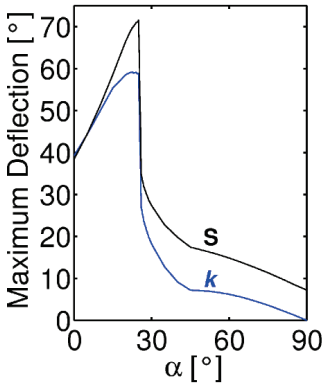

Figure 2.11: Maximum angular deflection of wave vector **k** and Poynting vector **S** versus α.

fixing the cell thickness (L) at 100μ. The periodicity of the comb is set to $\Lambda = 60\mu$m. The NLC cell is filled by capillarity with the standard mixture E7. To form the soliton (*nematicon*) a linearly y-polarized beam was launched into the cell to achieve maximum coupling to an extraordinary wave within the NLC. We set an input power P=5mW and an input waist w0≈4μm; these input parameters ensured the formation of stable nematicons in the whole range of biases. The beam propagation was monitored with a microscope objective lens and a high resolution CCD camera acquiring the outscattered light from the top of the cell.

For $V_1 = V_2 = 0V$, the nematicon propagates at the walk-off of the corresponding plane wave ($\delta_0 = \delta(\psi = 10°) \approx 2.5°$), as shown in figure 2.12, left column. When V_2=0V and $V_2 \neq$0V, the condition $n_{e,2} \leq n_{e,1}$ is satisfied: the solitary wave crosses the interface at $\beta = \delta_0$ and is pulled into the denser medium (figure 2.12, first column, V_1=0.9, 1.9, 2.2V). The graphs in figure 2.12, second column, first and second panels, display the trajectories and the corresponding local slopes, respectively: after an ef-

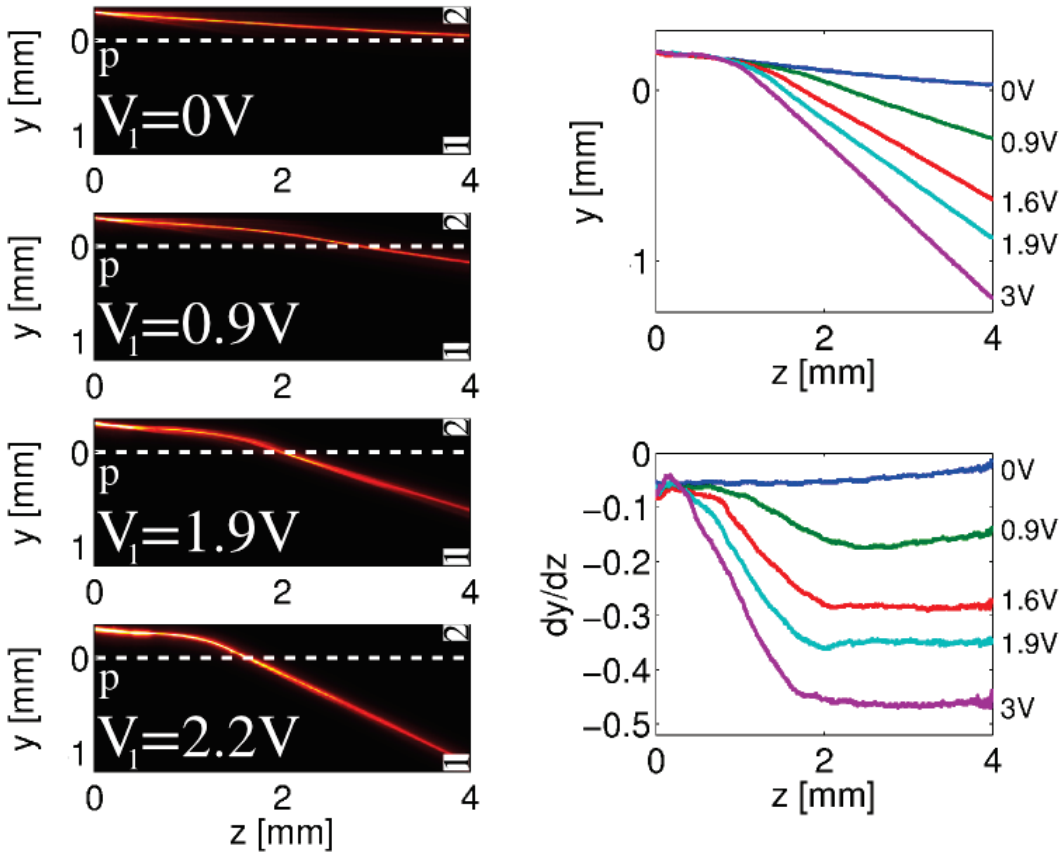

Figure 2.12: Experimental figure of nematicon in a cell working in refraction mode. Bias is applied to the first half of the cell (left panel, top to bottom). In right panel we plot the trajectory of the nematicon (top figure) and their respective slope (bottom).

fective acceleration within the graded region, the beam propagates in region 1 with a nearly constant angle the latter depending on V_1. The maximum beam deflection is $+20°$, reached for V_1=3V (upper limit due to soliton instability) and estimated $\psi_1 > 55$. As the walk-off variations are limited to a few degrees, it follows that the effective acceleration is mainly due to the refractive index change.

When V_1=0 and $V_2 \geq 0$, it is $n_{e,1} \leq n_{e,2}$: the beam travels through the interface figure 2.13(a) until, for V_2=0.9V and $\delta_2 \approx 3.5°$ corresponding to $\psi_2 \approx 15°$, reaches the critical incidence angle. For higher voltages figure 2.13, left column V_1=1.9 and 2.2V, the nematicon undergoes TIR. We stress that the angle of incidence depends on the applied voltage (besides the extraordinary index), and a continuous beam deflection is granted by the changing walk-off in region 1 (figure 2.13 right column, first panel).

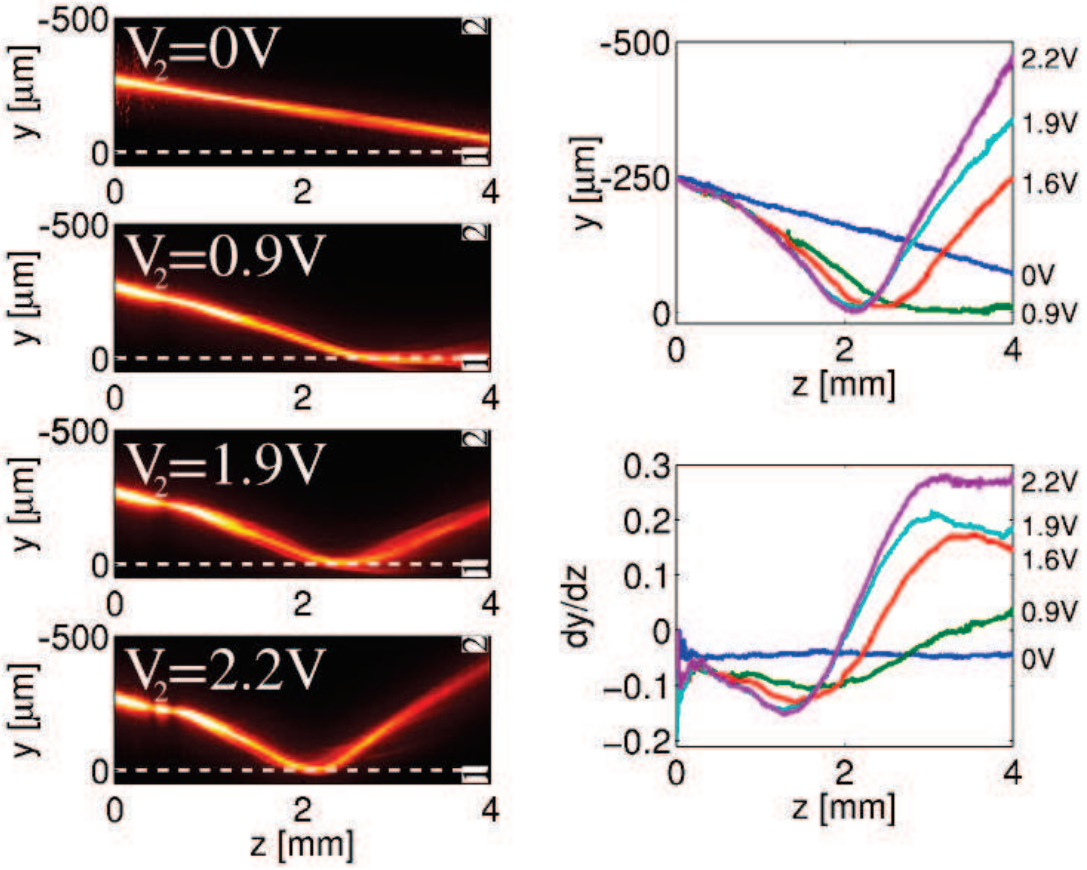

Figure 2.13: Picture of the nematicon in the cell working in TIR mode. The first half of the device is grounded and bias (0V,0.9V,1.9V and 2.2V, fist panel from top to bottom) is applied to the second half of the cell. In the left panel, the trajectories of light beam are shown (top) for different values of the bias with their respective slope (bottom)

Moreover, due to anisotropy, reflected and incident beams effectively propagate in uniaxials with diversely oriented optic axes,28 resulting in a remarkably large angular asymmetry of about $\beta_r - \beta_i \approx 5°$ in reflection. In this case, the maximum reflection angle is $\beta_r \approx 10°$ (figure 2.13 right column, second panel).

As visible in figure 2.14, the overall angle spanned by the Poynting vector of the nematicon in refraction and reflection is about $\Delta\beta \approx 30°$ in the range $-3V \leq \Delta V \leq 2.2V$, with $\Delta V = V_2 - V_1$. The refracted/reflected wavepacket remains extraordinarily polarized and self-confined (see figures 2.13 and 2.12). Finally, by varying the incidence angle a between k and z, we could further exploit the asymmetric reflection in order to enhance the total steering. Figure 2.15 displays the experimental results for an incidence angle $\alpha \approx 16°$: the obtained overall angular deflection $\Delta\beta \approx 55°$ is the

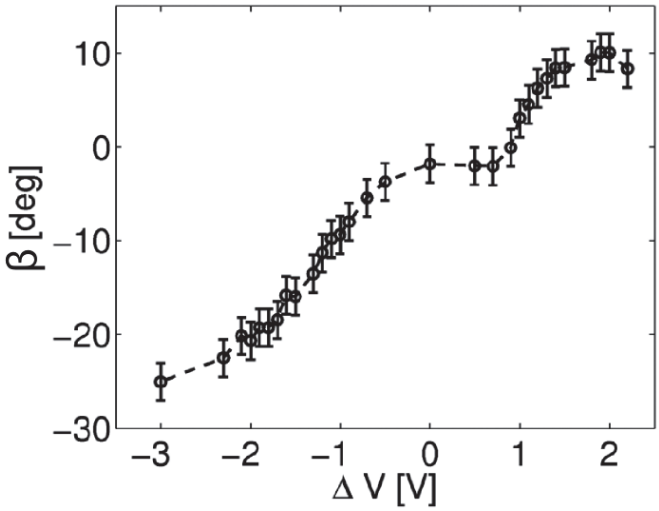

Figure 2.14: Experimentally measured steering of the Poynting vector versus ΔV.

largest ever observed for nematicons in a tunable geometry.

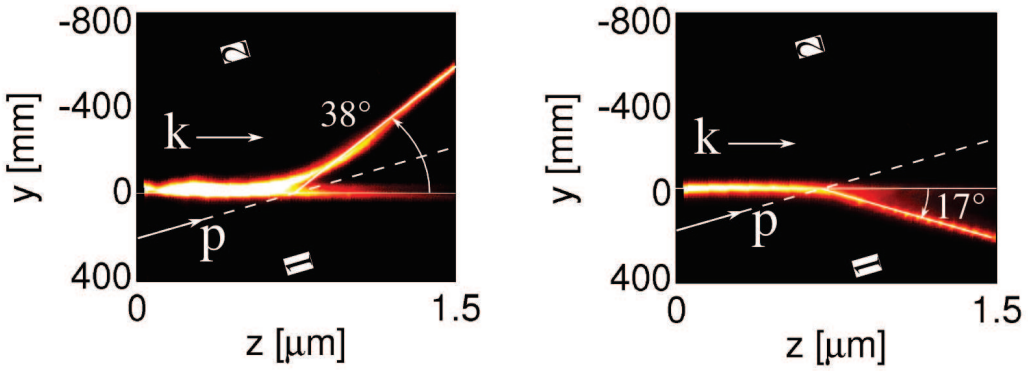

(a) (b)

Figure 2.15: Refraction for V_2=0V; $V_1 = 3.5$V (a) and TIR for $V_2 = 4$V; $V_2 = 0$V (b) with $\alpha = 16°$. The total angle spanned is $|\beta_{TIR}| + |\beta_{REF}| \approx 55°$.

2.3 Conclusion

In conclusion, we have presented booth theoretically and experimentally spatial solitons interacting with an electrically dened interface in nematic liquid crystals with a biasing arrangement ensuring in-plane deection. Periodic interdigitated and in-pair balanced electrodes allowed nematicon waveguide steering via both refraction and total

internal reection, maintaining the beam in the cell midplane. Exploiting both the refractive index variations and the anisotropy, we obtained a maximum deection of $55^{c}irc$ (70° for the theoretical prediction) while preserving self- connement and polarization. These results conrm the versatility of NLC in all-optical signal routing approaches and represent a remarkable achievement in controlling with modest voltageswaveguide bending/steering over large angles.

Chapter 3

Umbilic defects: Induction and control

In the previous chapter we have considered geometries in which the director is allowed to vary in the plane, and there was not so ever, ambiguities in determining the director orientation once one has given the type of excitation, electrical, optical or both and its characteristics, mainly the initial angle of the nematic director with respect to the electric field or the k-vector. In this chapter, we will investigate the case in which these ambiguities or degeneracies arise: that will be at the origin of the formation of defects in the orientation of the liquid crystal layer. These defects, when controlled, are useful because they induce topological defects in light beams, as demonstrated in the pioneering work by Brasselet et al.[29]. Only the interaction with a low frequency field will be considered here.

Our main scenarios will be hometropic geometries: the interfaces are treated to promote a vertical boundary conditions and the nematic director is anchored orthogonally to the bounding surfaces. The liquid crystal considered has a negative dielectric anisotropy. When the cell is subjected to an increasing uniform electric field normal to the bounding plates, hence, parallel to the initial alignment of the director, the homeotropic equilibrium configuration will be destabilized after a critical value of the bias over the cell called the Frederiks transition voltage V_{TH} [3]. This transition occurs when the electric torque overcomes the elastic one. Strictly speaking both torques are ideally zero in the hometropic condition. But due to the non null fluctuations of the director, after a small tilt from the electric field, a non null torque will appear and the only way to minimize the energy is that the director (in the midplane) tilts away from the electric field. In this configuration the director can tilt in all directions or-

thogonal to the electric field (Figure 3.1(a)) in order to equate the elastic torque to the electric torque: the dielectric anisotropy $\epsilon_a = \epsilon_{\parallel} - \epsilon_{\perp}$ is negative. This 2π degeneracy of the possible directions in which the director can reorient lead to a degenerate pitchfork bifurcation of the complex scalar order parameter A (Figure 3.1(b)) defined as $A = n_x + in_y$, which represent the projection of the nematic director on the $x - y$ plane. The order parameter $A = |A|e^{i\theta}$ can have phase singularities or disinclination points, where we are impossibilitate to determine the direction of the projection of the nematic director. In other terms, at these points the nematic director remains orthogonal to the bounding plates and the order parameter A goes to zeros with the director (its projection) circling around the singularity. These types of disinclinations are called *umbilics* and represent vortices of the complex scalar field A. They are characterized by their winding number $q = \dfrac{1}{2\pi}\displaystyle\int_{\mathcal{C}} d\theta$, with $\mathcal{C}$ any closed curve around the umbilic sufficiently far from the other vortices. The umbilics have only integral winding number or Frank index. Indeed, a semi integer, for example 1/2 means that the director projection rotates about π for a full rotation around the umbilic which is incompatible with the starting condition as the nematic is a continuous medium. Note that in a 2D geometry, the director and its projection are equivalent, with a π rotation leaving them both invariant [30, 31, 32]. The umbilics can have only ± 1 as Frank index [3, 33], due to the fact that their energy increases quadratically with the winding number q. Moreover, it is demonstrated in the literature that defects with $|q| \geq 2$ are unstable [34].

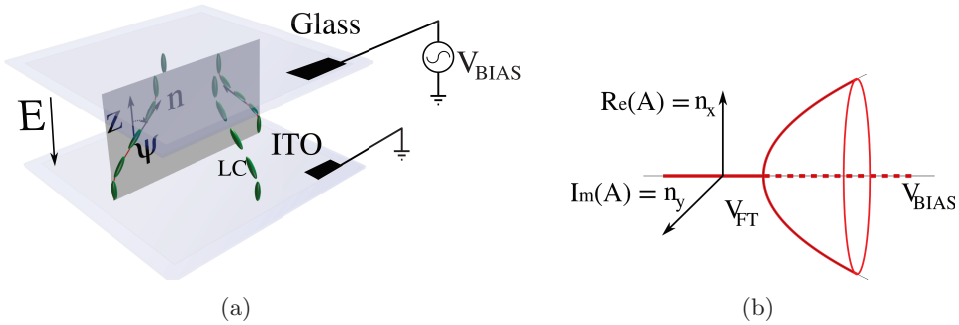

(a) (b)

Figure 3.1: (a) Sketch of a biased homeotropic liquid crystal showing the 2π degenerate Frederiks transition. (b) Degenerate pitchfork bifurcation of the complex scalar order parameter.

If we assume that n_z has always the same sign, which is taken to be positive, the

order parameter A gives an unique representation of the nematic director in space. The negative sign is also valid, since $\vec{n}$ and $-\vec{n}$ are equivalent. But the unicity of the representation of $\vec{n}$ through its transverse components $n_{x,y}$ or A is valid only if there is no twist of the director around the z axis (see for instance [35, page 399]). In our cases, we exclude the possibility of having twist disinclinations.

3.1 Quantitative analysis

In order to study quantitatively this phenomenon we will use the simplest equations of the liquid crystal dynamics, neglecting backflow effects and electroconvective effects[1]. In this case, the dynamics of the liquid crystal is ruled by [3, 4]:

$$\frac{\delta \mathcal{R}}{\delta \dot{\hat{n}}} + \frac{\delta \mathcal{F}}{\delta \hat{n}} + \boldsymbol{\lambda} \hat{n} = 0, \tag{3.1}$$

where $\mathcal{F}$ represent the free energy density introduced in equation 1.5 and $\mathcal{R}$ the energy dissipation function density

$$\mathcal{R} = \gamma \frac{1}{2} |\dot{\hat{n}}|^2, \tag{3.2}$$

with γ the orientational or rotational viscosity. As explained before, the Lagrange multiplier serves only to impose the fact that the director is a unit vector. To get rid of it, we can multiply by $\hat{n}$

$$\gamma \hat{n} \times \partial_t \hat{n} = -\hat{n} \times \frac{\partial \mathcal{F}}{\partial \hat{n}}, \text{ with } \hat{n} \cdot \hat{n} = 1. \tag{3.3}$$

By introducing the molecular field $\vec{h} = -\dfrac{\delta \mathcal{F}}{\delta \hat{n}}$, we have:

$$\begin{aligned} \vec{h} =& K_3 \nabla^2 \hat{n} + (K_1 - K_3) \nabla \nabla \cdot \hat{n} + 2(K_3 - K_2) \left(\hat{n} \cdot \nabla \times \hat{n}\right) \nabla \times \hat{n} \\ &+ (K_3 - K_2) \nabla (\hat{n} \cdot \nabla \times \hat{n}) \times \hat{n} + \epsilon_a^{\Omega} (\hat{n} \cdot \vec{E}) \vec{E}. \end{aligned} \tag{3.4}$$

The dynamical equation reads as:

$$\gamma \frac{\partial \hat{n}}{\partial t} = \vec{h} - (\hat{n} \cdot \vec{h}) \hat{n}, \tag{3.5}$$

[1] Experimentally will place ourselves in parameter regions in which these assumptions hold valid.

with V satisfying

$$\nabla \cdot \underline{\underline{\epsilon}} \cdot \nabla V = \epsilon_\perp \nabla^2 V + \epsilon_a \nabla \cdot (\hat{n}\hat{n} \cdot \nabla V) = 0. \tag{3.6}$$

3.1.1 Linear stability analysis

In the equilibrium condition we need to solve the equation 3.5 with the left hand side set to zero. It appears clearly that the homogeneous state is an equilibrium state: both the nematic director and the electric field (with an arbitrary amplitude) are parallel to the z axis and the electric and the elastic torque are null. But not all of them are stable to small perturbations, due to the Frederiks transition phenomenon.

3.1.1.1 Perturbation

Small perturbations around the homeotropic configuration, for an uniform perturbation voltage can be written as:

$$\begin{aligned}\gamma \partial_t \vec{n}_1 =& K_3 \nabla_t^2 \vec{n}_1 + K_3 \partial_z^2 \vec{n}_1 + (K_1 - K_3)\nabla_t \nabla_t \cdot \vec{n}_1 + (K_3 - K_2)\nabla_t(\vec{z} \cdot \nabla_t \times \vec{n}_1) \times \vec{z} \\ & - \epsilon_a^\Omega E_0^2 \vec{n}_1 + \epsilon_a^\Omega E_0 (\vec{E}_1 - (\vec{z} \cdot \vec{E}_1)\vec{z})\end{aligned}, \tag{3.7}$$

where E_0 is the amplitude of the low electric field and $\vec{E}_1$ its perturbation which, will be set to zero for now. Note that we, actually, split the gradient operator in its transverse and longitudinal contributions $\nabla = \nabla_t + \vec{z}\partial_z$.

the optical contribution to null

For the stability, we seek for solutions of the form:

$$\vec{n}_1(\vec{r}, z) = \vec{N}_m(\vec{q}) \mathrm{e}^{i\vec{q}\cdot\vec{r} + \sigma_m(\vec{q})t} \sin\left(m\pi \frac{z}{L}\right)$$

and after few passages, we get :

$$\begin{aligned}\gamma\sigma\vec{N} =& -K_3\left(q^2 + (m\pi/L)^2\right)\vec{N} - (K_1 - K_3)(\vec{q}\cdot\vec{N})\vec{q} \\ & - (K_2 - K_3)(\vec{z}\times\vec{q}\cdot\vec{N})\vec{z}\times\vec{q} - \epsilon_a^\Omega (V_0/L)^2 \vec{N}.\end{aligned} \tag{3.8}$$

We denote by $\tau_o = \gamma \dfrac{L^2}{K_3 \pi^2}$, which represents the characteristic relaxation time of the system, and $\mathrm{V_{FT}} = \pi \sqrt{\dfrac{K_3}{|\epsilon_a^\Omega|}}$ the Frederiks transition voltage for the homeotropic

geometry. This eigenvalue equation has two eigenvalues (growth rates)

$$\tau_o \sigma_{m,\parallel}(\vec{q}) = -\frac{K_1}{K_3}\left(\frac{qL}{\pi}\right)^2 - m^2 + \left(\frac{V_0}{\mathrm{V_{FT}}}\right)^2, \tag{3.9}$$

$$\tau_o \sigma_{m,\perp}(\vec{q}) = -\frac{K_2}{K_3}\left(\frac{qL}{\pi}\right)^2 - m^2 + \left(\frac{V_0}{\mathrm{V_{FT}}}\right)^2 \tag{3.10}$$

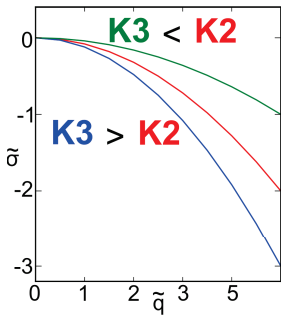

Figure 3.2: Stability curves for the perturbed dynamical equation around the homeotropic condition.

with their respective eigenvectors $\vec{N}_\parallel = N_\parallel \vec{q}/q$ and $\vec{N}_\perp = N_\perp \vec{z} \times \vec{q}/q$. The first modes that become unstable are the low order ($m = 1$) longitudinal ones. They have equal threshold coinciding with the Frederiks transition voltage. These eigenvalues are degenerate when $K_2 = K_1$, that is when, twist and splay modes manifest with equal strength. For $K_2 > K_1$ we will have a splay dominant deformation, and a twist dominant deformation otherwise.

3.1.1.2 Effect of dielectric coupling on instability curves.

So far, we have considered that in the anisotropic Laplace equation (equation 3.6) the director remains at rest. Weak tilts or director variations couples the dynamics of the LC molecules with the voltage distribution across the liquid crystal layer. The transverse contributions of this coupling lead to the perturbation of the equation 3.6. We assume that the voltage changes instantaneously in response to director changes. The perturbed equation for the voltage read as:

$$\frac{\epsilon_\perp^\Omega}{\epsilon_\parallel^\Omega}\nabla_t^2 V_1 + \partial_z^2 V_1 + \frac{\epsilon_a^\Omega}{\epsilon_\parallel^\Omega}\frac{V_0}{d}\nabla_t \cdot \hat{n}_1 = 0 \tag{3.11}$$

The perturbation voltage can be split into two contributions: $\delta V_S \frac{z}{L}$ with δV_S the

change in the surface voltage due to the perturbation, the bulk contribution null at the boundaries $z = 0, L$. After a projection of both the equations on the longitudinal mode, we can note that there is no change in $\sigma_\perp$, but $\sigma_\parallel$ changes in:

$$\tau_o \sigma_{m,\parallel}(\vec{q}) = -\frac{K_1}{K_3}\left(\frac{qL}{\pi}\right)^2 - m^2 + \left(\frac{V_0}{\mathrm{V_{TH}}}\right)^2 + \frac{\epsilon_a}{\epsilon_\parallel}\left(\frac{V_0}{\mathrm{V_{TH}}}\right)^2 \frac{(qL/\pi)^2}{(qL/\pi)^2\epsilon_\perp/\epsilon_\parallel + m^2}. \quad (3.12)$$

In conclusion, there is no qualitative change in the dispersion curves. Indeed as the anisotropy is negative, the curvature of both contributions have the same sign around zero.

3.1.2 Nonlinear analysis: Ginzburg-Landau equation.

For low bias, and in the vicinity of the Frederiks transition voltage, typically $\mathrm{V_{TH}} \leq V_0 \leq 2\mathrm{V_{TH}}$, we can assume that only the lowest longitudinal mode is excited. The validity of this approximation is supported by the fact that the two modes are subjected to the Frederiks transition which is a second order phase transition and the high order longitudinal modes are damped and follow adiabatically the first order mode: the information on the dynamics depend on the lowest modes [36]. We can derive the nonlinear dynamics by considering that the nematic director is weakly tilted from the homeotropic condition. First, we cast the director components in the following form $n_x = \epsilon N_x(\vec{r}) \sin\frac{\pi z}{L}$, $n_y = \epsilon N_y(\vec{r}) \sin\frac{\pi z}{L}$, $n_z = 1 - \epsilon^2 \frac{1}{2}\left[N_x^2(\vec{r}) + N_y^2(\vec{r})\right] \sin^2\frac{\pi z}{L}$, where ϵ represent the small parameter, $\vec{r}$ the transverse coordinate.

The director components are substituted in equation 3.5 and terms up to third order in ϵ are kept and projected on the first longitudinal mode. Then, by setting $\epsilon = 1$ we obtain the following equation:

$$\gamma \partial_t A = \mu A - \alpha |A|^2 A + \frac{K_1 + K_2}{2}\nabla^2 A + \frac{K_1 - K_2}{2}\partial^2_{\eta\eta}\bar{A}, \quad (3.13)$$

with $A = N_x + iN_y$ the complex scalar order parameter; $\mu = -\epsilon_a^\Omega E^2 - K_3\frac{\pi^2}{L^2}$, the control parameter; $\alpha = -\frac{3}{4}\epsilon_a^\Omega E^2 - \frac{\pi^2}{4L^2}(3K_3 - 2K_1)$ and $\partial_\eta = \partial_x + i\partial_y$. A similar equation for the dynamics of liquid crystals was derived by Frisch et al. [36], with other contributions due to the presence of a rotating magnetic field. The equation (3.14) can be scaled as follows: $A \to A\sqrt{\alpha/\mu}$, $\vec{r} \to L_c\vec{r}$, $t \to \tau t$, with $L_c = \frac{L}{\pi}\left(\frac{K_1 + K_2}{2K_3}\right)^{\frac{1}{2}} / \left[\left(\frac{V}{\mathrm{V_{TH}}}\right)^2 - 1\right]^{\frac{1}{2}}$,

$\tau = \tau_o / \left[\left(\frac{V}{V_{TH}} \right)^2 - 1 \right]$. We finally obtain the well known Ginzburg-Landau equation:

$$\partial_t A = A - |A|^2 A + \nabla^2 A + \delta \partial^2_{\eta\eta} \bar{A} \tag{3.14}$$

with an anisotropy related term depending on $\delta = (K_1 - K_2)/(K_1 + K_2)$. The parameters L_c and τ represent, respectively, the length scale and the time scale of the dynamics and both depend on the applied voltage V, the cell thickness and the physical properties of the LC medium, as the elastic constants and the rotational viscosity. It is interesting to note that the obtained equation is invariant by arbitrary rotation around the origin an also by translation. The 2π degenerated pitchfork bifurcation we have described above can be recovered by setting A to a constant.
The scaled GLE have static solutions of the form $A = a(r)e^{i(q\xi+\theta_0)}$, where q is an integer and represents the winding number, or topological charge, of the local defect and θ_0 is an arbitrary constant, with boundary condition $a(0) = 0$ and $a(\infty) = 1$. The case $q = \pm 1$ corresponds to the umbilic defects and their texture is shown in figure 3.3. The case $\delta = 0$ was extensively studied in the scientific literature [37, 38], and it has been demonstrated that, in this case, there is no close solution for vortex type solutions of the GLE. Nevertheless, it can be shown from their asymptotic properties that the core size of the scaled vortices goes like $|q|$, hence, the umbilics ($|q| = \pm 1$) have their core size about L_c. This prediction matches the experimental results [39].

Now, let us make some consideration about the formation of umbilics. In principle, we can write the nematic director distribution in the sample with respect to the transverse deformation modes, ie:

$$\vec{n}(\vec{r}) = \frac{1}{(2\pi)^2} \iint \left[\frac{\vec{q}}{q} n_{\parallel}(\vec{q}) + \vec{z} \times \frac{\vec{q}}{q} n_{\perp}(\vec{q}) \right] \mathrm{e}^{i\vec{q}\cdot\vec{r}} d\mathbf{q}, \tag{3.15}$$

where $n_{\parallel}$ and $n_{\perp}$ account for the longitudinal and the transverse deformations with respect to the wave vector $\vec{q}$. We can write the order parameter as:

$$A(\vec{r}) = \frac{1}{(2\pi)^2} \iint \left[n_{\parallel}(q,\phi) + i n_{\perp}(q,\phi) \right] \mathrm{e}^{i(qr\cos(\xi-\phi)+\phi)} q d\phi dq, \tag{3.16}$$

where the following substitutions are made: $\vec{q} = q(\cos\phi\vec{x} + \sin\phi\vec{y})$ and $\vec{r} = r(\cos\xi\vec{x} + \sin\xi\vec{y})$.

In the case of an isotropic spectrum $n_{\parallel,\perp}(q,\phi) = n_{\parallel,\perp}(q)$, case which will be likely

the most favoured thermodynamically (note that the space is isotropic), we have:

$$A(\vec{r}) = e^{i\xi} \int \frac{1}{2\pi} \left[n_{\parallel}(q) + i n_{\perp}(q) \right] J_1(qr) q dq, \tag{3.17}$$

where J_1 is the first order Bessel function of first kind (note that the Jacobi-Anger expansion is used to reduce the integral). It appears clearly that we will have spontaneous formation of defect over the threshold value of the driving voltage. The defects will be essentially a mixture of splay type ($n_{\parallel}$) and twist type ($n_{\perp}$) deformation. The formation of defects +1 is favored with respect to that of defects -1. Indeed, the anisotropy of the elastic constants lift the degeneracy with respect to the energy, with the -1 umbilic being more energetic respect to the +1 umbilic [40]. This will have important consequences in the generation and management of these defects. Moreover, the translational symmetry of the system will make the umbilic +1 to be generated in arbitrary space positions. In conclusion, by applying a voltage to the LC cell, +1 umbilics will form spontaneously and -1 umbilics will be generated by frustration of the order parameter.

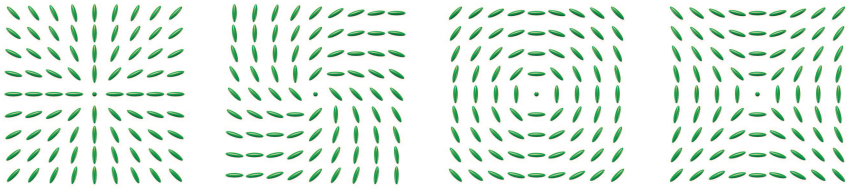

(a) q=+1,$\theta_0 = 0$ (b) q=+1,$\theta_0 = \pi/4$ (c) q=+1,$\theta_0 = \pi/2$ (d) q=-1,$\theta_0 = 0$

Figure 3.3: The defects with texture in (a), (b), (c) are topologically equivalent with winding number +1, the parameter θ_0 lift the degeneracy of the type of deformation: (a) splay dominant, (c) twist dominant, (b) intermediate case. Texture of defect with winding number -1 (d).

3.2 Numerical and experimental results.

The experiment on the generation of umbilics is carried out by using a 10μm thick hometropic cell filled with the liquid crystal MLC6608 which posses a negative dielectric anisotropy. The parameters are enlisted in table 3.1.

The cell is biased with a sinusoidal voltage whose frequency is set to 100Hz. To observe the texture of the nematic layer we use the crossed polarizers configuration under a uniform incoherent light illumination. The polarizers can be either linear or circular.

Elastic constants	
K_1(pN)	16.7
K_2(pN)	7.0
K_3(pN)	18.1
Viscosity γ Pa·s	0.186

Dielectric constant	
$\epsilon_\perp$	7.8
$\epsilon_\parallel$	3.6
ϵ_a	-4.2

Refractive index	n_o	n_e	$dn = n_e - n_o$
λ=532nm	1.4731	1.5531	0.080
λ=633nm	1.4775	1.5595	0.082

Table 3.1: MLC6608 parameters

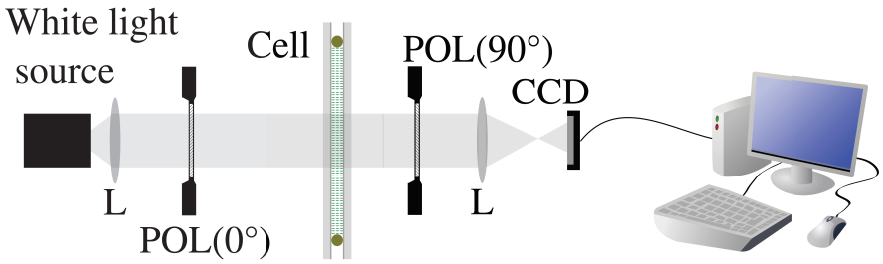

Figure 3.4: Experimental setup for the generation of umbilic defects. L: imaging lens or objective. CCD camera for image acquisition.POL(0°) and POL(90°) are respectively polarizer and analyzer.

Linear crossed polarizers

The biased LC cell, due to the non homogeneous arrangement of the director, changes spatially the polarization of the incident linearly polarized incoherent light. When inserted in between crossed polarizers, the transmitted intensity through the analyzer is given by: $I_0 \sin^2 \frac{\Gamma}{2} \sin^2 [2(\theta - \alpha)]$, with θ the azimuthal angle of the director in the $x-y$ plane and α the angle of the polarizer axis with respect to the x axis which is arranged to be zero. Γ represent the effective phase shift between the ordinary and extraordinary component of the light and is expressed as: $\Gamma = 2\pi \frac{L}{\lambda}(\bar{n}_e - n_o)$, n_o is the ordinary index, and $\bar{n}_e = \int_o^L n_e(\psi) dz$ is the effective extraordinary index. Clearly, in the presence of defects we will see dark brushes emerging from the core of the defect and interlaced with those emerging from the surrounding defects. Indeed, the collected intensity is null at the position of the nematic core (if we neglect the scattering) and where the nematic director (actually its projection) is either parallel or perpendicular to the polarizer or the analyzer. The number of brushes observed is always four, confirming that the created defects always have ± 1 index. This experimental observation in qualitatively

agreement with the simulation of the GLE with the physical parameters (see figure 3.5).

Circular crossed polarizers

Instead of using crossed linear polarizer, couples of polarizers and quarter wave plates can be used in order to have the crossed circular polarizers configurations. The collected intensity is simply $I_0 \sin^2 \frac{\Gamma}{2}$. The defects appear as dark spots over a non homogeneously illuminated background.

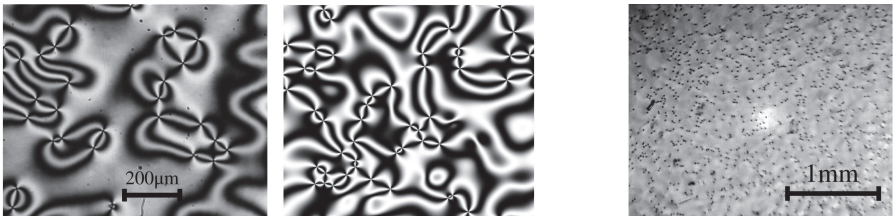

(a) (b)

Figure 3.5: (a)Experimental snapshot recorded under white-light illumination for a uniform bias cell in between crossed linear polarizers (left panel). Numerical simulations of equation(3.14)(right panel). (b) The defects under crossed circular polarizers.

3.2.1 Defect gas

As we apply a high voltage to the homeotropic cell, we observe first the formation of defect loops.

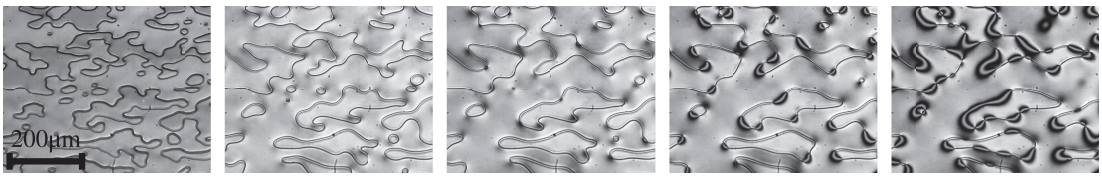

Figure 3.6: Temporal snapshots with steps of $400\mu s$ of the early dynamics in the biased nematic cell, from $t = 0$ (left) when a bias voltage of 15V is applied. Some of defect loops evolve in a random network of umbilics of alternate sign, others collapse.

After a fast dynamics the loops relax into umbilics of winding number +1 and -1. The defects with the same topological charge tend to repel, those with opposite charge attract each other and annihilate. The system is dissipative and have somehow to relax to the configuration with the lowest energy, which is a defect free configuration.

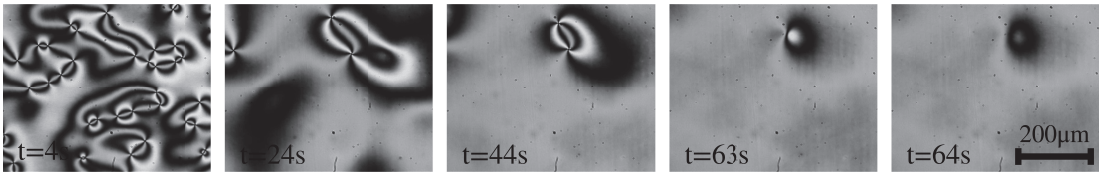

Figure 3.7: Temporal snapshots of the annihilation dynamics of the vortex gas.

The rich dynamics of this defect collection, or gas of vortices, is ruled by

$$\frac{\partial \mathbf{r}_i}{\partial t} = -\frac{\partial W}{\partial \mathbf{r}_i} - \frac{\partial W_{\mathrm{BC}}}{\partial \mathbf{r}_i} \ , \tag{3.18}$$

where W the well known Kirchhoff-Onsager function [38, 41, 42, 43]:

$$W(\mathbf{r}_0, \mathbf{r}_1, \dots) = -\sum_{i \neq j} n_i n_j \ln |\mathbf{r}_j - \mathbf{r}_i| \, , \tag{3.19}$$

and W_{BC} accounts for pinning and boundary terms [44, 45]. This approximation is valid when the GLE can be reduced to its phase dynamics, ie., the amplitude is one everywhere except for the vortex location where it is undefined. Physically speaking, the core radius is neglected with respect to other length scales, and all the molecules are supposed to been lying on the $x-y$plane. This is exactly what happens when the hometropic LC cell is subjected to high electric field.

Scaling Law

The scaling law of the vortex gas is measured by counting the number of umbilics during the annihilation dynamic. The dynamics is recorded by illuminating the nematic cell with a circular polarized white light and analyzed under a crossed circular analyzer. The recorded images were processed in order to retrieve the number of umbilics during the dynamics. The number of particles is then fitted against:

$$N(t) = \beta t^{-\alpha} + N_\infty,$$

α being the critical exponent. N_∞ accounts for the remaining defects due to boundary effects and pinning from impurities and the over-counting of the particles; β accounts for the initial number of defect in the cell. For all the ranges of the applied voltage, the critical exponent is close to its theoretically value 1 and does not change significantly with the bias [46].

We now consider the dynamics of two close *isolated* defects of opposite winding number, see figure 3.10. The distance between the two defect is computed by tracking

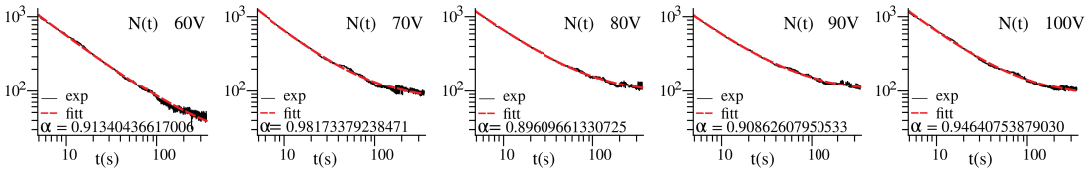

Figure 3.8: Evolution of the number of defects counted in the observed area for different applied voltages: 60V, 70V, 80V, 90V,100V. The experimental data (black) are superposed with the fitted curves (dashed red line)

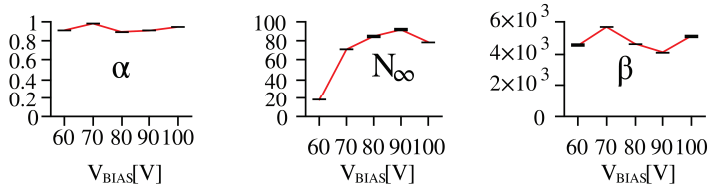

(a) (b) (c)

Figure 3.9: Plot of the fit parameters with respect to the bias voltage: (a) critical exponent α, (c)N_∞ and β (b).

their position during the collision. We can appreciate the close matching of the experimental curve (continuous line) with the square root law (dashed line). In fact, if we consider the Kirchhoff-Onsager function, and restrict ourselves to two defect with charge ± 1, we can easily find that the distance between the defects follows the law $r(t) = r(0)/\sqrt{1 - t/t_{COL}}$, with t_{COL} the time of collision.

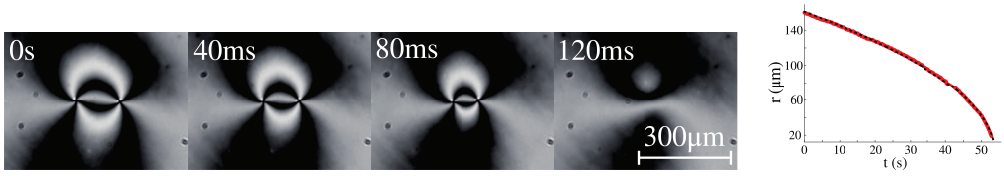

(a) (b)

Figure 3.10: (a) Snapshots of the collision dynamics of two umbilic defects with opposite winding number.(b) Interdistance vs t.

The vortices are created in a random manner, as the initial condition is essentially governed by thermal fluctuations and impurities at the LC rubbed-glass interface. Moreover, the defects interact one with another via long range interactions: the interaction potential depends logarithmically on the distance. The texture, then, is unstable and relaxes toward a defect free configuration, with resident defects due to

boundaries and impurities. In order to become exploitable for photonic applications, the textured liquid crystal will be required to be reproductible in the number of defects that it contains, in their positions and their charge. To begin with, we can see that one of the control parameters that we have is the voltage applied to the cell. Until now, we do not have the control over the voltage distribution on the top of the liquid crystal layer. In the next section we will see how a non uniform voltage on the top of the liquid crystal layer can dramatically change the behavior of the system when it is forced to generate defects.

3.3 Non uniform driving

3.3.1 Correction to the Ginzburg-Landau equation.

We now analyze the reorientation phenomena in presence of non uniform distribution of voltage on the top of the LC-layer. For sake of simplicity we neglect the dependency of the voltage distribution on the nematic director, by taking it in the nonlinear anisotropic Laplace equation a its equilibrium value, that is $\hat{n}$ is set to $\vec{z}$.We now have:

$$\frac{\epsilon_\perp}{\epsilon_\parallel}\nabla_T^2 V + \partial_z^2 V = 0, \text{ with } V(x,y,0) = 0, \text{ and } V(x,y,L) = V_s(x,y), \tag{3.20}$$

with $V_s(x,y)$ the surface distribution of the voltage on the nematic liquid crystal layer. The voltage, then, can be written in the following form:

$$V(x,y,z) = \int \frac{\sinh(Qz)}{\sinh(QL)} \tilde{V}_s(\vec{q}) \mathrm{e}^{\imath \vec{q}\cdot\vec{r}} d\vec{\mathbf{q}}^2 \tag{3.21}$$

with $Q = \sqrt{\frac{\epsilon_\perp}{\epsilon_\parallel}} q$. In the limit of small surface gradient, i.e. when the characteristic length of the surface voltage is greater than the cell thickness, the predominant spatial frequency component are in the way that $qL << 1$ (see A.1 for more rigorous derivation) we can approximate $\sinh(QL) \approx QL$. Then the voltage distribution is, simply,

$$V(x,y,z) = \frac{z}{L} V_s(x,y) = \frac{z}{L} V_s(\vec{r}).$$

In the derivation of the GLE, the electric field was assumed to be uniform and parallel to the z axis. For the non homogeneous bias scheme, we have a contribution of the transverse electric field $-\frac{z}{L}\nabla_t V_s$, that even if small, breaks the symmetry of the space, the translational and the rotational ones; the latest can be kept with radial

symmetric excitation. The transverse electric field bias the system and cannot be neglected. Following the same procedure used in the derivation of the GLE we have (see B.2 for the details):

$$\gamma\partial_t A = A_o + \mu A + \mu_* \bar{A} + \beta|A|^2 + \beta_* A^2 - \alpha|A|^2 A + \frac{K_1+K_2}{2}\nabla^2 A + \frac{K_1-K_2}{2}\partial^2_{\eta\eta}\bar{A} \quad (3.22)$$

with:

$$A_0 = \epsilon_a^\Omega \frac{2}{\pi} E \partial_\eta V_s,$$

$$\mu = -\epsilon_a^\Omega E^2 - K_3\frac{\pi^2}{L^2} + \epsilon_a^\Omega \frac{1}{2}\left(\frac{1}{3} - \frac{1}{2\pi^2}\right)\left|\partial_\eta V_s\right|^2,$$

$$\mu_* = \epsilon_a^\Omega \frac{1}{2}\left(\frac{1}{3} - \frac{1}{2\pi^2}\right)\left(\partial_\eta V_s\right)^2,$$

$$\alpha = -\frac{3}{4}\epsilon_a^\Omega E^2 - \frac{\pi^2}{4L^2}(3K_3 - 2K_1),$$

$$\beta = -\epsilon_a^\Omega \frac{2}{\pi} E \partial_\eta V_s,$$

$$\beta_* = -\epsilon_a^\Omega \frac{4}{3\pi} E \partial_{\bar{\eta}} V_s.$$

These corrections have dramatic consequences on the system. Let us focus on A_0 and μ which are the main parameters influencing the system. A_0 constitutes the bias term and μ the supercriticality. At the early stages of the reorientation dynamics, when the voltage is switched on (or the non uniform component is added to the uniform bias), the electric field and the nematics are no more parallel to each other. If the field is intense enough, it will govern the dynamics in contrary to what happens in the hometropic LC with uniform field configuration. In order to balance the total torque, the molecules will rotate increasing the acute angle between them and the field. It is clear that a defect created by a radially symmetric bias potential, will have the same radial structure. Hence, an umbilic like defect with winding number +1 will be created. With this assumption, $A_0 = \epsilon_a^\Omega \frac{2}{\pi} E(r)\partial_r V_s(r)\exp(i\xi)$, which is a forcing term with winding number +1. We will, from now on, refer to radially symmetric excitation. An analysis of the parameter μ show that to promote only the desired defect, the applied voltage has to be maximum at the defect location and decrease far from it. The opposite, the bias have a dip in the center, other defects will be excited far from the origin: this scheme is unsuitable for the controlled defect generation.

3.3.2 Pinning force

In this section we derive an approximate expression of the pining force of a radially symmetric potential on a stationary vortex. Let us consider a steady vortex in $\vec{r}_o$ (position of the vortex in the $x-y$ plane, we use $\vec{r}$ as transverse coordinate and z as longitudinal one), and a sudden rise $V_1(r)$ in the bias voltage. A the early stages (time scale less than the LC response time) there wouldn't be any deformation in the vortex structure. The force on the defect will be the variation of the interaction energy : $W_{INT} = -\frac{1}{2}\epsilon_a \iiint (\hat{n}\cdot\nabla V)^2 \mathrm{d}^2\vec{\mathbf{r}}dz$, with respect to the position of the defect. For the sake of simplicity, we assume that the director distribution does not influence the voltage distribution. Furthermore, we assume that the texture of the umbilic have the following expression in the $\vec{r}_o$-translated reference frame with respect to the origin: $\hat{n} = \begin{bmatrix} \sin(\psi)\cos(\Xi+\theta_0) \\ \sin(\psi)\sin(\Xi+\theta_0) \\ \cos(\psi) \end{bmatrix}$, with $\psi = \psi(R)$ and $\theta_0 = \theta_0(R)$ denoting the swirl of the defect in the nematic texture, which can be, in first order of approximation, set to constant, $\vec{R} = \vec{r} - \vec{r}_o = R\cos\Xi\vec{x} + R\sin\Xi\vec{y}$. Note that director field can be rewritten in a more convenient form: $\hat{n} = \frac{1}{|\vec{R}|}(\vec{R}\cos\theta_0 + \vec{R}_\perp\sin\theta_0)\sin\psi + \vec{z}\cos\psi$. For a bias voltage with radial dependence applied in $\vec{r}$, $\nabla V = V_r(r)\frac{\vec{r}}{|\vec{r}|} + \vec{z}V_z(r)$, with V_r and V_z being respectively the partial derivative of the potential with respect to the radial, R, and the longitudinal, z, coordinates, in the potential reference frame. The expression of the energy is then:

$$W_{INT} = -\frac{1}{2}\epsilon_a \iiint d\vec{\mathbf{r}}dz \left[V_r \frac{\vec{r}\cdot\vec{R}\cos\theta_0 + \vec{R}\cdot\vec{r}_\perp\sin\theta_0}{rR}\sin\psi + V_z\cos\psi \right]^2 .$$

A further expansion provides this convenient expression for the interaction potential noticing that terms linear in $\sin\xi$ do not contribute, we have:

$$\begin{aligned} W_{INT} = -\frac{1}{2}\epsilon_a \iiint d\vec{\mathbf{r}}dz \Bigg[& V_z^2\cos^2\psi + \frac{1}{2}V_r^2\sin^2\psi + V_rV_z[\sin 2\psi]\frac{\vec{r}\cdot R}{rR}\cos\theta_0 \\ & \frac{V_r^2\sin^2\psi}{r^2R^2}\left((\vec{r}\cdot\vec{R})^2 - (\vec{r}_\perp\cdot\vec{R})^2\right)\frac{\cos 2\theta_0}{2} \Bigg] \end{aligned} \tag{3.23}$$

It is worthwhile to split it in 3 contributions:

$$\begin{aligned} W_{INT} = &-\frac{1}{2}\epsilon_a \iiint d\vec{\mathbf{r}}dz \left[V_z^2 \cos^2\psi + \frac{1}{2} V_r^2 \sin^2\psi \right] \\ &-\frac{1}{2}\epsilon_a \iiint d\vec{\mathbf{r}}dz \left[V_r V_z [\sin 2\psi] \frac{\vec{r}\cdot\vec{R}}{rR} \right] \cos\theta_0 \\ &-\frac{1}{4}\epsilon_a \iiint d\vec{\mathbf{r}}dz \left[\frac{V_r^2 \sin^2\psi}{r^2R^2} \left((\vec{r}\cdot\vec{R})^2 - (\vec{r}_\perp\cdot\vec{R})^2 \right) \right] \cos 2\theta_0 \end{aligned} \tag{3.24}$$

The first term corresponds to a pure radial repulsive potential, the superposition integral is maximum when the defect and the pinning potential overlap. The two remaining terms are potentials dependent essentially on the transverse electric field and on the swirl of the defect and can be attractive or repulsive depending on θ_0 and the values the multiplying integrals.
Clearly the interaction potential cannot be computed in close form, but, with some assumptions we can derive an analytical approximation.

3.3.2.1 Small core approximation

Here we will assume that the core of the defect is small with respect to other length scale.

Moreover $V(\vec{r},z) = \frac{z}{L} V_s(r)$ and we can also assume that the the molecules are well oriented toward the $x-y$ plane, at least far from the defects core: only term depending on $\sin^2\psi$ are considered and $\psi(R,z)$ is set to constant $\psi_\infty(z)$, the far field profile.

Plugging everything in the equation 3.23, and neglecting the finite core size effect we have:

$$W_{INT} = \frac{1}{2}\alpha|\epsilon_a| L \cos 2\theta_0 \int d\vec{\mathbf{r}} \left[\frac{(\vec{r}\cdot\vec{R})^2 - (\vec{r}_\perp\cdot\vec{R})^2}{2r^2R^2} \left(\frac{dV_s}{dr} \right)^2 \right] \tag{3.25}$$

with $\alpha = \frac{1}{L}\int_0^L \left[\frac{z}{L} \sin\psi_\infty(z) \right]^2 dz$ taking into account the overlap integral in the z direction.

It can be shown that this integral can be written as

$$W_{INT} = \frac{\alpha}{2}|\epsilon_a| L \cos 2\theta_0 \int dr r_o \left(\frac{dV_s}{dr} \right)^2 G(r/r_o) \tag{3.26}$$

with

$$G(r) = \pi \begin{cases} 0 & , r \leq 1 \\ r - \dfrac{1}{r} & , r \geq 1 \end{cases} .$$

In the case of a voltage profile of the type $V_s(r) = V_0 + v \exp -\dfrac{r^2}{w^2}$ we a close form for the interaction energy, which is:

$$W_{INT} = \frac{\pi}{4} |\epsilon_a| \alpha L v^2 e^{-\frac{r_o^2}{2w^2}} \cos 2\theta_0$$

3.4 The liquid crystal light valve as platform for defect induction and control.

In the previous section we have shown theoretically that it is possible to induce in a controlled manner a single defect in the texture of the liquid crystal by using an appropriately shaped profile for the voltage applied across the nematic liquid crystal layer. Conventional cells, cells with uniformely coated glass plates, are therefore unfit to this task. We need, then, to engineer a new type of cell in which the profile of the voltage on the top of the LC layer can be tuned at will. One of the possible solutions is to use shaped electrodes [47], resistive electrodes as control layers [48, 49], or non uniform dielectric layers between the liquid crystals and the uniform control contact [50]. These techniques are well known for optical devices like tunable focus lenses, liquid crystal wavefront correctors for adaptive optics. Beside these methods, we might consider a liquid crystal light valve (LCLV) with hometropic conditions. The LCLV was first introduced by Margerum et al. [51] for image intensification and retention. The LCLV is composed of a photoconductive layer (figure 3.11), in our case made of a slab of bulk monocrystalline $Bi_{12}Si0_{20}$ (bismuth silicon oxide, BSO) with the outside surface coated with ITO, and a thin glass plate with ITO deposited on the inside surface. The two electrodes allow the application of a bias voltage across the cell. The inside surfaces of both the glass plate and the BSO are treated with lecithin in order to favor the homeotropic anchoring of the LC moelcules. The BSO slab and the glass plate are glued together, with thin spacers in between them which will define the LC layer thickness. The LCLV is finalized by filling it with the appropriate liquid crystal.

In this configuration, the BSO layer acts like a photo-controllable voltage divider that when illuminate can tune the effective voltage across the LC layer. By applying the appropriate illumination spatial profile we can modulate quite well this effective voltage, due to the high spatial sensitivity and the good modulation transfer function

of the LCLV [52]. The choice of the BSO as a photoconductive layer is justified by its availability in large samples and the good optical quality. Moreover, among the available photoconductors, the BSO exhibits the lowest dark current, which is important for the overall sensitivity of the device, and has a high saturation intensity [52, 53] which is important for the device linearity. For moderate frequency of the bias voltage, we are in quasi-static regime (we neglect phase shift effects) [54, 55] and the transferred voltage across the LC layer upon an illumination intensity $I(x, y)$ can be approximated by [52, 56]:

$$V_s(x, y) = \left| \frac{Z_{\text{BSO}}}{Z_{\text{BSO}} + Z_{\text{LC}}} \right| V_{\text{BIAS}} = \gamma V_{\text{BIAS}} + \alpha I(x, y) \ , \tag{3.27}$$

where α and γ are parameters depending on the operating point (frequency and bias voltage), the LC layer and the photoconductive layer parameters [52, 54]. The linearity of the transferred voltage versus the incident illumination [52], on one hand, the high spatial sensitivity on the other hand, allows us to use the simplest model for the LCLV behavior. Moreover the BSO has a high photoconductivity gain with a good optical transparency in the visible. This enable us to use fairly low optical densities, typically about 3mW/cm^2, and to design devices operating in transmissive mode, with the optional use of the writing beam for simultaneous readout. Although the BSO sensitivity to visible light beam, the absorption depends on the wavelength used; 532nm and below will be used for the writing process, and wavelength around 633nm and above will be use to probe the texture, as the sensitivity is reduced at this wavelength [57]. White light beam can be used too for the reading process, but must to be filtered before, in order to reduce biasing effects.

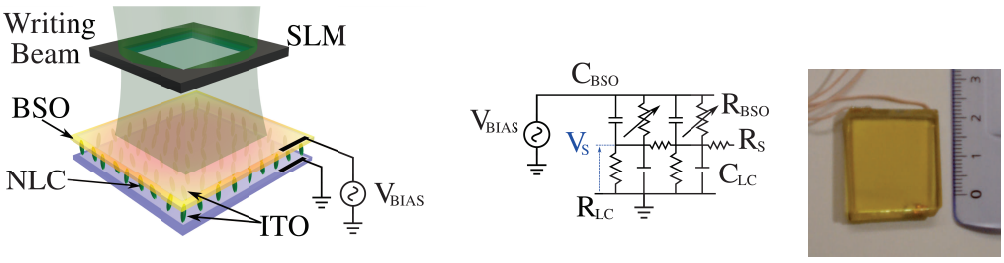

(a) (b)

Figure 3.11: Descriptive view of an homeotropic LCLV. The spatial light modulator (SLM) controls the transverse profile of the conditioned illumination beam. 1D equivalent circuit of an LCLV. Photo of an unclosed LCLV

The LCLV has proven itself to be more versatile with respect to other methodolo-

gies, as it allows us to reconfigure the topology of the induced electrodes by changing the electrode shape and position (profile of the illumination) and the effective voltage (intensity). Such versatility is supported by the use of LC spatial modulator (SLM), which enables real time and arbitrary control of the equivalent designed electrodes. The LCLV technology is a very mature one and had found many interesting applications since it introduction from display optics [51, 52], adaptive beam shaping [58, 59], fundamental physics [60], wave-mixing and singular wave-mixing [61, 62], all optical computing [63] and high precision metrology[64].

3.5 Experimental realization of localized defects

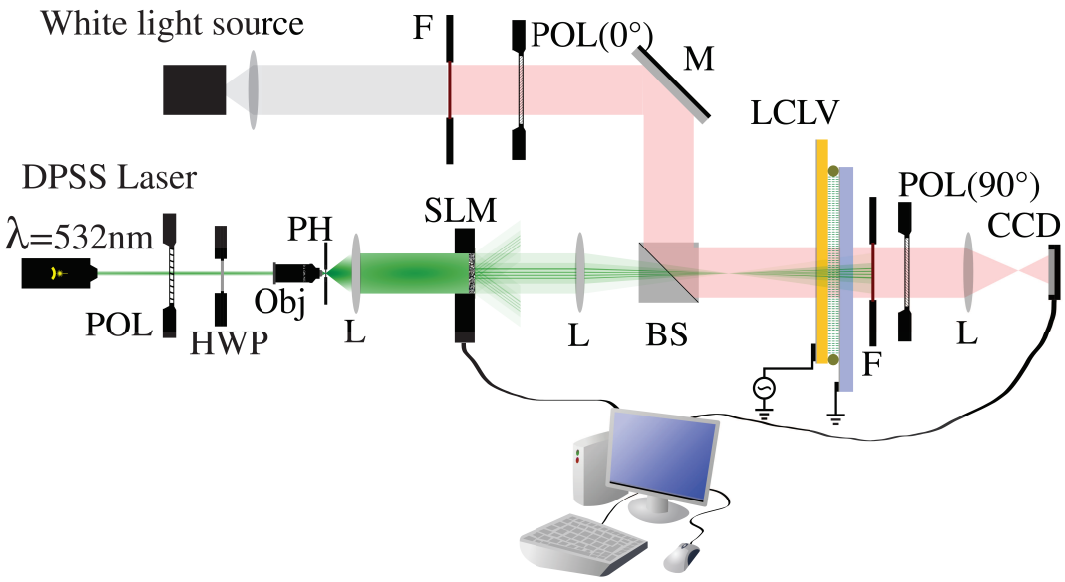

Figure 3.12: Experimental setup. HWP: half waveplate; M: mirror; PH: pinhole; Obj: objective; L: lens; F: red filter, POL: polarizzer;BS: beam splitter; SLM: spatial light modulator; CCD: CMOS camera; POL(0°), POL(90°), respectively, the input polarizer and the analyzer.

To implement the induction of defects, we use an LCLV (see figure 3.11(b)) filled the MLC-6608, with thickness $15\mu m$. The spatial light modulator (SLM) in the setup (figure 3.12) is used to impress the desired pattern on the light intensity via computer generated holograms. The red filter after the LCLV suppresses the residual intensity of the writing beam, $\lambda = 532$nm, with power density about 10mW/cm^2. The whole sample is illuminated with a white beam filtered with a red glass filter.

3.5.1 Single defect induction and control.

To induce a single defect in the texture of the liquid crystal, the SLM is programmed to send a small bright spot of the writing beam onto the sensitive side of the LCLV . The bias is turned on from 0V to higher voltage until the defect is formed. The umbilics are generated with different diameter of the incident spot (figure 3.13). We observe that the *threshold*, that is, the bias above which the transmitted intensity across the cell is not zero, varies with the size of the illumination spot.

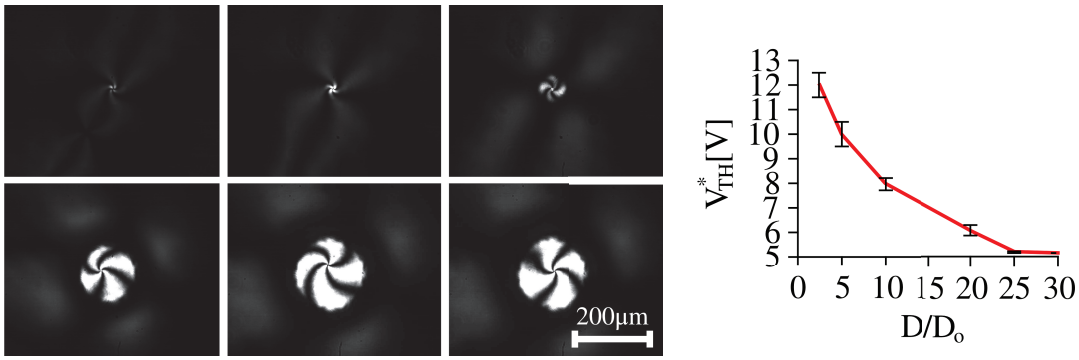

(a) (b)

Figure 3.13: (a) Induced umbilic with various spot sizes of the illuminating beam . (b) Threshold versus spot size, $D_o = 6.85\mu$m.

During the turn on, the slew rate of the voltage was limited in order to have the response time of the LCLV small with respect to the rise time, which avoids the formation of undesired umbilics. However, the undesired excited defects relaxed quickly and the only remaining defect spontaneously migrates to the center itself with respect to the writing spot. This is a clear evidence of the effect of the pinning potential on the defect. It is worthwhile to notice that different shapes of the illumination pattern generate a +1 defect located near the center of the spot.

3.5.1.1 Spatially resolved polarimetry

Until now the sign of the defects is identified by rotating the polarizer: the +1 defects rotate in the same direction of the polarizer and the -1 rotate oppositely. An another interesting technique to see the texture of the LC cell is based on the spatially resolved Stokes polarimetry [65, 66]. The spatially resolved Stokes polarimetry is an interesting technique to observe singularities in light fields and to retrieve the information carried in the phase of a beam. By sending a circularly polarized light beam on the cell, and by

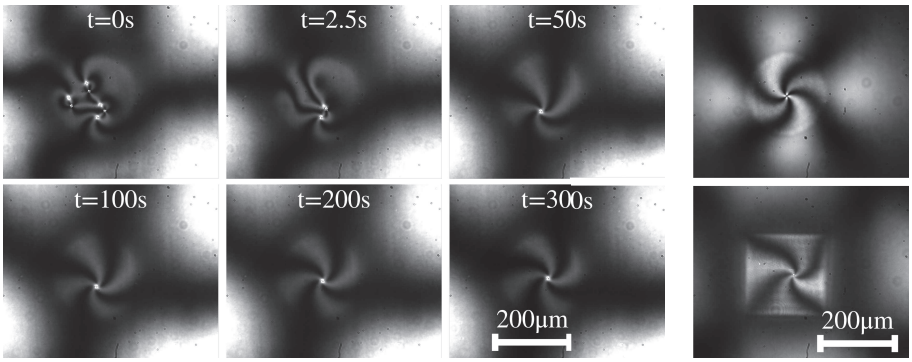

(a) (b)

Figure 3.14: (a) Early dynamics of the generation of the umbilics; multiple defects are generated at the beginning. (b) Generation of an umbilic with different shape of the illumination. The shape of the induced electrode can be seen in the background.

using the Jones matrix method, it is easy to find that the output beam will be a superposition of the unconverted part, and a converted part which carries information on the azimuthal distribution of the director in the thin sample of LC that we are investigating. Being $\vec{e}_\sigma = \frac{1}{\sqrt{2}}(\vec{x} + i\sigma\vec{y})$ the polarization of the white light with which the cell is illuminated, where $\sigma = +1/-1$ stands for left/right handed circular polarization, the output beam polarization is $\mathcal{M}\cdot\vec{e}_\sigma = \cos\frac{\Gamma}{2}\vec{e}_\sigma + i\sin\frac{\Gamma}{2}e^{2i\sigma\theta}\vec{e}_{-\sigma}$. By probing the output field with a linear polarizer forming an angle α with $\vec{x}$ (the x axis direction), the collected intensity on the CCD will be $I(\alpha) = \frac{I_0}{2}\left(\cos\frac{\Gamma}{2} - \sigma\sin\frac{\Gamma}{2}\sin\left[2(\theta-\alpha)\right]\right)$, where I_0 is the input beam intensity. We clearly see that: $\left[I(\frac{\pi}{2}) - I(0)\right] / \left[I(\frac{\pi}{2}) + I(0)\right] = \sigma\sin\Gamma\sin(2\theta)$, and $[I(\frac{\pi}{4}) - I(-\frac{\pi}{4})]/[I(\frac{\pi}{4}) + I(-\frac{\pi}{4})] = \sigma\sin\Gamma\cos(2\theta)$. The azimuthal variation can, then be recovered. The same applies to the polar component. Unlike in the previous cases, the azimuthal component cannot be calculated for crossed linear polarizers nor be uniquely determined in general. As $\theta + \pi$ and θ are equivalent, we cannot determine θ with an additive constant $\pi/2$ if we use $\sigma = -1$, right polarization, instead of left polarization, $\sigma = 1$. To probe the texture of the induced defect we perform the technique described above on the LCLV illuminated with a spot of diameter $\approx 130\mu m$ with the writing beam intensity about $300\mu\mathrm{W/cm}^2$. A quarter wave plate is inserted on the path of the white light beam, between the LCLV and the polarizer POL(0°) (see figure 3.12), and adjusted in order to have a circularly polarized incoherent light. Images were taken, varying the output polarizer angle from 0° to 135° with steps of 45°. The polarimetric images are shown in figure 3.15. We can observe that the azimuthal angle varies about

2π for counterclockwise turn around the defect core, which is resolved only within few μm due to experimental limitations: relative offset of the acquired images and the intrinsic scattering of the defect core. Indeed, the figure shows twice the azimuthal angle which varies about 4π. We can also notice that for increasing values of the bias the defect size increases For values of the applied voltage greater than 14V we can observe a substantial change in the polarimetric images due to the fact that the radial phase shift in the probe beam overcomes π. Indeed the induced umbilic like structure increases in size with the voltage, the molecules also bend toward the $x-y$, that is, the polar angle increases, with its peak value far from the center. Then the phase shift grows radially with the distance (until the first peak) with respect to the core, thus inducing radial phase modulation in the polarimetric images.

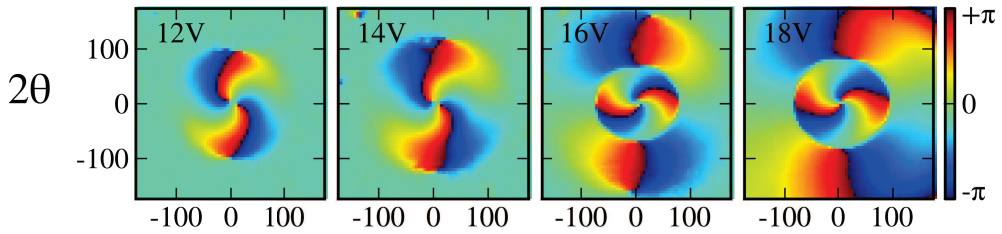

Figure 3.15: Spatially resolved polarimetry of the induced defect for different values of the applied voltage: (from left to right) 12V, 14V, 16V and 18V.

3.5.1.2 Experiment on the pinning of the defect.

To emphasize the presence of the pinning potential induced by the radially symmetric illumination, first, a gas of defect is generated in the LCLV by applying a bias of 30V. During the relaxation dynamics, a +1 moving umbilic is targeted by the writing beam of diameter about 205.4μm, with intensity 3mW/cm^2. Due to the bell shaped profile of the voltage induced by the writing beam across the cell, a pinning potential is created. We observe first a distortion of the defect (first three panels of figure 3.16). Then, the pinning force recalls the defect towards the center of the beam in order to minimize the overall energy.

This mechanism provides a natural stabilization of the generated umbilic, and is important for the generation of robust and more complex structures of umblics. For certain ranges of parameters, the pinning force will equate the long range $1/r$ force generated by the neighboring umbilics. All the defects can be consequently locked individually at the desired position by choosing the appropriate illumination pattern.

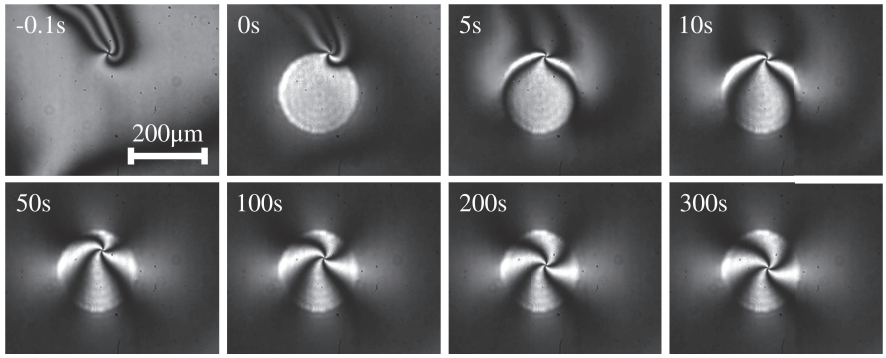

Figure 3.16: Snapshots of the defect dynamics under a pinning potential applied at t=0. The umbilic is attracted by the induced potential and stabilizes itself near the center of the writing beam.

3.5.1.3 Correction to the logarithmic law

With the technique described in the previous section, we were finally able to study the interaction of defects in a deterministic way and to recover features hidden by the defects statics. As illustrated in figure 3.17, three vortices are induced when creating willingly the two lateral ones with index +1. The bias voltage across the LCLV is kept slightly below V_{FT} and the writing beam consists of two circular spots of diameter about 200μm with intensity 4mW/cm^2. A third defect with index -1 appears in between them, due to the required reconnection of the distorted field lines of the nematic distribution. When one of the disc constraints is released (figure 3.17(a)), the negative and the positive vortices are free to interact (figure 3.17(c)(e)) and annihilate (figure 3.17(f)). Their separation distance r=r(t) versus time is plotted in figure 3.17(g) and compared with their separation in the absence of external potential. In order to emphasize the deviation from the power law behavior, the data for both constrained and unconstrained dynamics were normalized to the collision time for the unperturbed vortex pair. The deviation from the $r_0\sqrt{1-t/t_{COL}}$ law is significant, as the presence of the third defect slows down the interaction considerably by introducing screening effects. We have also studied vortex-pair interactions, in the presence of a static defect. The measurements demonstrate the importance of the propagation of the vortex phase, as the latter introduces a weakly nonlinear mobility in the dynamics of the surrounding defects, with the mobility defined as $-r(t)v(t)$, v the relative velocity, and equal to $r_0^2/2t_{COL}$ for the square root law, constant and related to the effective viscosity and the elastic constants of the liquid crystal. The theoretical prediction for a logarithmic dependence of the mobility [37] on the vortex speed results in good agreement with

the data (see figure 3.18), thus reconciling the theory with the experimental observations. The presence of a third vortex substantially lowers the vortex-pair interaction speed. Besides their fundamental relevance, the findings also pinpoint the accuracy of the optical addressing and pave the way for further developments on the management of umbilics in liquid crystals.

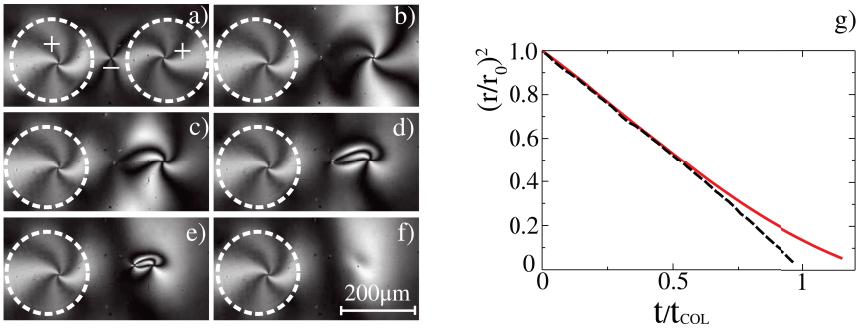

Figure 3.17: Controlled collision of two umbilics. Three umbilics are created, two with index +1 and the central one with index -1 by frustration. The release of the left defect triggers the collision dynamics (a-f). An important deviation from the square root law is observed (g).

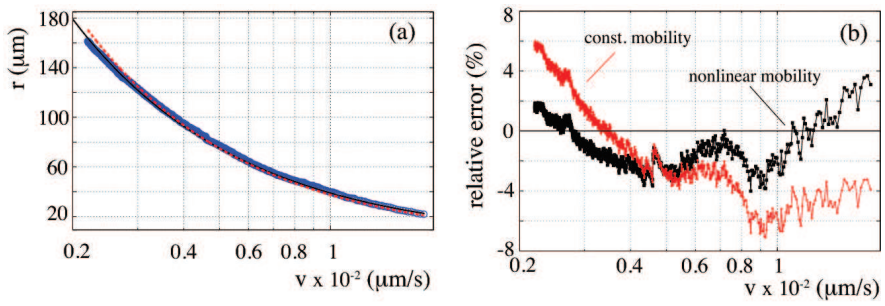

Figure 3.18: (a) Defect separation versus their relative speed in logarithmic scale. Blue circle the experimental data, the error is within their respective radius. Dashed red line: best fit with constant mobility $-rv = m_0$ with $m_0 = 0.3744\mu m^2/s$. The solid black line, the best fit for the nonlinear mobility model: $-rv = m_1/\log(v/v_0)$, $m_1 = 7.23543\mu m^2/s$, $v_0 = 119089\mu m/s$. (b) Relative error for the two models.

3.5.2 Defect arrays

After having implemented the building blocks for the the management of a single defect in the LCLV, we can proceed to the next level, where the management of large

collections of defects can be achieved. To generate an array of defects, the SLM is programmed to send the appropriate matrix of spots on the sensitive side of the LCLV. The spots are well separated so that the induced voltage across the cell has well defined peaks. Moreover the background of the illumination spot is reduced in order to prevent the umbilic like structure to be generated to spread across the cell. The bias voltage is calibrated so that the overall voltage on the cell due the dark state of the SLM (when the spots are turned off) and the probe beam, is well below the Fredericks transition voltage. This prevent unwanted defect to form. In figure 3.19 we show for different applied bias the texture of the liquid crystal when the LCLV is illuminated with an hexagonal pattern of bright spots with intensity about $300\mu W/cm^2$.

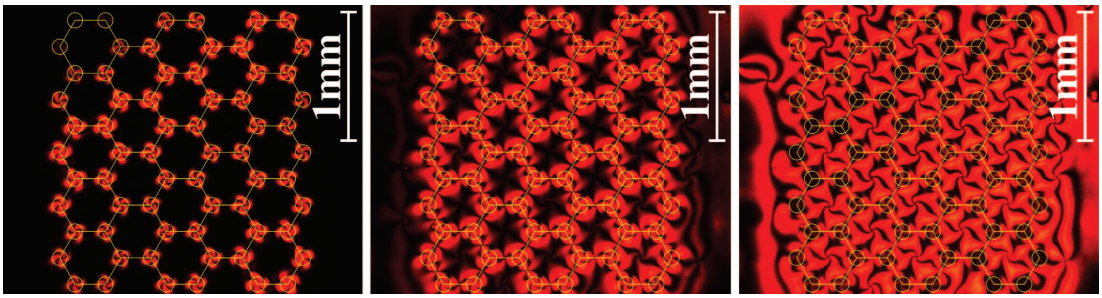

Figure 3.19: Texture of an hexagonal array under linear crossed polarizers. The circled areas represent in scale the writing beam spots. The figures correspond to (from left to right) to 15V, 20V, 25V applied voltage.

For low voltage, distinct umbilics can be observed. When the bias voltage increases, the background voltage increases as well. This make the generated umbilics to spread and finally touch.
The liquid crystal medium is a continuous director filed, in other to accommodate the far field induced by two umbilics with index +1 (located at the vertices of the hexagons), a third defect is created in between them by frustration, this helps to reduce the energy of the induced structure. Further increase in the voltage will make the -1 umbilics to connect and create +1 umbilic in the center of hexagon. To support the explanation we perform a spatially resolved polarimetry on an honeycomb lattice of umbilics 3.20. It appears clearly from the polarimetric images that, the +1 defect are well isolated on the smooth background for low voltages (12V). The phase increase about -2π when circling around the point at which they connect. For the defects created at the center of the hexagons, a counterclockwise turn around them shows a change of $+2\pi$, revealing the presence of a +1 umbilic.

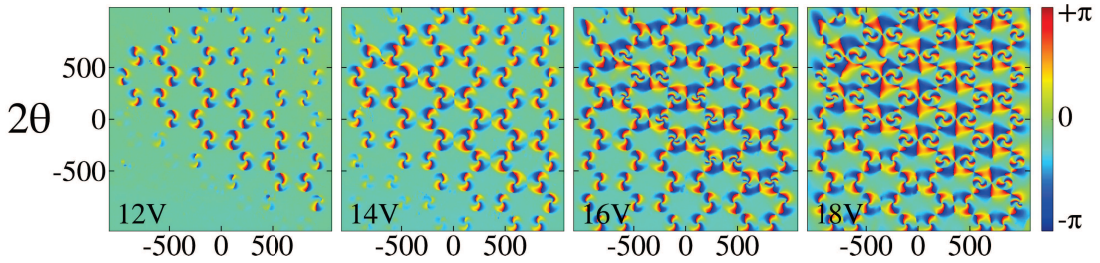

Figure 3.20: Spatially resolved polarimetry images of the hexagonal array of defects for increasing values of the applied voltage. The polarimetric images are shown (from left to right) for 12V, 14V, 16V and 18V.

3.6 Conclusions

In this chapter we show that singularities can generated willingly in crystal cell with hometropic anchoring, filled with negative anisotropic material. But these singularities, due their dissipative nature tend to be collectively unstable. The generated defects come in random number and random positions, with those of the same sign repelling each other and those of opposite sign attracting each other and annihilate. It is evident that such architecture is unreliable for applications; at least for those requiring the repeatability of the texture with respect to their number, position and eventually to their charge. We demonstrated theoretically that it is possible to achieve this goal by using spatially non uniform bias. The later concept is successfully implemented for the first time using liquid crystal light valves, enabling defects for photonic applications.

Chapter 4

Optical Vortices

It is well known that light can exert mechanical effects on matter. This is not limited on the effect of the radiation linear momentum, which can set particle to translation. Rotation of particle can happen if the radiation is circularly polarized. In this case the electromagnetic wave couples it spin angular momentum with that of the medium it interact with, and this effect is physically observable by the spinning of the particles around themselves or the object around itself, with the sense and rate of rotation depending on the helicity of the light beam. The first experimental observation of the fact that light can possess an intrinsic angular momentum is to due to R. A. Beth [67]. A polarized beam is sent onto a birefringent plate free to rotate. The thickness of the plate is that of a half wave plate at the operating wavelength and transforms a left circular polarized light beam in a right circular polarized beam. The plate experiences torque that changes its sign with the input polarization. By measuring the amount of torque, the value of the angular momentum of the photon can be calculated knowing the intensity the incoming light. The result was $+\hbar$ for left hand polarized input an $-\hbar$ for right hand one. For intermediate values it was shown that torque diminishes and vanishes for linearly polarized beams.

Besides these effects, it was also observed that, linearly polarized beams like Laguerre-Gauss beams, can also set particles in rotation and that they rotate around the axis of the beam and not the around their own axis as for circular polarized beam [68, 69]. This is related to the so called orbital angular momentum of the beam and is entangled to the beam structure: the phase.

Beams carrying orbital angular momentum are characterized by phase dislocations in their wave front. The latest manifest themselves by the nulling of the intensity at the position of the dislocation with the energy flowing around the singularities, fact

after which they are called optical vortices. Optical vortices are interesting not only for the mechanical effects they can have on matter, where they are mainly used for implementing optical tweezers [70, 71, 72, 73], they are also used in the field of high precision micro-machining [74, 75, 76], astronomical imaging (properly, the devices to generate them) as coronagraph [77, 78, 79]. Their latest employment can be find in the field of quantum communication where, the orbital degree of freedom of optical vortices is used to generate high dimensional q-bits [80, 81, 82, 83].

In this chapter we will introduce first the angular momentum of light beams, restricting ourselves to main results and to the case of paraxial propagation. The methods used in the generation of optical vortices will be discussed with a particular emphasis on the use of liquid crystal devices containing dislocations as they can convert the spin angular momentum of light beams into the orbital angular momentum, thus generating optical vortices.

4.1 Angular Momentum of light beams

From classical electromagnetism a propagating electromagnetic field carries a liner momentum depending on the Poynting vector and is defined as:

$$\mathbf{P} = \epsilon_0 \int \mathbf{E} \times \mathbf{B} \mathrm{d}^3\mathbf{r},$$

which, after quantization, leads to a well defined momentum for $\mathbf{p} = \hbar\mathbf{k}$ for a photon [84, 85]. With the same procedure, when balancing the angular momentum of particles in light field with respect to a pole $\mathbf{r}_o$, the angular momentum of the electromagnetic field can be introduced as:

$$\mathbf{J}(\mathbf{r}_o) = \epsilon_0 \int (\mathbf{r} - \mathbf{r}_o) \times (\mathbf{E} \times \mathbf{B}) \mathrm{d}^3\mathbf{r}.$$

If we use the tranversality condition for the magnetic field $\mathbf{B}$, the angular momentum can be rewritten with respect to the potential vector $\mathbf{A}$, and it is demonstrated that it is the sum of two contribution i.e.

$$\mathbf{J}(\mathbf{r}_o) = \mathbf{J}_o(\mathbf{r}_o) + \mathbf{J}_s,$$

with

$$\mathbf{J}_s = \epsilon_0 \int \mathbf{E} \times \mathbf{A} \mathrm{d}^3\mathbf{r},$$

and

$$\mathbf{J}_o(\mathbf{r}_o) = \epsilon_0 \sum_{i=x,y,z} \int E_i[(\mathbf{r}-\mathbf{r}_o)\times\nabla]A_i \mathrm{d}^3\mathbf{r}.$$

$\mathbf{J}_s$ is independent of the position of the pole $\mathbf{r}_o$, which will be later set to the origin. It is then the *intrinsic* part of the angular momentum and is termed as *spin angular momentum* (SAM) and depends on the vectorial nature of the propagating beam. Indeed, a scalar field, with linear polarization has a zero spin angular momentum as $\mathbf{E}$ and $\mathbf{A}$ are always parallel. Moreover, by quantizing the spin part, the angular momentum of photon is given by [84]: $\sigma\hbar\mathbf{k}/|\mathbf{k}|$, where σ represent its *helicity*; with $\sigma = +1/-1$ for left circular/right circular polarized photon.
The second contribution of the angular momentum $\mathbf{J}_o$ depends explicitly on the chosen reference/pole, and can be decomposed in the following manner:

$$\mathbf{J}_o(\mathbf{r}_o) = \mathbf{J}_o(0) + \mathbf{r}_o \times \mathbf{P}.$$

It represents the *extrinsic* part of the angular momentum of light: *the orbital angular momentum*, and will be shown to be dependent essentially on the phase structure of the beam i.e. its vorticity.

For a monochromatic beam pulsating at ω, we can express OAM and the SAM with respect to the electric field complex amplitude E:

$$\mathbf{J}_s = \frac{\epsilon_0}{4i\omega}\int E^* \times E \mathrm{d}^3\mathbf{r} + c.c.$$

$$\mathbf{J}_o(\mathbf{r}_o) = \frac{\epsilon_0}{4i\omega}\sum_{i=x,y,z}\int E_i^*[(\mathbf{r}-\mathbf{r}_o)\times\nabla]E_i \mathrm{d}^3\mathbf{r} + c.c$$

Even at this stage, the expressions of the angular momentum are difficult to handle, they are not explicit quantities that can be related to simple characteristics of the electromagnetic beam. As we deal with propagating beam with small divergence, we will limit ourselves to paraxial propagating beams, along z for simplicity. For paraxial beams the longitudinal component can be neglected; the electric field is nearly transverse. The main contribution of the angular momentum of optical field lies then along z and depends only on the transverse component of the field. Using this assumption, and writing the transverse component with respect to the circular polarization basis in the transverse plane, we finally have with respect to the pole $\mathbf{r}_o$ on the beam axis:

$$J_{sz} = \frac{\epsilon_0}{2\omega}\int \left(|E_L|^2 - |E_R|^2\right)\mathrm{d}^3\mathbf{r},$$

$$J_{oz} = \frac{\epsilon_0}{2i\omega} \int \left(E_L^* \partial_\xi E_L + E_R^* \partial_\xi E_R\right) \mathrm{d}^3\mathbf{r}.$$

Note that the linear momentum lies along z, then, the orbital angular momentum is independent on the position of the pole if the later is taken on the beam axis.

Its is worthy to write the latest expressions considering them explicitly with respect to the number of photon carried by the radiation. The number of photon is given by

$$\mathcal{N} = \frac{1}{\omega\hbar} \frac{\epsilon_0}{2} \int E^* \cdot E \mathrm{d}^3\mathbf{r}.$$

Dividing the angular momentums by the number of photon we have:

$$J_{oz}/\mathcal{N} = \hbar \int -i \left(E_L^* \partial_\xi E_L + E_R^* \partial_\xi E_R\right) \mathrm{d}^3\mathbf{r} / \int \left(|E_L|^2 + |E_R|^2\right) \mathrm{d}^3\mathbf{r},$$

$$J_{sz}/\mathcal{N} = \hbar \int \left(|E_L|^2 - |E_R|^2\right) \mathrm{d}^3\mathbf{r} / \int \left(|E_L|^2 + |E_R|^2\right) \mathrm{d}^3\mathbf{r}.$$

Here, we have the expression of the average angular momentum carried by a single photon. The spin part depends only on the helicity of the beam, a left polarized beam $E_R = 0$, will caries $+\hbar$ SAM per photon, and $-\hbar$ if right circularly polarized, $E_L = 0$. The orbital part have the same expression if written with respect to the horizontal (x) and the vertical (y) polarization, hence, independent on the state of polarization of the beam. We can see an explicit dependence on the derivative respect to the azimuthal coordinate: the orbital angular momentum depends on the azimuthal structure of the beam. Indeed, by taking a beam with the simplest azimuthal dependance, a beam with helical phase, i.e. $a(r)e^{im\xi}$, regardless to its polarization and radial profile, the orbital angular momentum per photon is $m\hbar$.

4.2 Optical vortices and their generation.

Optical vortices are characterized by the presence of single or multiple phase dislocation where the field amplitude goes to zero and quantities like polarization and phase are undefined. At this singular point the phase front of the electromagnetic field has an helical structure with number of helix and rotation direction depending on the topological charge defined as

$$m = \frac{1}{2\pi} \oint_C \nabla\chi \mathrm{d}\mathbf{l},$$

C any closed curve encircling only the considered singularity, χ the phase of the considered complex amplitude. In the framework of paraxial beam propagating along z, the

simplest optical vortex that we can then imagine has the form of: $A(r,z)e^{i(kz+m\xi+\chi(r,z))}\mathbf{e}_\sigma$ and carries $m\hbar$ OAM per photon and $\sigma\hbar$ SAM per photon, σ the helicity.
From what we had discussed until now, the vorticity of the optical field depends only on the phase structure of its amplitude. However, the OAM and the SAM conserve separately if the propagating medium is the vacuum, thus, these two parameters can be coupled efficiently or uncoupled by choosing the appropriate medium. In this section will discuss methods used to generate optical vortices from non singular beams by acting only on the wavefront (then only on the OAM). The second part will be dedicated to the generation of singular beams based on the SAM and the OAM coupling.

4.2.1 Astigmatic mode converters

Optical vortices can be generated by using cylindrical lenses [86]. The main concept of this mode converter has its background on the completeness of the Hermite-Gauss (HG) basis and Laguerre-Gauss (LG) basis with the linear relationship between the projection coefficients from the LG and a $\pi/4$-rotated HG basis to the HG basis. Beijersbergen et al demonstrated that [87] a $\pi/4$-rotated $\mathrm{HG}_{m,n}$ and $\mathrm{LG}_{m,n}$ can be written as a linear superposition of the same set of vectors $\{\mathrm{HG}_{m+n-l,l}\}_{l=0,\ldots,n+m}$. The expansion coefficients are in phase for the HG mode and are the same for LG mode except for the $(i)^l$ multiplying every coefficient. By using an astigmatic lens and the effect it has on the Gouy phase of each mode, it is possible to change coherently the relative phase between each coefficients. This relative phase shift depends on the distance between the two lenses. When this distance is set to $f/\sqrt{2}$, f the focal length of the cylindrical lenses, the phase shift is $\pi/2$ and every $\mathrm{HG}_{m,n}$ is converted to a $\mathrm{LG}_{m,n}$ vice versa [88]. This method can be highly efficient, but due to the hard condition on the type of input beam, which has to be an Hermite-Gauss beam, there is a severe limitation on using it.

4.2.2 Phase Plate

A plane wavefront can be transformed into a phase front with a screw dislocation by using elementary concepts of classical optics. This is achieved with thin glass plates that have a spatially varying optical thickness in term of λ equal to the desired wavefront over 2π. For instance the screw phase dislocation can be introduce in a propagating light beam by using glass plates with thickness depending linearly on the azimuthal coordinate [89] i.e $t(r,\xi) = t\xi/2\pi$, with t the height of the created spiral surface, thus,

the name of spiral phase plate. The introduced phase shift is given by:

$$\delta\phi(r,\xi) = dn\frac{t}{\lambda}\xi,$$

with dn the difference of the refractive index between the plate and the outer medium (glass, air), λ the operating wavelength. To see how the angular momentum is transferred to input beam, we can consider the effect of the spiral phase plate (SSP) on a beam impinging on it at a position r from its center. The normal to the surface at this point is given by $\vec{n} = s\sin\xi\vec{x} - s\cos\xi\vec{y} + r\vec{z}$, $s = t/2\pi$. Therefore, an incoming photon pictured as a ray normal to the bottom surface with linear momentum $\hbar k_1\vec{z}$, will exit at an angle β with respect to z, β given by $n_{air}\sin(\alpha+\beta) = n_{glass}\sin\alpha$; the Snell law is used and α represent the angle of the surface normal with respect to z, $\tan\alpha = s/r$. Note that the plane of refraction is oriented radially, so that the output momentum will have a z component and an azimuthal component with a null radial component and is given by $\hbar k_2(\vec{\xi}\sin\beta + \vec{z}\cos\beta)$, we remind that the angular momentum is given by $\mathbf{r}\times\mathbf{p}$. The z component of the orbital angular momentum with respect to the center of the plate is $L_z = r\hbar k_2\sin\beta$. For small bending angle α i.e. far from the center of the SSP, we can approximate $\tan\alpha \approx \alpha$, $\sin\alpha \approx \alpha$ and $\sin(\alpha+\beta) \approx \alpha+\beta$. Within these approximations, the angular momentum transferred to the photon is simply: $dn\frac{t}{\lambda}$. To

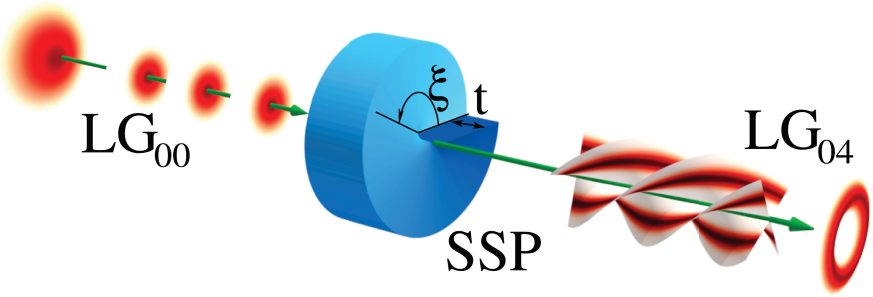

Figure 4.1: Sketch of a spiral phase plate with an incident LG_{00} beam, generating an optical vortex with topological charge 4.

generate an optical vortex with topological charge m the height of the SSP has to be set to $m\lambda/dn$. The latter condition can have drawback on the purity of the generated optical vortex in term of the azimuthal number [90] due to practical mismatch. However this offers some interesting insight for the generation of non integer optical vortices.

4.2.3 Diffraction gratings with embedded singularities

Beside the use of SSP, one of the most widespread method for the generation of optical vortices is based on holographic methods. The desired wavefront that we want to reproduce, $E_s e^{i(k_z z + m\xi)}$, is made to interfere with a reference beam (ideally a plane wave) $E_r e^{i(k_z z + k_x x)}$. The obtained interference pattern

$$I = |E_r|^2 + |E_s|^2 + \mathrm{Re}(E_r E_s^*)\cos(k_x x + m\xi) + \mathrm{Im}(E_s E_r^*)\sin(k_x x + m\xi),$$

, can, then, be recorded on a photographic plate. After being developed, the recorded hologram is used to generate the desired beam by sending in a plane wave and by filtering the first order diffracted mode. The availability of high quality spatial light modulators (SLM) make this alternative more versatile. The hologram can be generated by computer and sent to the SLM which will modulate the amplitude/phase of the input in order to diffract/transmit light accordingly. A generic transmittance function can be written as

$$T(x, y) = \sum_n T_n e^{in(2\pi \frac{x}{\Lambda} - m\xi)},$$

where Λ represents the periodicity of the grating, m the topological charge. Light is diffracted according to Bragg law (conservation of transverse momentum) and the m-th diffracted beam caries topological charge nm with an diffraction efficiency $|T_n|^2$. The generation of optical vortices with computer generated hologram can suffer efficiency problems, however high efficiency hologram can be generated with the use phase-only SLM with the appropriate transmittance function.
By using a blazed phase-only grating with 2π modulation depth, $T = \exp[i\mathrm{Mod}(2\pi \frac{x}{\Lambda} + m\xi, 2\pi)]$, a high efficiency close to the theoretical 100% can be obtained.

4.2.4 Panchanratnam-Berry phase optical elements.

Another method, in our opinion the most intriguing one, used to generate optical vortices is based on the so-called Panchnaratnam-Berry phase optical elements (PBOEs). The PBOEs are based on the use of the spatial manipulation of the polarization of electromagnetic wave in order to modify the wavefront, thus, couple the spin angular momentum and the orbital one. It is well known that when the polarization of a beam evolves adiabatically on a close path on the Poincaré sphere (equivalently the Stokes sphere), the polarization after every turn accumulates phase shift equal to half the corresponding solid angle sustained by the close path.

This can be achieve by using a medium that exhibits anisotropy, so that the SAM

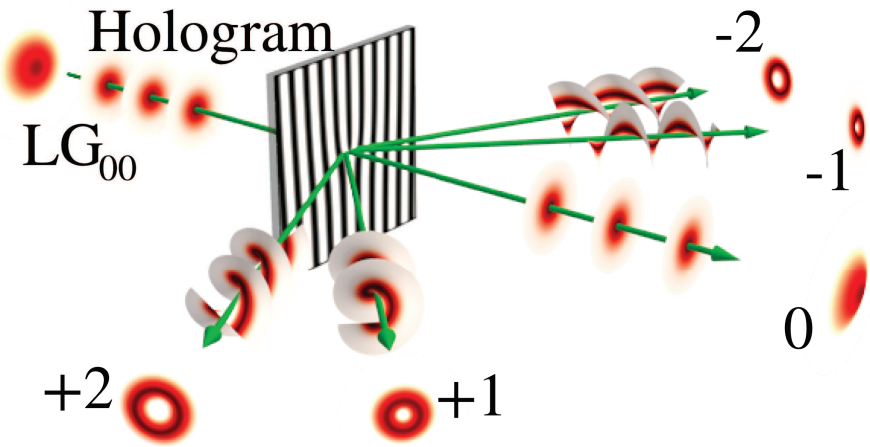

Figure 4.2: Diffraction of a LG_{00} mode by a forked hologram with singularity +1. The diffraction order depends on the grating profile, which can be optimized to enhance the desired diffraction order. In general the diffracted orders do not correspond to Laguerre-Gauss beams.

can be coupled efficiently with the OAM. Two different solutions came with few years of delay, one based on subwavelength grating [91], the other based on nematic liquid crystal [92]. Both are based on plate with constant thickness with non uniform planar variation of the optical axis for the LC based device : q-plate, and the axis of the wavelength microgroove forming the subwavelength grating. They can be considered as wave plate with constant local retardation and continuously space varying fast axis, thus the phase shift (between an ordinary and extraordinary) beam will be constant, but the polarization at the output will vary according to the relative orientation of the input polarization and the fast axis.

4.2.4.1 SAM and OAM coupling.

To get some insight on how these devices work, we can use the simplest approach based on the Jones calculus. We denote $\hat{\tau} = \cos\theta\hat{x} + \sin\theta\hat{y}$ the fast axis, and $\hat{\theta} = -\sin\theta\hat{x} + \cos\theta\hat{y}$, θ denotes the angle between the fast axis and the x. The input beam is taken to be propagating along the z, and diffraction is neglected. The Jones matrix can be written as: $\mathcal{M} = t_{\parallel}\hat{\tau}\hat{\tau} + t_{\perp}\hat{\theta}\hat{\theta}$, $t_{\parallel}$ and $t_{\perp}$ the complex transmission function for a beam polarized along the fast axis and the slow axis. The Jones vector can be rewritten as

$$\mathcal{M} = \frac{t_{\parallel} + t_{\perp}}{2}\mathbb{1} + \frac{t_{\parallel} - t_{\perp}}{2}[\hat{\tau}\hat{\tau} - \hat{\theta}\hat{\theta}],$$

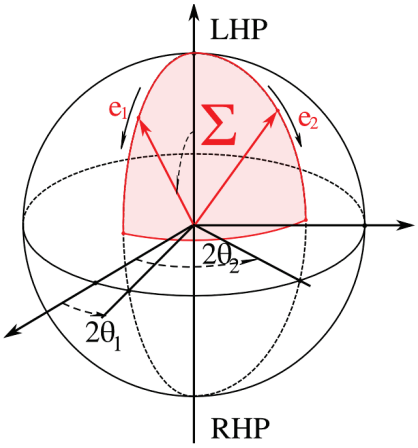

Figure 4.3: Evolution of a circular polarization on the Poincaré sphere. The movement on meridians corresponds to the effect of a wave plate with fast axis oriented along $\theta_{1,2}$, with increasing phase shift. The movement on the parallels corresponds to the effect of a polarization rotator.The phase shift between the two polarization state corresponds to the phase difference when one of them is rotated to match the other. The total phase shift is half the solid angle Σ.

showing that its explicit dependence on the transmission anisotropy and the fast axis orientation in the plane (last term). Since we are considering the spin angular momentum as a key parameter to work with, it is worthwhile writing the Jones matrix in the circular polarization basis

$$\mathcal{M} = \frac{t_{\parallel} + t_{\perp}}{2}\mathbb{1} + \frac{t_{\parallel} - t_{\perp}}{2}\left[e^{i2\theta}\mathbf{e}_{+}\mathbf{e}_{+}^{*} + e^{-i2\theta}\mathbf{e}_{-}\mathbf{e}_{-}^{*}\right],$$

with $\mathbf{e}_{\sigma} = \frac{1}{\sqrt{2}}[\vec{x} + i\sigma\vec{y}]$,$\sigma = +1/-1$ representing the left/right handed polarization LHP/RHP, we write shortly $\mathbf{e}_{+1} = \mathbf{e}_{+}$ and $\mathbf{e}_{-1} = \mathbf{e}_{-}$. It appears clearly that for circularly polarized input beam $\mathbf{e}_{\sigma}$, the beam that emerges from the PBOE device consists of two components: an unconverted component and a component with the opposite polarization with a phase shift $e^{2i\sigma\theta}$ which is entangled to the spatial arrangement of the optical axis, and independent on the optical path seen by the beam: a geometrical phase. Indeed by applying the Jones matrix to $\mathbf{e}_{\sigma}$, we get:

$$\mathcal{M} \cdot \mathbf{e}_{\sigma} = \frac{t_{\parallel} + t_{\perp}}{2}\mathbf{e}_{\sigma} + \frac{t_{\parallel} - t_{\perp}}{2}e^{2i\sigma\theta}\mathbf{e}_{-\sigma},$$

To introduce a singularity or a topological charge in the emerging beam we need to embed a topological defect in director field of the optical axis. The topological charge of

the emerging optical vortex is $m = 2\sigma q$ with $q = \frac{1}{2\pi}\oint_{\mathcal{C}} d\theta = m$, the topological charge of the defect in the director field formed by the optical axis, $\mathcal{C}$ any closed curve around the topological defect. The simplest pattern are the form $\theta(r,\xi) = q\xi + \theta_o(r)$ and have been successfully implemented with the wavelength grating and with liquid crystal cell with azimuthal anchoring like for q-plates. One of the interest in using liquid crystals is the low optical absorption and the relative and the relative easiness to process them. So, for the q-plate, $t_{\parallel} = e^{i2\pi L n_e/\lambda}$, $t_{\perp} = e^{i2\pi L n_o/\lambda}$, and the SAM-OAM coupling reads as:

$$\mathcal{M}\cdot\mathbf{e}_\sigma = \cos\frac{\Gamma}{2}\mathbf{e}_\sigma + ie^{2i\sigma q\xi}\sin\frac{\Gamma}{2}e^{2i\sigma\theta_0}\mathbf{e}_{-\sigma},$$

with $\Gamma = 2\pi(n_e - n_o)\frac{L}{\lambda}$ the phase shift of the equivalent wave plate. Note that the obtained expression explains the appearance of the helical phase but does not explain correctly the nulling of the intensity of the converted (optical vortex) beam on its axis. This due to the fact that the Jones matrix method does not consider diffraction, nevertheless the full Maxwell equation in the paraxial approximation gives the correct propagators that are identically null of the z axis [93]. The PBOE, for a circularly polarized input, couples its spin angular momentum to its orbital one with a coupling efficiency $\sin^2\frac{\Gamma}{2}$ depending on a phase shift equal that of the equivalent uniform wave plate. This phase shift depends on the optical parameter of the LC used and the thickness of the cell and is at its optimum when the equivalent wave-plate is a half-wave plate i.e. $\Gamma = \frac{\pi}{2} + l\pi$, l integer, the order of the wave plate. Clearly, due to process uncertainty, the device has to be tuned after fabrication in order to work at the optimum of the efficiency. With the help of the properties of LCs, q-plate can be tuned thermally [94] as the change in the order parameter reflects in a change of the optical anisotropy [3]. Electrical tuning can be used as well, by applying electrodes to the bounding glass plate [95]. For the thermal tuning, the order parameter changes, the nematic director none. For the electrical tuning the bias applied to the cell , will vary the azimuthal reorientation angle ψ of the LC molecules across the cell. The phase shift will be given by $\Gamma = 2\pi(\bar{n}_e - n_o)\frac{L}{\lambda}$, $\bar{n}_e = \frac{1}{L}\int_0^L n_e(\psi(z))dz$ being the effective index. Due the high optical anisotropy, the SAM-OAM couplers can be very thin while maintaining a deep modulation of the output efficiency, that is the efficient can be tune at will from 0 to values close to 1, making them SAM-OAM modulators.

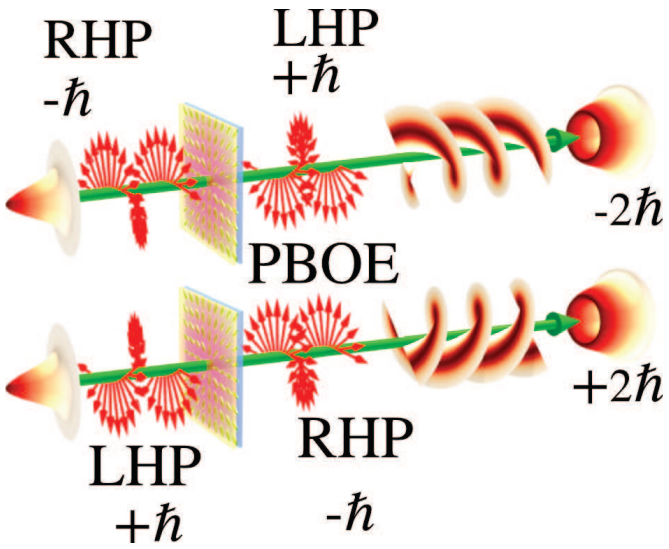

Figure 4.4: Schematics of the SAM and OAM coupling in a PBOE with topological charge +1. We assume that the phase-shift is π and unitary transmittance along fast and slow axes.

4.2.4.2 SAM and OAM conservation.

The PBOE has the essential effect to couple the SAM and OAM degree of freedom. In the ideal case $\Gamma = \pi/2$ a $\sigma\hbar$ photon entering the device will be converted into to a photon carrying $-\sigma\hbar$ of SAM and with an increment of $2q\sigma\hbar$ in the OAM, thus, with total AM $\sigma(2q-1)\hbar$. The net change in the total angular momentum is that transferred to the plate: $\Delta L_z = 2\sigma(1-q)\hbar$. It is clear that the AM of the photon is not always conserved, and the conservation of the OAM relies to the particular case of $q = 1$. For $q = 1$ device we have the pure SAM to OAM conversion, in the other cases we have SAM to OAM coupling. For non unitary efficiency it can be shown that $\Delta L_z = 2\sigma\hbar(1-q)\sin^2\frac{\Gamma}{2}$, here again the total AM of the photon is not conserved, and the conservation happens when the topological charge of the PBOE is 1.

4.2.4.3 Umbilical defects

To generate the optical vortex with the PBOE, it was essentially required that the director profile varies azimuthally in the plane transverse to the propagating beam. Hence the planar azimuthal rubbing of the nematic cell is adopted to create a q-plate [96]. It appears clearly that a surface defect will form in the bounding plate correspondingly to the location of the center of the azimuthal rubbing. These surface defects, *boojums*, connect in the bulk to form the so-called *schlieren* defect that looks under crossed po-

larizers like an umbilic. So, the main requirement is to replicate this texture view from a transverse plane. As we saw in the previous chapter, umbilic defects exhibit the same azimuthal distribution of the director projection in the $x-y$ plane. The first successful demonstration of using them as SAM to OAM converter (q=1) was done by Brasselet et al [97], with a demonstration of the switching by modulating the bias voltage under and above the the Fredericks transition voltage. As we saw in the previous chapter, the generated umbilics have charge +1/-1. But in normal cell, +1 defect are likely to be stable for energetic reason or can stabilized by surface impurities or can have slow drift if isolated enough. Then by using a +1 umbilic, in a cell having π phase shift between (local) ordinary and extraordinary, from an incoming right/left handed circularly polarized input, we will have a left/right circularly polarized optical vortex, with topological charge +2/-2. The use hometropic anchoring makes the cell fabrication intrinsically easier to achieve with respect to the azimuthal rubbing which can be done mechanically and is limited to charge +1 devices. A more involved holographic methods based on the use of UV curing polymer as rubbing layer, allow the design of more complex pattern of anchoring, as for example those exhibiting high order topological charge as negative ones as well, enabling the generation of high order optical vortices [98] not just +2 or -2 like for the direct use of umbilics. High order vortices can be created by cascading several SAM-to-OAM converter with topological charge +1 and wave plates.

4.3 Conclusions

In this chapter we have described the various methodologies to generate optical vortices, the first ones, SSPs, CGHs and mode converters act directly on the phase of the input beam thus couples the OAM degree of freedom to that of the matter. The second, based on the Pancharatnam-Berry effect, by rotating the polarization in order to introduce a geometric phase that can induce OAM. The last method, also the most recent, is under constant development. Moreover, with the use of LC all the methods described can be implemented by using SLMs (spatial light modulators) to shape the phase of the beam, or planar azimuthally aligned cell filled with LC. Both offer the creation of discrete devices and one device can be used to generate one optical vortex, at least for q-plate. Moreover the relative misalignment of beam and singularity embedded in the phase mask, the hologram or the spatially varying axis field can affect in a limitative way the quality of the obtained optical vortex [99].
In the next chapter we will show the practical implementation of OAM to SAM con-

verter based on umbilic like defects using LCLV as the latest provides, in some configurations, a self-centering and stabilized the defect with respect to the beam to be converted.

Chapter 5

Singular Optics in Liquid Crystal Light Valves

In this chapter we will demonstrate the practical implementation of the generation of optical vortices in liquid crystal light valves, using the defect created in the texture of the liquid crystal within the valve. To begin with, we introduce the self induced SAM to OAM conversion in liquid crystal light valve, which is the building block of reconfigurable SAM to OAM converters. The possibility of generating array of vortices and the achievement of SAM to OAM conversion will be investigated successively.

5.1 Optical vortex generation via self induced SAM to OAM conversion

5.1.1 Single Beam

We consider the LCLV described in the chapter 3. The bias is set to a value such that the voltage across the liquid crystal layer is slightly below the Freedericks transition voltage, this in order to have a defect free cell, and to be able to induce appreciable reorientation at relatively low optical powers. When a low power circularly polarized Gaussian probe beam is shone onto the LCLV, the BSO becomes more conductive in the center of the shone area and less far from it. The voltage across the LC layer acquires a bell shaped profile, with value over the Fredericks transition voltage when the bias is increased further and decreasing far from the axis of the beam. Due to this radial profile impressed by the beam, an umbilic like profile is induced and pinned on the axis of the incoming beam due to the radial transverse electric field generated

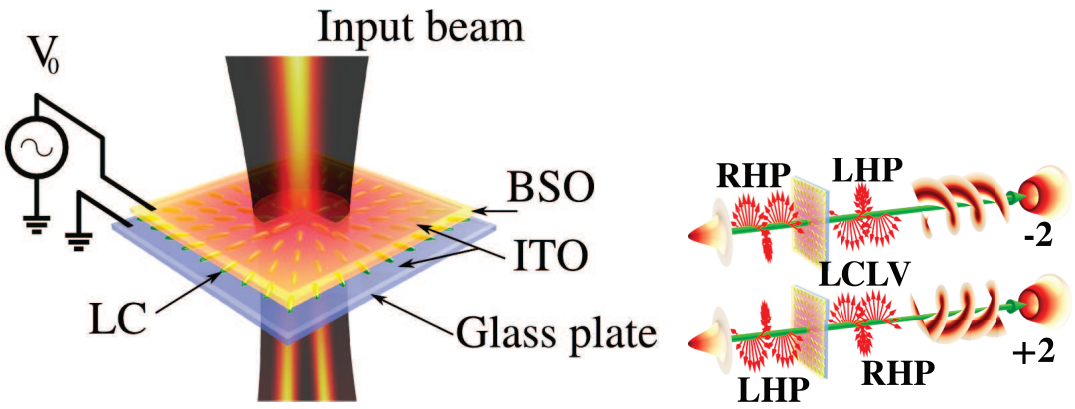

(a) (b)

Figure 5.1: Illustration of the self induction mechanism in the LCLV. A Gaussian beam sent on the BSO, will exit with a doughnut profile, an optical vortex with topological charge m such that $|m| = 2$. The phase helicity will depend on the helicity of the input beam which can be either +1 (left handed polarized beam) or -1 (right handed polarized beam).

by the non uniform voltage. This umbilic like defect is characterized by a varying azimuthal angle varying from 0 to 2π on the whole distorted region, i.e. of the form $\theta(r, \xi) = \xi + \theta_0(r)$, θ_0 taking into account eventual swirl, with varying polar angle which is null in the center and depending on the profile of the induced voltage, with value decreasing far from the illuminated region where the texture will be undistorted, i.e. homeotropic. Due to anisotropy of the nematic liquid crystal, it will behave like a PBOE with topological charge +1 able to couple the SAM and the OAM of the incoming incident beam. Therefore, a circular polarized non singular beam (without angular momentum) entering the defect free LCLV, in the ideal case, will exit with its polarization reversed and a phase dislocation with topological charge depending on the input polarization, thus a contra-polarized optical vortex with topological charge $|m| = 2$ sign depending on the polarization (see figure 5.1).

This self induced spin to orbital angular momentum conversion is different from that obtained by El Ketara et al [100]. Here the creation of the defect is mediated by the low frequency field via the photoconductive (BSO) layer. So low power input beam can be used while maintaining high efficiency, and the singular reordering due to the Gaussian beam [101] is negligible with respect to that of the electric field due to the power level used in this work.

To prove the vortex induction, a laser beam of wavelength $\lambda = 632.8$nm and power P = 0.55mW is focused on a diameter of 395μm onto the photoconductive side of the

LCLV. The input beam polarization is taken to be circular, either right handed polarized (RHP) or left handed polarized (LHP). To observe the created optical vortex, a quarter wave plate is inserted after the LCLV (see figure 5.2), the two circular polarization component are projected onto two linear orthogonal polarizations and a polarizer helps to select the component corresponding to the optical vortex. When the LCLV is unbiased, the collected intensity on the CCD/photodiode is zero. To observe the phase dislocation, beam splitters and mirrors are arranged in order to have a Mach-Zender interferometer with the LCLV on the principal arm. The half wave plate on the reference arm helps to adjust the polarization of the reference beam of the interferometer with respect to that of the linearly polarized optical vortex. In this way, we can control the contrast of the interference fringes. Two types of interferometers are arranged: in the first type, figure 5.2(a), the reference arm is weakly tilted such that the typical plane wave interferogram is obtained when the bias of the LCLV is turned off (with polarizers and quarter wave plates removed). In the second type, figure 5.2(b), an objective and a lens are inserted on the reference arm such that the interferogram with the LCLV removed consists of concentric rings. Typical snapshots of the observed intensity of

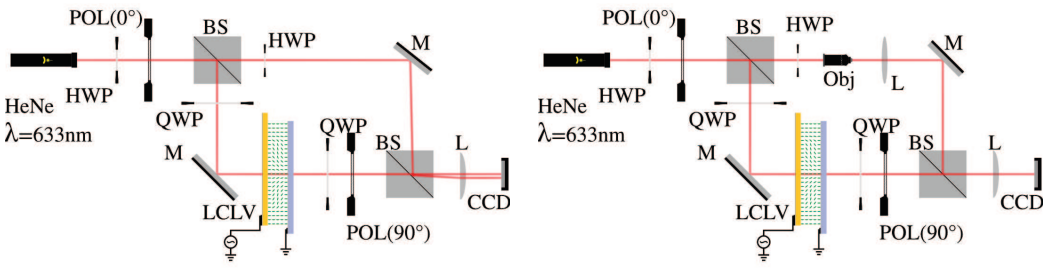

(a) (b)

Figure 5.2: Setup for the self induction of an optical vortex.POL: polarizer; QWP: quarter wave plate; HWP: half wave plate; Obj: microscope objective; M mirror; BS: beam splitter; CCD: CMOS camera; L: lens. LCLV liquid crystal light valve. In (a) the the two beams at the output of the Mach-Zehnder interferometer are weakly tilt on respect the other. In (b) the objective and the lens on the reference arm serve to control the relative curvature between the two wave front, with the Mach-Zehnder interferometer well aligned.

output beams and their interferograms in the two cases of polarization are shown in figure 5.3, (first row LHP input, second row RHP input) for the bias $V_{BIAS} = 24V$ at a frequency of 100Hz. The intensity profiles, figure 5.3 first column, show that the two beams have zero intensity on their axis, with a doughnut shaped profile typical of that

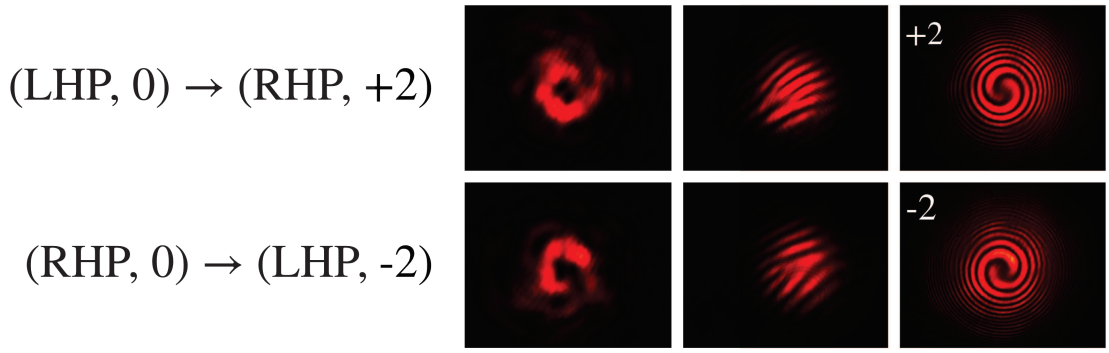

Figure 5.3: Optical vortex generation in LCLV via self induced SAM to OAM conversion. Labels correspond to the input polarizations and the SAM to OAM conversion. We show (from left to right) the output intensity profile, the forked interferogram and the spiral fringes. Booth the interferograms confirm the generation of an optical vortex of topological charge +2 for the LHP input and -2 for the RHP one.

of optical vortices. The output beam polarization for a LHP (RHP) input beam has been verified to be RHP (LHP). To check the presence of the singularity we use the interferometer in figure 5.2(a). We observe fork like interference patterns with dislocated lines. The number of dislocated lines is two for both polarizations, showing that the topological charge is in modulus 2 (number of dislocation lines). They are reversed one with respect to the other, confirming that they have opposite sign. To check the sign in an absolute way, we use the configuration in figure 5.2(a). The observed interferograms consist of two intertwined spirals. The spirals for the LHP input rotates clockwise (from the center of the vortex outward), and counterclockwise for the RHP input, with the observer pointing in the direction of the k-vector. The results are consistent with the spiral interferogram for a +2 charged optical vortex in the case of the LHP input and a -2 charged optical vortex for the RHP input.

Correspondingly, the spin to orbital angular momentum conversion is consistent with the presence of an umbilic like defect with winding number $q = 1$, presence confirmed by the spatially resolved polarimetry in figure 5.4. Note that due to the nature of the matter vortex, $m = \pm 2$ are the only possible values for the transferred topological charge.

To measure the transferred optical power into the vortex mode, we record the power P_2 of the LG_{02} like output mode when varying the bias voltage V_{BIAS} applied to the LCLV and for various input powers P. The sweep on the values of the bias is done by modulating the bias voltage with a linear ramp voltage from 0 to 1V with rise time large enough with respect to the LCLV response time in order to prevent dynamic effects.

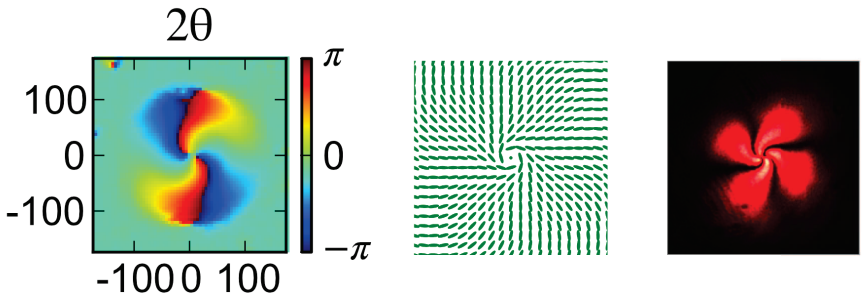

Figure 5.4: From left to right: spatially resolved polarimetry of an induced umbilic, 2D reconstructed nematic orientation, induced defect observed under crossed polarizers.

The measurements are carried out by placing a $\lambda/4$ wave plate on the path of the output beam, projecting the circularly converted RHP (LHP) for LHP (RHP) input, and the residual polarization components into two orthogonal linear polarizations, and measuring with a photodiode the intensity of the one carrying the topological charge. The results are reported in figure 5.5(a) first panel, where the value of the input power is marked along each curve. The threshold voltage V_{TH} at which the vortex form slightly depends on the input power and is shown in figure 5.5(b) with the experimental points in (black dots). The continuous curve is the best fit corresponding to the linear dependence of the BSO conductivity on the intensity, other parameters are considered constant [52]. For low optical power, even if the absorption of the BSO is lower at 633nm, the input beam makes it more conductive, with an increasing effective voltage across the LC with respect to the beam intensity. Due to the fact that the distorted area is comparable in size with the input Gaussian beam, efficiency has to be computed considering the overlap of the induced PBOE, which takes into account the position dependent efficiency and the beam shape. The conversion efficiency is, then:

$$\eta_2 = \sin^2\left(\frac{\bar{\Gamma}}{2}\right) = \int_0^\infty I(r)\sin^2\left[\frac{\Gamma(r)}{2}\right]\mathrm{d}r,$$

with $I(r)$ the normalized density of the input beam, Γ the local phase shift given by $\Gamma(r) = 2\pi\left(\bar{n}_e(r) - n_o\right)\frac{L}{\lambda}$, with

$$\bar{n}_e(r) = \frac{1}{L}\int_0^L n_e(\psi(r,z))\mathrm{d}z.$$

The dependence of the profile of the induced defect on the input power will make $\bar{\Gamma}$ power dependent. Nevertheless the transferred output power agrees qualitatively with

that of a planar cell in between crossed polarizers. The peak of the response curves corresponds to an overall phase retardation $\bar{\Gamma} = \pi$ between the ordinary and extraordinary components in the LC layer. The efficiency curves are reported in figure 5.5(a), second panel, with respect to the overdrive voltage $V_{BIAS} - V_{TH}$. The conversion efficiencies are quite high, and the first peaks are between 68% (4mW) and 92% (5mW). The nonlinear dependence of the peaks are attributable to the non linear modulation of the effective phase shift with respect to the power. For a further increase in the efficiency, the bias voltage can be increased adiabatically after the creation of the defect, the molecules in the LCLV bend toward the $x - y$ plane without the creation of other undesired ones that can ruin the quality of the generated optical vortex. This driving mechanism is robust, indeed, after the defect has been created, the 2π degenerated symmetry for the reorientation is broken. The configuration of the projected director field will evolve toward new one maintaining it topological charge as the molecules will move smoothly from their current positions to minimize the acute angle between them and the electric field.

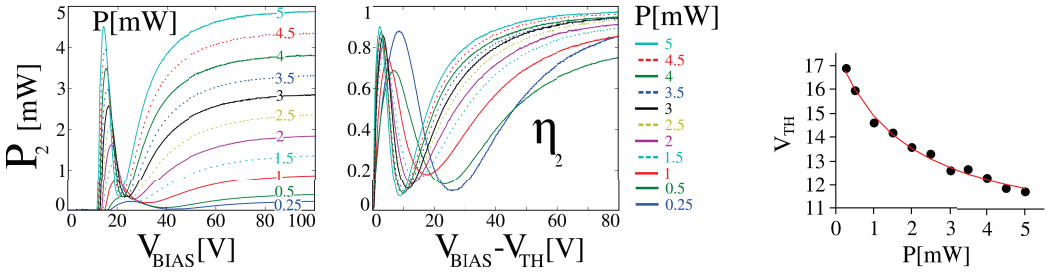

(a) (b)

Figure 5.5: (a) Power transfer curve and OAM conversion efficiency.(b) Threshold versus the input power. Black dots correspond to the experimental values, the continuous curve is the best fit using only the linear dependance of the BSO conductance on the input intensity

Finally, in figure 5.6(a) and 5.6(b), we show the recorded intensity profiles and the interferograms for the LHP and RHP polarized Gaussian input beam respectively. Labels correspond to the applied bias. The obtained optical vortices exhibit a good quality. Note the that profiles were not spatially filtered.

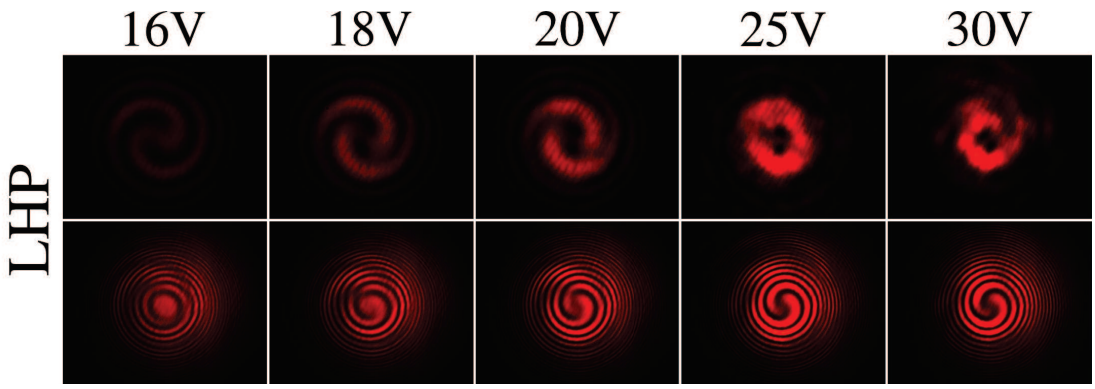

(a)

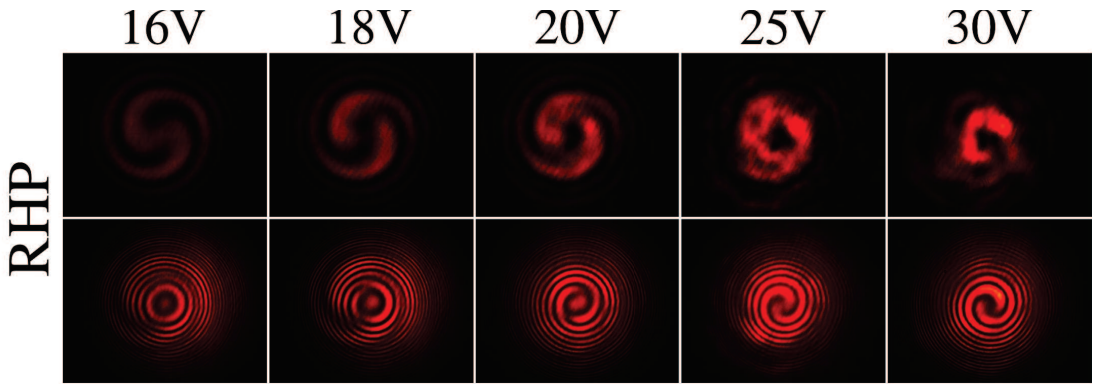

(b)

Figure 5.6: Beam profiles and interferograms for the LHP (a) and the RHP (b) input beam. Labels correspond to the applied bias to the LCLV.

5.1.2 Self-induced SAM to OAM conversion for multiple incoherent sources.

To demonstrate the potential of the LCLV scheme in generating optical vortices from non singular beams by using the self SAM to OAM conversion, we can consider using it for the simultaneous generation of multiple incoherent optical vortices using multiple sources, irrespective of the sign of their topological charge (i.e input polarization). As a proof of concept, the setup in figure 5.2(a) is modified in order to launch two adjacent input Gaussian beams on the conductive side of the LCLV biased at 24V (see figure 5.7). The laser beams are adjusted at the same power level, P=0.55mW and their diameters is about 315μm on the BSO. The distance between the beams is about the same value as the spot diameters in order to test high density capabilities.

We verify that two stable and independent vortices are obtained, see for instance

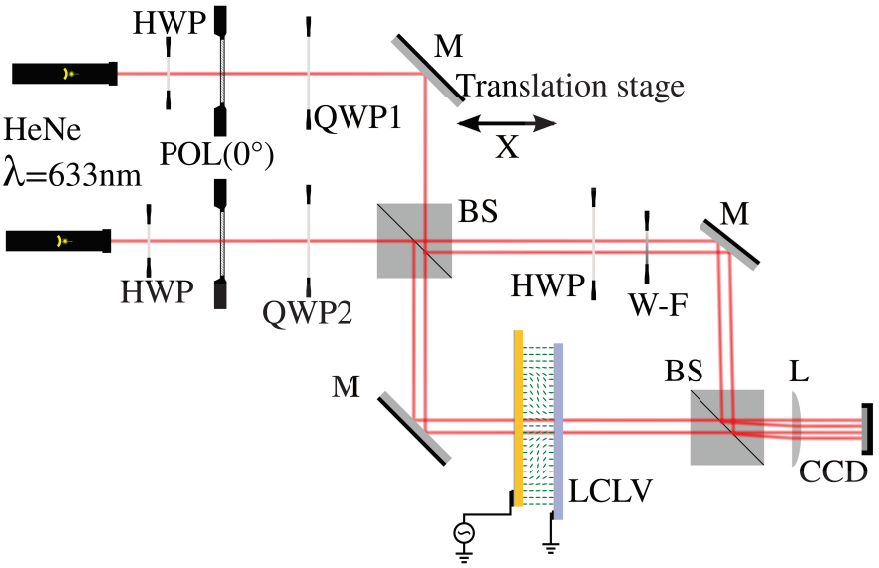

Figure 5.7: Experimental setup for the self SAM to OAM conversion of independent sources. HWP: half wave plate; QWP: quarter wave plate. BS: beam splitter; M: mirror; W-F: wheal filter. CCD: CMOS camera. L: lens. LCLV liquid crystal light valve

figure 5.8, first image. The interferograms correspond to (from left to right) RHP-RHP, LHP-LHP, RHP-LHP input polarization configurations. With the help of the LCLV and the self-induced spin to orbital angular momentum conversion, we can generate array of mutually incoherent optical vortices with topological charge $|m| = 2$ and with arbitrary sign depending on the modulation pattern of the beam helicity.

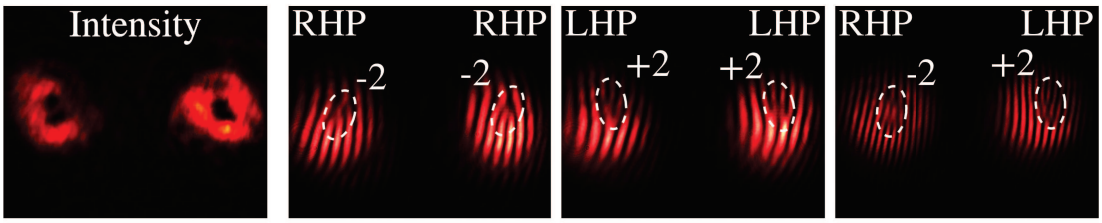

Figure 5.8: Intensity profiles of the output beams showing the doughnuts. Interferograms for RHP-RHP, LHP-LHP, RHP-LHP polarized inputs.

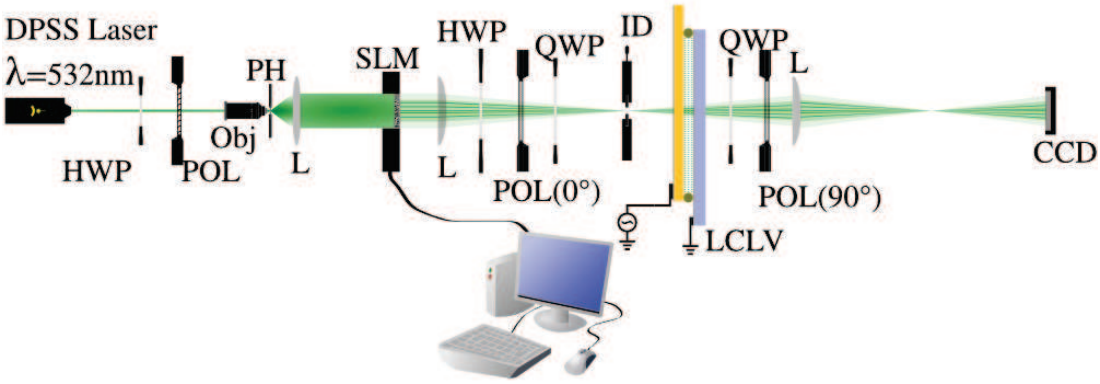

Figure 5.9: Experimental setup for the generation of array of optical vortices.SLM: Spatial Light Modulator; LCLV: Liquid Crystal Light Valve; L: Lens; Obj: Objective; PH: pinhole; POL: Polarizer; HWP: half wave plate; QWP: quarter waveplate; ID iris diaphragm.

5.2 Dense array of optical vortices in LCLV

Further integration can be made based on the previous experiments. Instead of using multiple sources, a spatial light modulator (SLM) is used to modulate a writing beam at $\lambda = 532$nm with a planar wavefront at the SLM plane, see figure 5.9 for the experimental setup. The power density is about 3mW/cm^2, and modulated with a honeycomb pattern with the bright spots at the vertices of the hexagons. The polarizer and the quarter waveplate between the SLM and the LCLV serve to create an array of circular polarized beamlets on the sensitive side of the LCLV. Those, at output, are used to select the part of the beam carrying the optical vortices. Operating at shorter wavelengths permit to use the BSO in the most sensitive region [52], this in order to use fairly low optical power for the vortex generation. Note that the circular polarization converters at the input and output can be removed. In our case, this leads to vectorial optical vortices with zero net topological charge [102, 103].

The generated array of optical vortices and the corresponding in defects induced in the medium are shown in figure 5.10 for a bias voltage of 17V.

Moreover by illuminating the generated array with 633nm circular polarized probe beam, it wave front is impressed with the singularities in the LCLV. In figure 5.11, we report the plane wave interferogram, for low voltages, the dislocation are well localized, increasing the voltage causes the umbilics to connect and generate other singularities with ± 1 sign, this reflect in the apperance of other dislocations in the wave front.

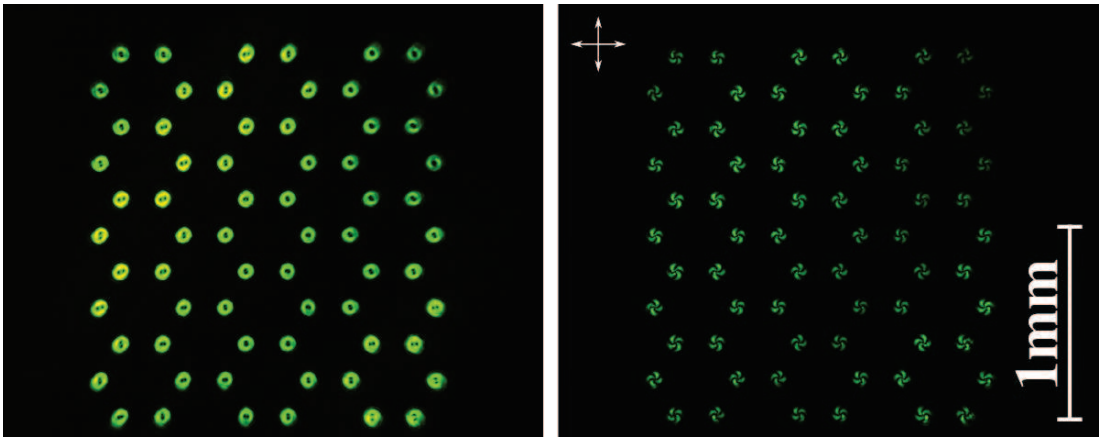

Figure 5.10: Left figure: hexagonal array of optical vortices. The power density of the writing beam at the LCLV level is about 3mW/cm^2. The texture of the nematic liquid crystal under crossed polarizers showing the location of the defects.

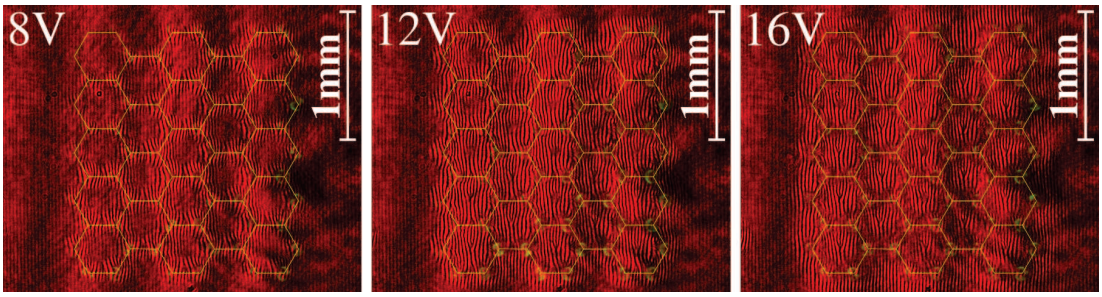

Figure 5.11: Hexagonal array of optical vortices for increasing bias.

5.3 Orbital angular momentum modulation via frustrated state

Until now, to create optical vortices, we rely on the defect mediate SAM to OAM conversion. The generated defect has a winding number +1 permitting the generation of optical vortices of charge +2 and -2 respectively for LHP and RHP polarized input. Although this method provides the ability to generate a class of vortices of topological charge integer multiples of 2 (we remind that the cascading method be can used), we have to switch the helicity from +1 to -1 in order to change the sign of the vortex from + to -.

To complete the generation scheme, i.e. the changing of the sign of the vortex without switching the polarization of the input beam, we need to change the sign of the topological charge of the equivalent induced PBOE, i.e., the topological charge of the

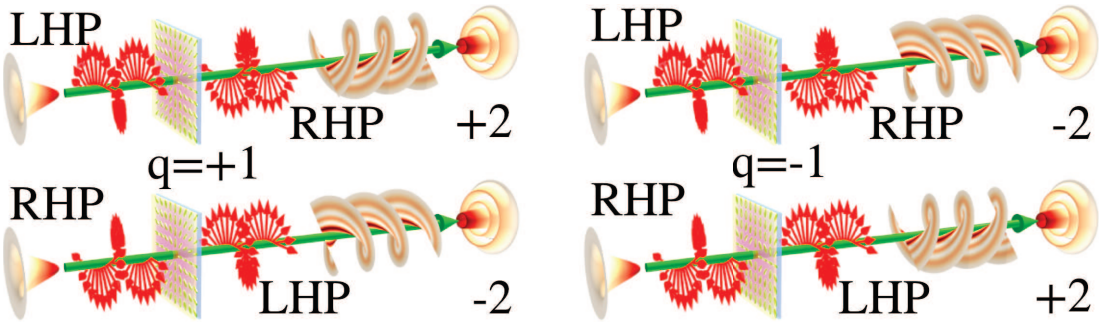

Figure 5.12: Illustration of the four way of implementing SAM-OAM modulation.

Input state	PBOE q=1		PBOE q=-1	
$\|+\hbar, 0>$	$\|-\hbar, +2\hbar>$	$\Delta L_z = 0$	$\|-\hbar, -2\hbar>$	$\Delta L_z = +4\hbar$
$\|-\hbar, 0>$	$\|+\hbar, -2\hbar>$	$\Delta L_z = 0$	$\|+\hbar, +2\hbar>$	$\Delta L_z = -4\hbar$

Table 5.1: SAM to OAM coupling table for the 4-way modulator. $|\sigma\hbar, m\hbar>$ correspond to the input or output AM state for the incoming photons in the form of |SAM, OAM >. ΔL_z the AM per photon exchanged with the PBOE.

embedded defect. This can only be accomplished by using a -1 umbilic. As we learn from the previous chapters (3), -1 umbilics are not generated spontaneously nor by a direct writing at least for radially symmetric writing beam. However, a -1 umbilic can be generated by frustration. To do so, we can dynamically create two +1 defects and force them to connect. Due to the incompatibility of the far field of the director field from the two defects, a -1 defect is created by frustration. In this way, a full modulation scheme is implemented by using alternatively a + defect written directly and a -1 defect written by frustration. We summarized the modulation scheme in figure5.12 with total angular momentum balance in table 5.1.

The implementation is done by using a 532nm writing beam with intensity $250\mu W/cm^2$. The beam is modulated with the SLM in order to create alternatively a +1 defect and two +1 defects that are forced to touch one with each other. We increase the illumination spot size until the two defects touch, producing an umbilic of winding number -1. The probe beam power is set to $1.5\mu W$ is aligned to the barycenter of the two spots and coincides also with center of the writing beam when a single illuminated beam is used (see figure 5.13).

The OAM modulation interferograms are shown in figure 5.14. The picture shown corresponds to what it is seen with the k-vector of the beam pointing toward the observer. In this configuration the positively charged vortices will have their helix (spiral fringes from the center outward) rotating counterclockwise, and clockwise for

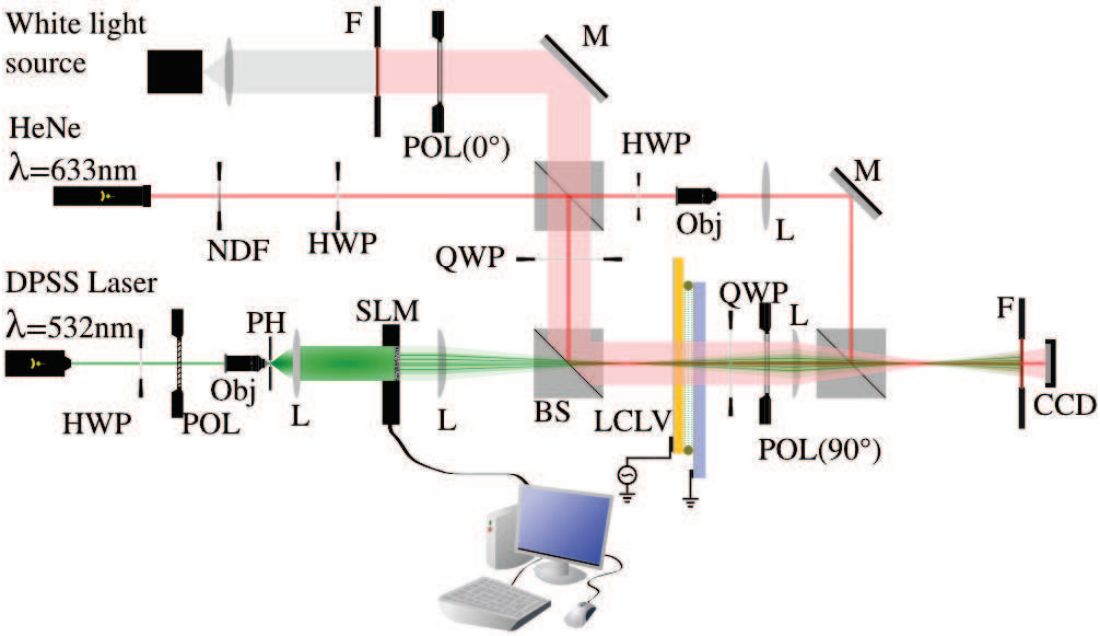

Figure 5.13: Experimental setup for the four way SAM-OAM coupling. The white light source is used to check the presence of other defects in the texture. BS: beam splitter, CCD: CMOS camera, F: red glass filter, HWP: half waveplate, QWP: quarter wave plate, L: lens, M: mirror, NDF: neutral density filter, Obj: microscope objective, P: polarizer, PH: pinhole.

negatively charged helix. For an RHP/LHP input a +2/-2 vortex is created when we use one writing spot,q=+1, and -2/+2 vortex is created when two adjacent writing spots are used, q=-1.

For completeness, we provide also the intensity profile for the vortex at various bias voltages and with different types of modulation schemes. When a +1 defect is used, the optical vortex exhibits the usual doughnut profile with the appearance of concentric rings, with their number varying. This is due to the radial dependency of the efficiency and the radial phase modulation of the optical vortex due to the swirl (the phase factor $e^{\pm i2\theta_0(r)}$). Moreover, it has been proven that the optical vortices obtained from an LG_{00} mode are not $LG_{n,\pm 2}$ modes, in the ideal case they are the so-called Kummer beams [93, 104], with the azimuthal phase factor ± 2. When a q=-1 defect is used, evident distortions of the vortex profile are noticed, with the appearance or rings as in the case previous case. Nevertheless, this distortion due to the swirl, which in this case is not a pure radial one, i.e, $\theta_0 = \theta_0(r, \xi)$, can be controlled by applying auxiliary field in the $x - y$ plane.

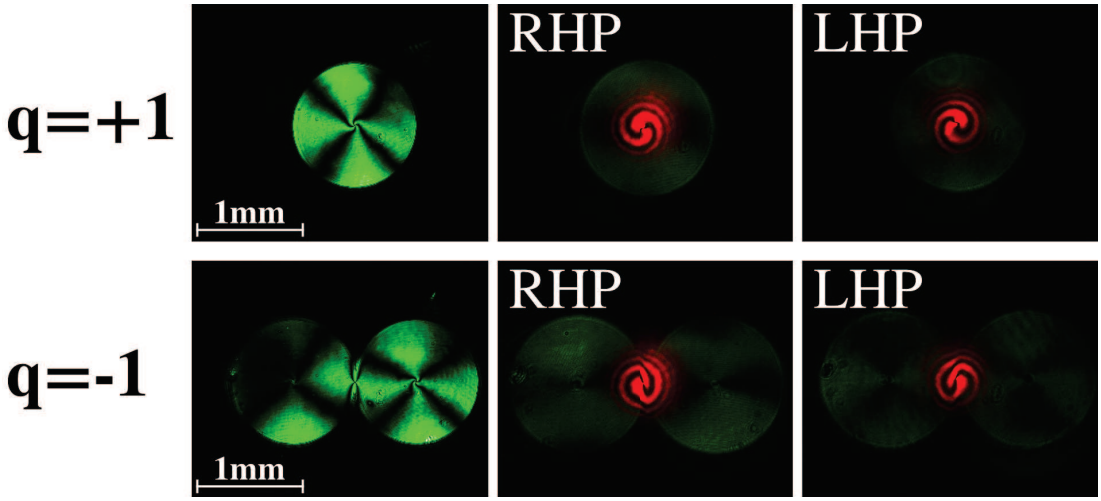

Figure 5.14: Four way SAM-OAM coupling. In the left column the generated defect(s), in central and right columns the interferogram for a circularly polarized input beam. The labels indicates the handedness of the polarization.

5.4 Conclusions

In this final chapter we have shown the essential features of the use of LCLV to generate optical vortices in homeotropic nematic liquid crystal cells filled with negative anisotropic material. This experimental platform offers the capability of generating optical vortices dynamically via the self induced SAM to OAM conversion mechanism. We demonstrate the ability to generate vortex arrays with arbitrary topological charge, supplemented with that of vector vortices. Finally a four way SAM to OAM modulation is demonstrated using external controlled beam, achieving the design of compact

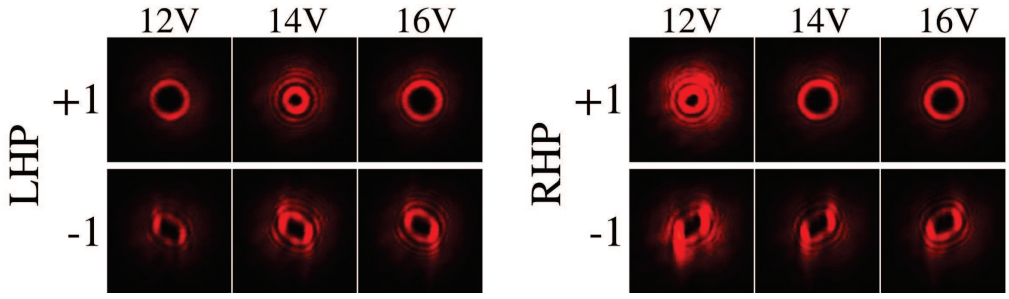

(a) LHP (b) RHP

Figure 5.15: Beam profiles for LHP polarized input(a) and RHP polarized input(b). The presence of rings show the modulation of the radial number of the optical vortex.

SAM to OAM couplers. This devices could be used in quantum communications.

Conclusion

While soft matter is, in general, a versatile playground for optics, nematic liquid crystals are an even richer workbench as they also encompass anisotropy, nonlinearity, electro-optic response, nonlocality. Owing to their response to low frequency voltages as well as optical frequency electric fields, nematic liquid crystals were used in this work to investigate some advance features of optical spatial solitons, nematicons, as well as of singular beams or vortices. In the area of optical spatial solitons, I have demonstrated that particular arrangements of electrodes in planar liquid crystalline cells can lead to in-plane steering of solitons with large angular deflections. An overall angular deflection of 55 degrees was achieved for the first time by means of refraction and total internal reflection of soliton waveguides. The latter results are relevant in the domain of integrated optics, as solitons can be effectively used as deformable waveguides for signals. In the area of singular optics, using planar geometries with a photoconductive layer, i.e. liquid crystal light valves, I have demonstrated that a homeotropic alignment of nematic liquid crystals, combined with the application of a bias voltage and an external illumination, can induce the controlled formation of matter defects or vortices. The latter, in turn, behave as q-plates and are capable of changing both the polarization and the topological charge of input beams. Finally, I have realized two-dimensional arrays of matter vortices in various geometric arrangements, with the first realization to date of compact and tunable matrices of packed optical vortices for signal processing.

Appendix A

Voltage distribution in Liquid crystal cell

A.1 Homeotropic configuration

For the hometropic cell the anistropic Laplace equation, (equation 3.6) can be rewritten in the following form:

$$\frac{\epsilon_\perp}{\epsilon_\parallel}\nabla_T^2 V + \frac{\partial^2 V}{\partial^2 z} + F = 0 \ , \tag{A.1}$$

where $F = \nabla \cdot \underline{\underline{\delta}} \cdot \nabla V$ with

$$\underline{\underline{\delta}} = \frac{\epsilon_a}{\epsilon_\perp}\left(\hat{n}\hat{n} - \vec{z}\vec{z}\right) = \frac{\epsilon_a}{\epsilon_\perp}\left(\hat{n}\hat{n} - \vec{z}\vec{z}\right) = \frac{\epsilon_a}{\epsilon_\perp}\left[\vec{z}(\hat{n}-\vec{z}) + (\hat{n}-\vec{z})\vec{z} + (\hat{n}-\vec{z})(\hat{n}-\vec{z})\right]$$

We can proceed by Fourier transforming the equation A.1 with respect to the transverse dimension:

$$-\frac{\epsilon_\perp}{\epsilon_\parallel}q^2\tilde{V}(\vec{q},z) + \frac{\partial^2 \tilde{V}}{\partial^2 z} + \tilde{F}(\vec{q},z) = 0 \ . \tag{A.2}$$

The solution of this equation is formally:

$$\tilde{V}(\vec{q},z) = \tilde{V}(\vec{q},0)\frac{\sinh\left(Q(L-z)\right)}{\sinh\left(QL\right)} + \tilde{V}(\vec{q},L)\frac{\sinh\left(Qz\right)}{\sinh\left(QL\right)} + \int_0^L G_{1D}(\vec{q},z,z')\tilde{F}(z',\vec{q})dz' \ , \tag{A.3}$$

with $Q = q\sqrt{\frac{\epsilon_\perp}{\epsilon_\parallel}}$, and

$$G_{1D}(\vec{q}, z, z') = \begin{cases} \frac{\sinh(Q(L-z))}{Q\sinh(QL)}\sinh(Qz')\,,\ 0 \le z' \le z \\ \frac{\sinh(Qz)}{Q\sinh(QL)}\sinh(Q(L-z'))\,,\ z \le z' \le L \end{cases}$$

the Green function of the 1D problem.
By anti-transforming the equation A.3 one gets the profile of the voltage across the cell. The expression of V is given by:

$$V(\vec{r}, z) = \int G_0(\vec{r}-\vec{r}', z)V(\vec{r}', 0)d\vec{\mathbf{r}}\prime + \int G_L(\vec{r}-\vec{r}', z)V(\vec{r}', L)d\vec{\mathbf{r}}\prime + \int G(\vec{r}-\vec{r}', z, z')F(\vec{r}', z')d\vec{\mathbf{r}}' \ , \tag{A.4}$$

with

$$G_0(\vec{r}-\vec{r}', z) = \frac{1}{(2\pi)^2}\int \frac{\sinh(Q(L-z))}{\sinh(QL)} e^{i\vec{q}\cdot(\vec{r}-\vec{r}')}d\vec{\mathbf{q}}\ ,$$

$$G_L(\vec{r}-\vec{r}', z) = \frac{1}{(2\pi)^2}\int \frac{\sinh(Qz)}{\sinh(QL)} e^{i\vec{q}\cdot(\vec{r}-\vec{r}')}d\vec{\mathbf{q}}\ ,$$

$$G(\vec{r}-\vec{r}', z, z') = \frac{1}{(2\pi)^2}\int G_{1D}(\vec{q}, z, z') e^{i\vec{q}\cdot(\vec{r}-\vec{r}')}d\vec{\mathbf{q}}\ .$$

G_0 and G_L represent the Green function of the surface terms at $z = 0$ and $z = L$ respectively and G the Green function of the bulk terms.
Clearly the bulk term depends on V itself and on the tilt $\hat{n} - \vec{z}$, the full solution can be computed only numerically, or by using perturbative methods in witch high order terms can be computed using recursively terms of low order. Unfortunately the expression of the above Green functions cannot be written in close form. Let us consider the surface terms, we take only the second term ($z = L$), the fisrt one correspond to the contribution of the ground electrode $z = 0$ which is set to a constant voltage distribution and therefore can be set to zero. We assume that the surface voltage varies with a spatial length scale Λ, we can write $V(\vec{r}, z) = V(\vec{r}/\Lambda, z/L)$, changing $\vec{r} = \Lambda\vec{R}$ $z = L\zeta$

$$V(\vec{R}, \zeta) = \iint \frac{\sinh(\zeta QL/\Lambda)}{\sinh(QL/\Lambda)} e^{i\vec{q}\cdot(\vec{R}-\vec{R}')}V(\vec{R}', 1)d\vec{\mathbf{q}}d\vec{\mathbf{R}}'$$

(we've made the change $\vec{q} \to \vec{q}/\Lambda$). If the applied surface voltage varies slowly respect to the cell thickness we have $L/\Lambda << 1$, we can expand

$$\frac{\sinh(\zeta QL/\Lambda)}{\sinh(QL/\Lambda)} \approx \zeta + \frac{1}{6}\zeta(\zeta^2 - 1)Q^2(L/\Lambda)^2 + O((L/\Lambda)^4)$$

after some algebra,

$$V(\vec{r},z) = \frac{z}{L}V(\vec{r},L) + \frac{1}{6}(\frac{z^3}{L^3} - \frac{z}{L})\frac{\epsilon_\perp}{\epsilon_\parallel}L^2\nabla_T^2 V(\vec{r},L) \ .$$

The second order correction being small, we will keep only the first order term.

Appendix B

Derivation of the Ginzburg Landau equation

B.1 Ginzburg Landau equation

In this section we will provide the full derivation of the Ginzburg Landau equation for the molecule dynamics in the homeotropic condition. Let us consider the equation 3.5 which can be rewritten in the following form

$$\begin{aligned}\gamma\frac{\partial\hat{n}}{\partial t} =& K_3\left[\nabla^2\hat{n} - (\hat{n}\cdot\nabla^2\hat{n})\hat{n}\right] + (K_1 - K_3)\left[\nabla\nabla\cdot\hat{n} - (\hat{n}\cdot\nabla\nabla\cdot\hat{n})\hat{n}\right] \\ &+ 2(K_3 - K_2)\left(\hat{n}\cdot\nabla\times\hat{n}\right)\left[\nabla\times\hat{n} - (\hat{n}\cdot\nabla\times\hat{n})\hat{n}\right] + (K_3 - K_2)\nabla(\hat{n}\cdot\nabla\times\hat{n})\times\hat{n} \\ &+ \epsilon_a^{\Omega}(\hat{n}\cdot\vec{E})[\vec{E} - (\hat{n}\cdot\vec{E})\hat{n}\ .\ ]\end{aligned} \tag{B.1}$$

To derive the third order approximate equation, we need to expand it in terms of Taylor series of the smallness parameter which in this case will be $\epsilon = \sqrt{\left(\frac{V}{V_{TH}}\right)^2 - 1}$. It is worthwhile to notice that the smallness parameter controls also the transverse spatial scale, so that the effect of the transverse gradient operator has to be taken into account: it acts like a first order term in ϵ. With these assumptions, by projecting the equation B.1 x and the y we have:

for the first term in the lhs. of B.1:

$$K_3 \begin{cases} \nabla^2 n_x + ((\partial_z n_x)^2 + (\partial_z n_y)^2) n_x \\ \\ \nabla^2 n_y + ((\partial_z n_x)^2 + (\partial_z n_y)^2) n_y \ . \end{cases} \tag{B.2}$$

Projected on the first mode, i.e. $n_x = X(x,y)\sin\frac{\pi z}{L}$ and $n_y = Y(x,y)\sin\frac{\pi z}{L}$ and every terms projected on $\sin\frac{\pi z}{L}$, gives:

$$K_3 \begin{cases} \nabla_t^2 X - \frac{\pi^2}{L^2} X + \frac{1}{4}\frac{\pi^2}{L^2}(X^2+Y^2)X \\ \\ \nabla_t^2 Y - \frac{\pi^2}{L^2} Y + \frac{1}{4}\frac{\pi^2}{L^2}(X^2+Y^2)Y \ . \end{cases} \tag{B.3}$$

For the second term in lhs. of B.1, we have:

$$(K_1 - K_3) \begin{cases} \partial_x^2 n_x + \partial_{xy}^2 n_y - \frac{1}{2}\partial_{xz}^2(n_x^2+n_y^2) - [\partial_{zx}^2 n_x + \partial_{zy}^2 n_y - \frac{1}{2}\partial_z^2(n_x^2+n_y^2)]n_x \\ \\ \partial_{yx}^2 n_x + \partial_y^2 n_y - \frac{1}{2}\partial_{yz}^2(n_x^2+n_y^2) - [\partial_{zx}^2 n_x + \partial_{zy}^2 n_y - \frac{1}{2}\partial_z^2(n_x^2+n_y^2)]n_y \ , \end{cases} \tag{B.4}$$

which projected on the first mode gives:

$$(K_1 - K_3) \begin{cases} \partial_{xx}^2 X + \partial_{xy}^2 Y - \frac{\pi^2}{L^2}\frac{1}{2}(X^2+Y^2)X \\ \partial_{yx}^2 X + \partial_{yy}^2 Y - \frac{\pi^2}{L^2}\frac{1}{2}(X^2+Y^2)Y \ . \end{cases} \tag{B.5}$$

For the third and fourth terms we have, defining $\phi = \hat{n}\cdot\nabla\times\hat{n} \approx -n_x\partial_z n_y + n_y\partial_z n_x + \partial_x n_y - \partial_y n_x$, the following:

$$(K_3 - K_2) \begin{cases} -2\phi\partial_z n_y - n_y\partial_z\phi + \partial_y\phi \\ \\ 2\phi\partial_z n_x + n_x\partial_z\phi - \partial_x\phi \ . \end{cases} \tag{B.6}$$

The projection on the first mode gives:

$$(K_3 - K_2) \begin{cases} \partial_{yx} Y - \partial_{yy}^2 X \\ \\ \partial_{xy} X - \partial_{xx}^2 Y \ . \end{cases} \tag{B.7}$$

The fifth term in the lhs. of the equation B.1 if we consider a constant uniform electric field and neglect the feedback of the reorientation on the voltage distribution, gives:

$$-\epsilon_a^\Omega E^2 \begin{cases} (1-(n_x^2+n_y^2))n_x \\ \\ (1-(n_x^2+n_y^2))n_y \ , \end{cases} \tag{B.8}$$

with $E = V_s/L$, Vs the voltage across the liquid crystal layer.

It projection on the first mode gives:

$$-\epsilon_a^\Omega E^2 \begin{cases} (1-\frac{3}{4}(X^2+Y^2))X \\ \\ (1-\frac{3}{4}(X^2+Y^2))Y \ . \end{cases} \tag{B.9}$$

Summing according to the complex representation $A = X + iY$ and defining $\partial_x + i\partial_y = \partial_\eta$ we have the following

$$\gamma\partial_t A = \mu A - \alpha|A|^2 A + \frac{K_1+K_2}{2}\nabla^2 A + \frac{K_1-K_2}{2}\partial_{\eta\eta}^2 \bar{A} \tag{B.10}$$

with $\mu = -\epsilon_a^\Omega E^2 - K_3\frac{\pi^2}{L^2}$, $\alpha = -\frac{3}{4}\epsilon_a^\Omega E^2 - \frac{\pi^2}{4L^2}(3K_3 - 2K_1)$

B.2 Corrective terms to the Ginzburg Landau equation

So far we have considered a constant bias voltage on the cell. In this case due to the non uniformity of the applied bias, the effect of the transverse electric field has to be considered. Moreover the transverse electric filed is small with respect to the longitudinal one, i.e., for V_s varying over a length scale Λ, $V(\vec{r},z) = \frac{z}{L}V_s(\vec{r}/\Lambda)$, $E_z = \frac{1}{L}V_s(\vec{r}/\Lambda)$, $\vec{E}_T = \frac{z}{L\Lambda}\nabla_{\vec{R}}V_s(\vec{R})|_{\vec{R}=\vec{r}/\Lambda}$, the ratio is in the order z/Λ which by definition is very small. Still, we should consider terms up to third order in the mix product of the transverse component of the electric field and the director. By projecting the

electric contribution of the equation on the x and y axis we get:

$$\epsilon_a^\Omega \begin{cases} ((E_x n_x + E_y n_y) + E_z - \frac{1}{2}E_z(n_x^2 + n_y^2))E_x - (2E_z(n_x E_x + n_y E_y) + (1 - n_x^2 - n_y^2)E_z^2)n_x \\ \\ ((E_x n_x + E_y n_y) + E_z - \frac{1}{2}E_z(n_x^2 + n_y^2))E_y - (2E_z(n_x E_x + n_y E_y) + (1 - n_x^2 - n_y^2)E_z^2)n_y \ . \end{cases} \tag{B.11}$$

We can now consider the first longitudinal modes. With $P = X\partial_x V_s + Y\partial_y V$, we have:

$$\epsilon_a^\Omega \begin{cases} \left[(\frac{1}{3} - \frac{1}{2\pi^2})P + \frac{2}{\pi}E - \frac{1}{2}\frac{4}{3\pi}E(X^2 + Y^2)\right]\partial_x V_s - \left[2EP\frac{4}{3\pi} + E^2 - \frac{3}{4}E^2(X^2 + Y^2)\right]X \\ \\ \left[(\frac{1}{3} - \frac{1}{2\pi^2})P + \frac{2}{\pi}E - \frac{1}{2}\frac{4}{3\pi}E(X^2 + Y^2)\right]\partial_y V_s - \left[2EP\frac{4}{3\pi} + E^2 - \frac{3}{4}E^2(X^2 + Y^2)\right]Y \ , \end{cases} \tag{B.12}$$

and summing according to B.1,

$$\frac{2}{\pi}E\partial_\eta V_s + \frac{1}{2}(\frac{1}{3} - \frac{1}{2\pi^2})|\partial_\eta V_s|^2 A + \frac{1}{2}(\frac{1}{3} - \frac{1}{2\pi^2})(\partial_\eta V_s)^2\bar{A} - \frac{4}{3\pi}E\partial_{\bar{\eta}}V_s A^2 - \frac{2}{\pi}E\partial_\eta V_s|A|^2 - E^2(1 - \frac{3}{4}|A|^2)A \ . \tag{B.13}$$

Then the modified Ginzburg-Landau equation read as:

$$\gamma\partial_t A = A_o + \mu A + \mu_*\bar{A} + \beta|A|^2 + \beta_* A^2 - \alpha|A|^2 A + \frac{K_1 + K_2}{2}\nabla^2 A + \frac{K_1 - K_2}{2}\partial^2_{\eta\eta}\bar{A} \tag{B.14}$$

with $A_0 = \epsilon_a^\Omega \frac{2}{\pi}E\partial_\eta V_s$ $\mu = -\epsilon_a^\Omega E^2 - K_3\frac{\pi^2}{L^2} + \epsilon_a^\Omega\frac{1}{2}(\frac{1}{3} - \frac{1}{2\pi^2})|\partial_\eta V_s|^2$, $\mu_* = \epsilon_a^\Omega\frac{1}{2}(\frac{1}{3} - \frac{1}{2\pi^2})(\partial_\eta V_s)^2$ $\alpha = -\frac{3}{4}\epsilon_a^\Omega E^2 - \frac{\pi^2}{4L^2}(3K_3 - 2K_1)$ $\beta = -\epsilon_a^\Omega\frac{2}{\pi}E\partial_\eta V_s$ $\beta_* = -\epsilon_a^\Omega\frac{4}{3\pi}E\partial_{\bar{\eta}}V_s$

Publications and Conferences

Publications

A. Alberucci, A. Piccardi, R. Barboza, O. Buchnev, M. Kaczmarek and G. Assanto *Interactions of accessible solitons with interfaces in anisotropic media: the case of uniaxial nematic liquid crystals* NJP. **15** 4, 043011 (2013)

R. Barboza, T. Sauma, U. Bortolozzo, G. Assanto, M.G. Clerc and S. Residori *Characterization of the vortex-pair interaction law and nonlinear mobility effects* NJP. **15** 1, 013028 (2013)

R. Barboza, U. Bortolozzo, G. Assanto and S. Residori *Optical Vortex Generation in Nematic Liquid Crystal Light Valves.* Mol. Cryst. Liq. Cryst. **572** 1, 24-30 (2013)

R. Barboza, U. Bortolozzo, G. Assanto, M. G. Clerc, E. Vidal-Henriquez and S. Residori *Vortex induction via anisotropy self-stabilized light-matter interaction* Phys. Rev. Lett. **109** (14), 143901 (2012)

A. Piccardi, A. Alberucci, R. Barboza, O. Buchnev, M. Kaczmarek and G. Assanto *In-plane steering of nematicon waveguides across an electrically tuned interface* Appl. Phys. Lett. **100**, 251107 (2012)

G. Assanto, A. Piccardi, R. Barboza and A. Alberucci *Electro-optic steering of nematicons* Phot. Lett. Pol. **4** (1), 2-4 (2012)

R. Barboza, A. Alberucci, G. Assanto *Electro-optic beam steering with nematicons* Mol. Cryst. Liq. Cryst. **558**, 12-21 (2012)

R. Barboza, A. Alberucci, G. Assanto *Large electro-optic beam steering with Nematicons* Opt. Lett. **36** (14), 26113 (2011)

Conferences

Generation of optical vortices in liquid crystal light-valves, **EOS Annual Meet. 2012**, Aberdeen (UK), Sept. 25-28, 2012

In-plane interaction of spatial solitons with bias-tuned interfaces, **EOS Annual Meet. 2012**, Aberdeen (UK), Sept. 25-28, 2012

Generation of optical vortices in liquid crystal light-valves, **10th Meeting SICL 2012**, Roma (ITALY), June 21-23, 2012

Optical vortex generation via induced singular reorientation in nematic liquid crystal light valve. **13th International Symposium on Colloidal and Molecular Electrooptics**, Ghent (BELGIUM), Sept. 02-05, 2012

Recent results on Nematicons, **NOA 2011-Nonlinear Optics Applications**, Toruń (POLAND), Sept. 14-17, 2011 [Invited]

Planar Steering of Light-Induced Waveguides via Voltage Controlled Interface, **2nd School of the Italian Liquid Crystal Society**, Erice (ITALY), July 03-10, 2011

Planar Steering of Light-Induced Waveguides via Voltage Controlled Interface, **Fotonica 2011:** 13° **Convegno Nazionale delle Tecnologie Fotoniche**, Genova (ITALY), May 09-11, 2011.

References

[1] P. G. De Gennes, "Short range order effects in the isotropic phase of nematics and cholesterics," *Molecular Crystals and Liquid Crystals*, vol. 12, no. 3, pp. 193–214, 1971. [Online]. Available: http://www.tandfonline.com/doi/abs/10.1080/15421407108082773 4

[2] L. Blinov, *Structure and properties of liquid crystals*, ser. Topics in applied physics. Springer Netherlands, 2011. 4

[3] P. G. de Gennes and J. Prost, *The Physics of Liquid Crystals (International Series of Monographs on Physics)*, 2nd ed. Oxford University Press, USA, Aug. 1995. 4, 7, 23, 24, 25, 58

[4] B. Y. Zel'dovich and N. V. Tabiryan, "Orientational optical nonlinearity of liquid crystals," *Soviet Physics Uspekhi*, vol. 28, no. 12, p. 1059, 1985. [Online]. Available: http://stacks.iop.org/0038-5670/28/i=12/a=R01 8, 25

[5] I. C. Khoo, "Nonlinear optics of liquid crystalline materials," *Physics Reports*, vol. 471, no. 56, pp. 221 – 267, 2009. [Online]. Available: http://www.sciencedirect.com/science/article/pii/S0370157309000271 8, 9

[6] L. Vicari, *Optical Applications of Liquid Crystals*, ser. Series in Optics and Optoelectronics. Taylor & Francis, 2010. [Online]. Available: http://books.google.fr/books?id=Rmp0GJnjORIC 9

[7] S. Wu and D. Yang, *Fundamentals of Liquid Crystal Devices*, ser. Wiley Series in Display Technology. Wiley, 2006. [Online]. Available: http://books.google.fr/books?id=0m2ag8AMzSkC 9, 10

[8] M. Peccianti, C. Conti, and G. Assanto, "Optical modulational instability in a nonlocal medium," *Phys. Rev. E*, vol. 68, p. 025602, Aug 2003. [Online]. Available: http://link.aps.org/doi/10.1103/PhysRevE.68.025602 9

[9] J. Margerum, J. Nimoy, and S.-Y. Yong, "Reversible ultraviolet imaging with liquid crystals," *Appl. Phys. Lett.*, vol. 17, no. 2, pp. 51–53, 1970. 10

[10] L. K. Cotter, T. J. Drabik, R. J. Dillon, and M. A. Handschy, "Ferroelectric-liquid-crystal/silicon-integrated-circuit spatial light modulator," *Opt. Lett.*, vol. 15, no. 5, pp. 291–293, 1990. 10

[11] P. Valley, D. L. Mathine, M. R. Dodge, J. Schwiegerling, G. Peyman, and N. Peyghambarian, "Tunable-focus flat liquid-crystal diffractive lens," *Opt. Lett.*, vol. 35, pp. 336–338, 2010. 10

[12] I. C. Khoo, "Nonlinear optics of liquid crystalline materials," *Phys. Rep.*, vol. 471, pp. 221–267, 2009. 10, 11

[13] A. Fratalocchi and G. Assanto, "Nonlinear all-optical switch with nematic liquid crystals," *Appl. Phys. Lett.*, vol. 86, pp. 051 109–051 111, 2005. 10

[14] A. d'Alessandro d'Alessandro d'Alessandro, R. Asquini, M. Trotta, G. Gilardi, R. Beccherelli, and I. C. Khoo, "All-optical intensity modulation of near infrared light in a liquid crystal channel waveguide," *Appl. Phys. Lett.*, vol. 97, p. 093302, 2010. 10

[15] G. Assanto and M. A. Karpierz, "Nematicons: self-localised beams in nematic liquid crystals," *Liq. Cryst.*, vol. 36, pp. 1161–1172, 2009. 10

[16] M. Peccianti and G. Assanto, "Signal readdressing by steering of spatial solitons in bulk nematic liquid crystals," *Opt. Lett.*, vol. 26, pp. 1690–1692, 2001. 10

[17] A. Pasquazi, A. Alberucci, M. Peccianti, and G. Assanto, "Signal processing by opto-optical interactions between self-localized and free propagating beams in liquid crystals," *Appl. Phys. Lett.*, vol. 87, p. 261104, 2005. 10

[18] A. Piccardi, A. Alberucci, U. Bortolozzo, S. Residori, and G. Assanto, "Read-dressable interconnects with spatial soliton waveguides in liquid crystal light valves," *IEEE Photon. Techn. Lett.*, vol. 22, pp. 694–696, 2010. 10

[19] M. Peccianti, A. Fratalocchi, and G. Assanto, "Transverse dynamics of nematicons," *Opt. Express*, vol. 12, p. 6524, 2004. 11

[20] D. Scrymgeour, A. Sharan, V. Gopalan, K. T. Gahagan, J. L. Casson, R. Sander, J. M. Robinson, F. Muhammad, P. Chandramani, and F. Kiamilev, "Cascaded

electro-optic scanning of laser light over," *App. Phys. Lett.*, vol. 81, p. 3140, 2002. 11

[21] S. R. Davis, G. Farca, S. D. Rommel, A. W. Martin, and M. H. Anderson, "Analog, non-mechanical beam-steerer with 80 degree field of regard," *Proc. SPIE*, vol. 6971, p. 69710G, 2008. 11

[22] A. Piccardi, M. Peccianti, G. Assanto, A. Dyadyusha, and M. Kaczmarek, "Voltage-driven in-plane steering of nematicons," *Appl. Phys. Lett.*, vol. 94, p. 091106, 2009. 12

[23] A. Alberucci, A. Piccardi, M. Peccianti, M. Kaczmarek, and G. Assanto, "Propagation of spatial optical solitons in a dielectric with adjustable nonlinearity," *Phys. Rev. A*, vol. 82, no. 2, p. 023806, 2010. 12, 13, 14, 16

[24] N. Tabiryan and B. Zeldovich, "The orientational optical nonlinearity of liquid-crystals," *Mol. Cryst. Liq. Cryst.*, vol. 62, pp. 237–250, 1980. 12, 14

[25] M. Peccianti, G. Assanto, A. D. Luca, C. Umeton, and I. C. Khoo, "Electrically assisted self-confinement and waveguiding in planar nematic liquid crystal cells," *Appl. Phys. Lett.*, vol. 77, no. 1, pp. 7–9, 2000. 14

[26] A. Alberucci, A. Piccardi, U. Bortolozzo, S. Residori, and G. Assanto, "All-optical control of nematicon path in liquid crystal light valves," *Opt. Lett.*, vol. 35, no. 3, pp. 390–392, 2010. 15

[27] M. Peccianti, G. Assanto, A. Dyadyusha, and M. Kaczmarek, "Non-specular total internal reflection of spatial solitons at the interface between highly birefringent media," *Phys. Rev. Lett.*, vol. 98, p. 113902, 2007. 16

[28] M. Peccianti, A. Dyadyusha, M. Kaczmarek, and G. Assanto, "Tunable refraction and reflection of self-confined light beams," *Nat. Phys.*, vol. 2, pp. 737–742, 2006. 17

[29] E. Brasselet and C. Loussert, "Electrically controlled topological defects in liquid crystals as tunable spin-orbit encoders for photons," *Opt. Lett.*, vol. 36, no. 5, pp. 719–721, Mar 2011. [Online]. Available: http://ol.osa.org/abstract.cfm?URI=ol-36-5-719 23

[30] G. P. Alexander, B. G. ge Chen, E. A. Matsumoto, and R. D. Kamien, "*Colloquium*: Disclination loops, point defects, and all that in nematic liquid

crystals," *Rev. Mod. Phys.*, vol. 84, pp. 497–514, Apr 2012. [Online]. Available: http://link.aps.org/doi/10.1103/RevModPhys.84.497 24

[31] V. P. Mineev, *Topologically Stable Defects and Solitons in Ordered Media*, ser. Classic Reviews in Physics. Harwood Academic Publishers, 1998. 24

[32] P. Chaikin and T. Lubensky, *Principles of Condensed Matter Physics*. Cambridge University Press, 2000. [Online]. Available: http://www.cambridge.org/9780521794503 24

[33] RAPINI, A., LÉGER, L., and MARTINET, A., "Umbilics : Static and dynamic properties," *J. Phys. Colloques*, vol. 36, no. C1, pp. C1–189–C1–196, 1975. [Online]. Available: http://dx.doi.org/10.1051/jphyscol:1975136 24

[34] Y. N. Ovchinnikov and I. M. Sigal, "Ginzburg-landau equation i. static vortices," in *Partial Differential Equations and their Applications*, ser. AMS CRM Proceedings and Lecture Notes Series. American Mathematical Society, 1997, pp. 199–220. 24

[35] M. Kleman and O. D. Lavrentovich, *Soft Matter Physics: An Introduction*, 1st ed. Springer, Oct. 2002. [Online]. Available: http://www.worldcat.org/isbn/0387952675 25

[36] T. Frisch, "Spiral waves in nematic and cholesteric liquid crystals," *Physica D: Nonlinear Phenomena*, vol. 84, no. 3–4, pp. 601–614, 1995. [Online]. Available: http://www.sciencedirect.com/science/article/pii/0167278994002099 28

[37] L. Pismen, *Vortices in Nonlinear Fields: From Liquid Crystals to Superfluids, from Non-equilibrium Patterns to Cosmic Strings*, ser. Oxford science publications. Oxford University Press, Incorporated, 1999. 29, 45

[38] Y. N. Ovchinnikov and I. M. Sigal, "Symmetry-breaking solutions of the ginzburg-landau equation," *Journal of Experimental and Theoretical Physics*, vol. 99, no. 5, pp. 1090–1107, 2004. [Online]. Available: http://dx.doi.org/10.1134/1.1842890 29, 33

[39] A. Rapini, "Umbilics : static properties and shear-induced displacements," *J. Phys. France*, vol. 34, no. 7, pp. 629–633, 1973. [Online]. Available: http://dx.doi.org/10.1051/jphys:01973003407062900 29

[40] S. Chandrasekhar, *Liquid Crystals*. Cambridge University Press, 1992. 30

[41] C. M. Dafermos, "Disinclinations in liquid crystals," *The Quarterly Journal of Mechanics and Applied Mathematics*, vol. 23, no. 2, pp. 49–64, 1970. [Online]. Available: http://qjmam.oxfordjournals.org/content/23/2/49.abstract 33

[42] F.-H. Lin and J. X. Xin, "On the dynamical law of the ginzburg-landau vortices on the plane," *Communications on Pure and Applied Mathematics*, vol. 52, no. 10, pp. 1189–1212, 1999. [Online]. Available: http://dx.doi.org/10.1002/(SICI)1097-0312(199910)52:10⟨1189::AID-CPA1⟩3.0.CO;2-T 33

[43] F. Bethuel, G. Orlandi, and D. Smets, "Dynamics of multiple degree ginzburg-landau vortices," *Communications in Mathematical Physics*, vol. 272, no. 1, pp. 229–261, 2007. [Online]. Available: http://dx.doi.org/10.1007/s00220-007-0206-6 33

[44] R. L. Jerrard and H. M. Soner, "Dynamics of Ginzburg-Landau Vortices," *Archive for Rational Mechanics and Analysis*, vol. 142, pp. 99–125, 1998. 33

[45] F. H. Lin, "Some dynamical properties of Ginzburg-Landau vortices," *Communications on Pure and Applied Mathematics*, vol. 49, pp. 323–359, 1996. 33

[46] I. Dierking, O. Marshall, J. Wright, and N. Bulleid, "Annihilation dynamics of umbilical defects in nematic liquid crystals under applied electric fields," *Phys. Rev. E*, vol. 71, p. 061709, Jun 2005. [Online]. Available: http://link.aps.org/doi/10.1103/PhysRevE.71.061709 33

[47] Y. Li, Y. Liu, Q. Li, and S.-T. Wu, "Polarization independent blue-phase liquid crystal cylindrical lens with a resistive film," *Appl. Opt.*, vol. 51, no. 14, pp. 2568–2572, May 2012. [Online]. Available: http://ao.osa.org/abstract.cfm?URI=ao-51-14-2568 39

[48] *Modal wavefront correction with liquid crystals: different options*, 2005. [Online]. Available: http://dx.doi.org/10.1117/12.590205 39

[49] A. K. Kirby, P. J. Hands, and G. D. Love, "Liquid crystal multi-mode lenses and axicons based on electronic phase shift control," *Opt. Express*, vol. 15, no. 21, pp. 13 496–13 501, Oct 2007. [Online]. Available: http://www.opticsexpress.org/abstract.cfm?URI=oe-15-21-13496 39

[50] K. Asatryan, V. Presnyakov, A. Tork, A. Zohrabyan, A. Bagramyan, and T. Galstian, "Optical lens with electrically variable focus using an optically

hidden dielectric structure," *Opt. Express*, vol. 18, no. 13, pp. 13 981–13 992, Jun 2010. [Online]. Available: http://www.opticsexpress.org/abstract.cfm?URI=oe-18-13-13981 39

[51] J. Margerum and J. Nimoy, "Reversible ultraviolet imaging with liquid crystals," *Applied Physics Letters*, vol. 17, no. 2, pp. 1969–1971, 1970. 39, 41

[52] P. Aubourg, J. P. Huignard, M. Hareng, and R. A. Mullen, "Liquid crystal light valve using bulk monocrystalline bi12sio20 as the photoconductive material," *Appl. Opt.*, vol. 21, no. 20, pp. 3706–3712, Oct 1982. [Online]. Available: http://ao.osa.org/abstract.cfm?URI=ao-21-20-3706 40, 41, 66, 70

[53] P. Gèunter and J. Huignard, *Photorefractive Materials and Their Applications 2: Materials*, ser. Springer series in optical sciences. Springer London, Limited, 2007. 40

[54] G. V. Vdovin, I. R. Guralnik, S. P. Kotova, M. Y. Loktev, and A. F. Naumov, "Liquid-crystal lenses with a controlled focal length. i. theory," *Quantum Electronics*, vol. 29, no. 3, p. 256, 1999. [Online]. Available: http://stacks.iop.org/1063-7818/29/i=3/a=A16 40

[55] ——, "Liquid-crystal lenses with a controlled focal length. ii. numerical optimisation and experiments," *Quantum Electronics*, vol. 29, no. 3, p. 261, 1999. [Online]. Available: http://stacks.iop.org/1063-7818/29/i=3/a=A17 40

[56] M. Herrington, K. Daly, O. Buchnev, G. D'Alessandro, and M. Kaczmarek, "Ac-field–enhanced beam coupling in photorefractive, hybrid liquid crystals," *EPL (Europhysics Letters)*, vol. 95, no. 1, p. 14003, 2011. [Online]. Available: http://stacks.iop.org/0295-5075/95/i=1/a=14003 40

[57] F. Kajzar and V. Agranovich, *Multiphoton and Light Driven Multielectron Processes in Organics: New Phenomena, Materials, and Applications*, ser. NATO Science Series. Kluwer Academic Publishers, 2000. 40

[58] N. Sanner, N. Huot, E. Audouard, C. Larat, J.-P. Huignard, and B. Loiseaux, "Programmable focal spot shaping of amplified femtosecond laser pulses," *Opt. Lett.*, vol. 30, no. 12, pp. 1479–1481, Jun 2005. [Online]. Available: http://ol.osa.org/abstract.cfm?URI=ol-30-12-1479 41

[59] J. Heebner, M. Borden, P. Miller, S. Hunter, K. Christensen *et al.*, "Programmable beam spatial shaping system for the national ignition facility," in

Proc. SPIE 7916, High Power Lasers for Fusion Research, vol. 79160H, 2011, pp. 79 160H–79 160H–6. [Online]. Available: http://dx.doi.org/10.1117/12.875794 41

[60] S. Residori, "Patterns, fronts and structures in a liquid-crystal-light-valve with optical feedback," *Physics Reports*, vol. 416, no. 5â"6, pp. 201–272, 2005. [Online]. Available: http://www.sciencedirect.com/science/article/pii/S0370157305002668 41

[61] S. Residori, U. Bortolozzo, and J. Huignard, "Slow light using wave mixing in liquid crystal light valve," *Applied Physics B*, vol. 95, no. 3, pp. 551–557, 2009. [Online]. Available: http://dx.doi.org/10.1007/s00340-009-3556-2 41

[62] F. Lenzini, S. Residori, F. T. Arecchi, and U. Bortolozzo, "Optical vortex interaction and generation via nonlinear wave mixing," *Phys. Rev. A*, vol. 84, p. 061801, Dec 2011. [Online]. Available: http://link.aps.org/doi/10.1103/PhysRevA.84.061801 41

[63] A. Piccardi, A. Alberucci, U. Bortolozzo, S. Residori, and G. Assanto, "Soliton gating and switching in liquid crystal light valve," *Applied Physics Letters*, vol. 96, no. 7, p. 071104, 2010. [Online]. Available: http://link.aip.org/link/?APL/96/071104/1 41

[64] U. Bortolozzo, S. Residori, and J.-P. Huignard, "Adaptive holography in liquid crystal light-valves," *Materials*, vol. 5, no. 9, pp. 1546–1559, 2012. [Online]. Available: http://www.mdpi.com/1996-1944/5/9/1546 41

[65] E. Brasselet, N. Murazawa, H. Misawa, and S. Juodkazis, "Optical vortices from liquid crystal droplets," *Phys. Rev. Lett.*, vol. 103, p. 103903, Sep 2009. [Online]. Available: http://link.aps.org/doi/10.1103/PhysRevLett.103.103903 42

[66] M. S. Soskin, V. G. Denisenko, and R. I. Egorov, "Singular Stokes-polarimetry as new technique for metrology and inspection of polarized speckle fields," in *Society of Photo-Optical Instrumentation Engineers (SPIE) Conference Series*, ser. Society of Photo-Optical Instrumentation Engineers (SPIE) Conference Series, C. Gorecki and A. K. Asundi, Eds., vol. 5458. SPIE, Aug. 2004, pp. 79–85. [Online]. Available: http://dx.doi.org/10.1117/12.544681 42

[67] R. A. Beth, "Mechanical detection and measurement of the angular momentum of light," *Phys. Rev.*, vol. 50, pp. 115–125, Jul 1936. [Online]. Available: http://link.aps.org/doi/10.1103/PhysRev.50.115 49

[68] H. He, M. E. J. Friese, N. R. Heckenberg, and H. Rubinsztein-Dunlop, "Direct observation of transfer of angular momentum to absorptive particles from a laser beam with a phase singularity," *Phys. Rev. Lett.*, vol. 75, pp. 826–829, Jul 1995. [Online]. Available: http://link.aps.org/doi/10.1103/PhysRevLett.75.826 49

[69] A. T. O'Neil, I. MacVicar, L. Allen, and M. J. Padgett, "Intrinsic and extrinsic nature of the orbital angular momentum of a light beam," *Phys. Rev. Lett.*, vol. 88, p. 053601, Jan 2002. [Online]. Available: http://link.aps.org/doi/10.1103/PhysRevLett.88.053601 49

[70] N. Simpson, L. Allen, and M. Padgett, "Optical tweezers and optical spanners with laguerre-gaussian modes," *Journal of Modern Optics*, vol. 43, no. 12, pp. 2485–2491, 1996. 50

[71] J. E. Curtis, B. A. Koss, and D. G. Grier, "Dynamic holographic optical tweezers," *Optics Communications*, vol. 207, no. 1–6, pp. 169–175, 2002. [Online]. Available: http://www.sciencedirect.com/science/article/pii/S0030401802015249 50

[72] D. G. Grier, "A revolution in optical manipulation," *Nature*, vol. 424, pp. 810–816, Aug. 2003. 50

[73] M. Padgett and R. Bowman, "Tweezers with a twist," *Nature Photonics*, vol. 5, pp. 343–348, Jun. 2011. 50

[74] J. Hamazaki, R. Morita, K. Chujo, Y. Kobayashi, S. Tanda, and T. Omatsu, "Optical-vortex laser ablation," *Opt. Express*, vol. 18, no. 3, pp. 2144–2151, Feb 2010. [Online]. Available: http://www.opticsexpress.org/abstract.cfm?URI=oe-18-3-2144 50

[75] O. J. Allegre, W. Perrie, S. P. Edwardson, G. Dearden, and K. G. Watkins, "Laser microprocessing of steel with radially and azimuthally polarized femtosecond vortex pulses," *Journal of Optics*, vol. 14, no. 8, p. 085601, Aug. 2012. 50

[76] C. Hnatovsky, V. G. Shvedov, W. Krolikowski, and A. V. Rode, "Materials processing with a tightly focused femtosecond laser vortex pulse," *Opt. Lett.*, vol. 35, no. 20, pp. 3417–3419, Oct 2010. [Online]. Available: http://ol.osa.org/abstract.cfm?URI=ol-35-20-3417 50

[77] G. Foo, D. M. Palacios, and J. G. A. Swartzlander, "Optical vortex coronagraph," *Optics Letters*, vol. 30, pp. 3308–3310, Dec. 2005. 50

[78] E. Serabyn, D. Mawet, and R. Burruss, "An image of an exoplanet separated by two diffraction beamwidths from a star," *Nature*, vol. 464, pp. 1018–1020, 2010. 50

[79] F. Tamburini, G. Anzolin, G. Umbriaco, A. Bianchini, and C. Barbieri, "Overcoming the Rayleigh Criterion Limit with Optical Vortices," *Physical Review Letters*, vol. 97, no. 16, p. 163903, Oct. 2006. 50

[80] H. H. Arnaut and G. A. Barbosa, "Orbital and intrinsic angular momentum of single photons and entangled pairs of photons generated by parametric down-conversion," *Phys. Rev. Lett.*, vol. 85, pp. 286–289, Jul 2000. [Online]. Available: http://link.aps.org/doi/10.1103/PhysRevLett.85.286 50

[81] E. Nagali, F. Sciarrino, F. De Martini, L. Marrucci, B. Piccirillo, E. Karimi, and E. Santamato, "Quantum information transfer from spin to orbital angular momentum of photons," *Phys. Rev. Lett.*, vol. 103, p. 013601, Jun 2009. [Online]. Available: http://link.aps.org/doi/10.1103/PhysRevLett.103.013601 50

[82] L.-P. Deng, H. Wang, and K. Wang, "Quantum cnot gates with orbital angular momentum and polarization of single-photon quantum logic," *J. Opt. Soc. Am. B*, vol. 24, no. 9, pp. 2517–2520, Sep 2007. [Online]. Available: http://josab.osa.org/abstract.cfm?URI=josab-24-9-2517 50

[83] L. Marrucci, E. Karimi, S. Slussarenko, B. Piccirillo, E. Santamato, E. Nagali, and F. Sciarrino, "Spin-to-orbital conversion of the angular momentum of light and its classical and quantum applications," *Journal of Optics*, vol. 13, no. 6, p. 064001, 2011. [Online]. Available: http://stacks.iop.org/2040-8986/13/i=6/a=064001 50

[84] L. Mandel and E. Wolf, *Optical Coherence and Quantum Optics*, L. Mandel and E. Wolf, Eds. Cambridge University Press, Sep. 1995. 50, 51

[85] J. Jackson, *Classical Electrodynamics*. Wiley, 1999. 50

[86] L. Allen, M. W. Beijersbergen, R. J. C. Spreeuw, and J. P. Woerdman, "Orbital angular momentum of light and the transformation of laguerre-gaussian laser modes," *Phys. Rev. A*, vol. 45, pp. 8185–8189, Jun 1992. [Online]. Available: http://link.aps.org/doi/10.1103/PhysRevA.45.8185 53

[87] M. Beijersbergen, L. Allen, H. van der Veen, and J. Woerdman, "Astigmatic laser mode converters and transfer of orbital angular momentum," *Optics*

Communications, vol. 96, no. 1–3, pp. 123–132, 1993. [Online]. Available: http://www.sciencedirect.com/science/article/pii/003040189390535D 53

[88] J. Courtial and M. Padgett, "Performance of a cylindrical lens mode converter for producing laguerre–gaussian laser modes," *Optics Communications*, vol. 159, no. 1–3, pp. 13–18, 1999. [Online]. Available: http://www.sciencedirect.com/science/article/pii/S0030401898005999 53

[89] M. W. Beijersbergen, R. P. C. Coerwinkel, M. Kristensen, and J. P. Woerdman, "Helical-wavefront laser beams produced with a spiral phaseplate," *Optics Communications*, vol. 112, pp. 321–327, Dec. 1994. 53

[90] G. Turnbull, D. Robertson, G. Smith, L. Allen, and M. Padgett, "The generation of free-space laguerre-gaussian modes at millimetre-wave frequencies by use of a spiral phaseplate," *Optics Communications*, vol. 127, no. 4–6, pp. 183–188, 1996. [Online]. Available: http://www.sciencedirect.com/science/article/pii/0030401896000703 54

[91] Z. Bomzon, G. Biener, V. Kleiner, and E. Hasman, "Space-variant Pancharatnam-Berry phase optical elements with computer-generated subwavelength gratings," *Optics Letters*, vol. 27, pp. 1141–1143, Jul. 2002. 56

[92] L. Marrucci, C. Manzo, and D. Paparo, "Pancharatnam-Berry phase optical elements for wave front shaping in the visible domain: Switchable helical mode generation," *Applied Physics Letters*, vol. 88, no. 22, p. 221102, May 2006. 56

[93] E. Karimi, B. Piccirillo, L. Marrucci, and E. Santamato, "Light propagation in a birefringent plate with topological charge," *Opt. Lett.*, vol. 34, no. 8, pp. 1225–1227, Apr 2009. [Online]. Available: http://ol.osa.org/abstract.cfm?URI=ol-34-8-1225 58, 73

[94] E. Karimi, B. Piccirillo, E. Nagali, L. Marrucci, and E. Santamato, "Efficient generation and sorting of orbital angular momentum eigenmodes of light by thermally tuned q-plates," *Applied Physics Letters*, vol. 94, no. 23, p. 231124, 2009. [Online]. Available: http://link.aip.org/link/?APL/94/231124/1 58

[95] B. Piccirillo, V. D'Ambrosio, S. Slussarenko, L. Marrucci, and E. Santamato, "Photon spin-to-orbital angular momentum conversion via an electrically tunable [bold q]-plate," *Applied Physics Letters*, vol. 97, no. 24, p. 241104, 2010. [Online]. Available: http://link.aip.org/link/?APL/97/241104/1 58

[96] L. Marrucci, "Generation of helical modes of light by spin-to-orbital angular momentum conversion in inhomogeneous liquid crystals," *Molecular Crystals and Liquid Crystals*, vol. 488, no. 1, pp. 148–162, 2008. 59

[97] E. Brasselet and C. Loussert, "Electrically controlled topological defects in liquid crystals as tunable spin-orbit encoders for photons," *Opt. Lett.*, vol. 36, no. 5, pp. 719–721, Mar 2011. [Online]. Available: http://ol.osa.org/abstract.cfm?URI=ol-36-5-719 60

[98] S. Slussarenko, A. Murauski, T. Du, V. Chigrinov, L. Marrucci, and E. Santamato, "Tunable liquid crystal q-plates with arbitrary topological charge," *Opt. Express*, vol. 19, no. 5, pp. 4085–4090, Feb 2011. [Online]. Available: http://www.opticsexpress.org/abstract.cfm?URI=oe-19-5-4085 60

[99] A. Bekshaev and S. Sviridova, "Effects of misalignments in the optical vortex transformation performed by holograms with embedded phase singularity," *Optics Communications*, vol. 283, no. 24, pp. 4866–4876, 2010. [Online]. Available: http://www.sciencedirect.com/science/article/pii/S0030401810007686 60

[100] M. E. Ketara and E. Brasselet, "Self-induced nonlinear spin–orbit interaction of light in liquid crystals," *Opt. Lett.*, vol. 37, no. 4, pp. 602–604, Feb 2012. [Online]. Available: http://ol.osa.org/abstract.cfm?URI=ol-37-4-602 63

[101] E. Brasselet, "Singular optical reordering of liquid crystals using gaussian beams," *Journal of Optics*, vol. 12, no. 12, p. 124005, 2010. [Online]. Available: http://stacks.iop.org/2040-8986/12/i=12/a=124005 63

[102] Z. Bomzon, G. Biener, V. Kleiner, and E. Hasman, "Vectorial vortex structures formed by computer-generated space-variant dielectric subwavelength gratings," in *Lasers and Electro-Optics, 2002. CLEO '02. Technical Digest. Summaries of Papers Presented at the*, 2002, pp. 74–75 vol.1. 70

[103] E. Hasman, A. Niv, G. Biener, and V. Kleiner, "Vectorial vortices obtained with quantized Pancharatnam-Berry phase optical elements," in *Society of Photo-Optical Instrumentation Engineers (SPIE) Conference Series*, ser. Society of Photo-Optical Instrumentation Engineers (SPIE) Conference Series, D. L. Andrews, Ed., vol. 6131, Feb. 2006, pp. 27–34. 70

[104] A. Bekshaev and A. Karamoch, "Spatial characteristics of vortex light beams produced by diffraction gratings with embedded phase singularity," *Optics*

Communications, vol. 281, no. 6, pp. 1366 – 1374, 2008. [Online]. Available: http://www.sciencedirect.com/science/article/pii/S0030401807011996 73